MONTAN
UNIVERSITÄT
LEOBEN

Chair of Materials Science and Testing of Polymers

Master's Thesis

Morphology and fracture mechanical behavior of Polyoxymethylene platelets produced by injection molding under industrial-near processing conditions

Eric Kurt Helfer, BSc

March 2020

MONTANUNIVERSITÄT LEOBEN
www.unileoben.ac.at

EIDESSTATTLICHE ERKLÄRUNG

Ich erkläre an Eides statt, dass ich diese Arbeit selbständig verfasst, andere als die angegebenen Quellen und Hilfsmittel nicht benutzt, und mich auch sonst keiner unerlaubten Hilfsmittel bedient habe.

Ich erkläre, dass ich die Richtlinien des Senats der Montanuniversität Leoben zu "Gute wissenschaftliche Praxis" gelesen, verstanden und befolgt habe.

Weiters erkläre ich, dass die elektronische und gedruckte Version der eingereichten wissenschaftlichen Abschlussarbeit formal und inhaltlich identisch sind.

Datum 08.03.2020

Unterschrift Verfasser/in
Eric Kurt, Helfer

EIDESSTATTLICHE ERKLÄRUNG

Ich erkläre an Eides statt, dass ich diese Arbeit selbstständig verfasst, andere als die angegebenen Quellen und Hilfsmittel nicht benutzt und mich auch sonst keiner unerlaubter Hilfsmittel bedient habe.

AFFIDAVIT

I declare in lieu of oath, that I wrote this thesis and performed the associated research myself, using only literature cited in this volume.

LEOBEN, March 2020 **(Eric Helfer)**

ACKNOWLEDGEMENT

The research work of this paper was performed at the Polymer Competence Center Leoben GmbH (PCCL, Austria) within the framework of the “BRIDGE” program of the Federal Ministry for Transport, Innovation and Technology and the Federal Ministry of Digital and Economic Affairs with contributions by the Institute of Materials Science and Testing of Polymers / Montanuniversitaet Leoben and the Department of Industrial Engineering / University of Salerno. The PCCL is funded by the Austrian Government and the State Governments of Styria, Lower Austria and Upper Austria.

I express my great appreciation to my supervisor Dipl.-Ing. Dr.mont. Michael Berer. His support and guidance exceeded by far what one can expect. Especially his patience throughout this study and the time he took for discussions are highly appreciated.

For the appraisal of this thesis, my thanks go to Univ.-Prof. Dipl.-Ing. Dr.mont. Gerald Pinter.

Also, I thank Dipl.-Ing. Dr.mont. Michael Feuchter for introducing me to the field of X-ray measurements in polymer science and for sharing his knowledge with me.

My explicit appreciation also extends to Dipl.-Ing. Theresia Schrank and Bernd Haar. They always had an open ear for my issues and many helpful discussions ensued. Please be assured that your support was never taken for granted.

Finally, special thanks go to my family for their support throughout the whole studying time. Thank you for always being there when I needed moral support and for bringing motivation and joy into my life.

ABSTRACT

Polyoxymethylene (POM) is an engineering thermoplastic with a high degree of crystallinity and excellent mechanical properties. It is used in a wide field of industry sectors that require good mechanical properties. For polymers, the mechanical properties are amongst others determined by the morphology of the material. These can be influenced by various aspects like additives and especially by the processing.

In this thesis, injection molded platelets were analyzed to find a correlation between process settings, morphology and fracture mechanical properties. The production of the platelets was carried out following a design of experiments (DOE), where mold temperature, injection speed and packing pressure were varied. To analyze the morphological state in the specimens, small-angle X-ray scattering (SAXS) and wide-angle X-ray diffraction (WAXD) as well as polarized light microscopy (PLM) were used. The fracture mechanical analysis included monotonic fracture tests as well as cyclic fatigue fracture tests. For these tests, so called micro single-edge notched tension (µ-SENT) specimens, which were obtained from the injection molded platelets, were used. Additionally to all tests, filling simulations in MoldFlow were carried out. MoldFlow allows to model the crystallization in polymers during injection molding. To asses these results, they were compared to the results obtained by the X-ray measurements and by PLM.

Specimens produced with a higher mold temperature showed an increase in the crystalline fraction and the lamellar thickness while a decrease in the fracture toughness occurred. The fatigue behavior did not seem to be influenced much by the mold temperature. Higher injection speeds led to higher oriented samples. These samples showed an improvement in both the monotonic and fatigue fracture properties in the range examined. The packing pressure did not show any significant influence on both the morphology and the fracture mechanical properties. It is assumed that the effect of the holding pressure in the very small platelets is rather low, especially in the area away from the sprue. This leads to the conclusion that the orientation of the lamellae and crystals improved the fracture mechanical behavior for the resin used in this thesis. With the PLM, it was difficult to accurately determine the transition between the different layers in the injection molded samples. Hence, further investigation with etching in combination with Scanning Electron Microscopy is recommended. The simulations provided information about the different crystal sizes of the various process conditions. However, the individual spherulites were too small to be quantified by PLM and therefore could not be compared to the results from the simulations. Furthermore, the simulations gave information about the orientation of the crystals. The values obtained could not be directly compared to the values obtained by the X-ray measurements, because the reference axis was different and the X-ray measurements only took into account a single crystal plane.

KURZFASSUNG

Polyoxymethylen (POM) ist ein technischer Thermoplast mit hohen Kristallinitätsgraden und hervorragenden mechanischen Eigenschaften. Er wird in einem weiten Feld von Industriebereichen verwendet, in denen gute mechanische Eigenschaften erforderlich sind. Bei polymeren Werkstoffen werden die mechanischen Eigenschaften unter anderem durch die Morphologie des Materials bestimmt. Diese kann durch verschiedene Faktoren, wie zum Beispiel Additive und insbesondere durch die Verarbeitung beeinflusst werden.

Um eine Korrelation zwischen Prozesseinstellungen, Morphologie und bruchmechanischen Eigenschaften von POM zu finden, wurden in dieser Arbeit spritzgegossene Plättchen analysiert. Die Herstellung der Plättchen erfolgte anhand eines Versuchsplanes, bei dem die Werkzeugtemperatur, die Einspritzgeschwindigkeit und der Nachdruck variiert wurden. Zur Analyse des morphologischen Zustands in den Proben wurden die Kleinwinkel-Röntgenstreuung (SAXS) und die Weitwinkel-Röntgenbeugung (WAXD) sowie die Polarisationslichtmikroskopie (PLM) verwendet. Die bruchmechanische Analyse umfasste sowohl monotone Bruchzähigkeitsversuche als auch zyklische Ermüdungsversuche. Für diese Tests wurden so genannte Mikro Single-Edge Notched Tension (µ-SENT) Prüfkörper verwendet, die direkt aus den spritzgegossenen Plättchen hergestellt wurden. Zusätzlich zu allen Versuchen wurden auch Füllsimulationen in MoldFlow durchgeführt. MoldFlow ermöglicht die Modellierung der Kristallisation in Polymeren während des Spritzgießens. Um diese Ergebnisse zu bewerten, wurden sie mit den Ergebnissen aus den Röntgenmessungen und der PLM verglichen.

Proben, die mit einer höheren Werkzeugtemperatur hergestellt wurden, zeigten eine Zunahme der Kristallinität und der Lamellendicke, wobei eine Abnahme der Bruchzähigkeit auftrat. Das Ermüdungsverhalten schien von der Werkzeugtemperatur nicht wesentlich beeinflusst zu werden. Höhere Einspritzgeschwindigkeiten führten zu einem höheren Orientierungsgrad in den Proben. Diese Proben zeigten eine Verbesserung der monotonen bruchmechanischen Eigenschaften als auch der Ermüdungseigenschaften im untersuchten Bereich. Der Nachdruck zeigte keinen signifikanten Einfluss auf die Morphologie und die bruchmechanischen Eigenschaften. Es ist anzunehmen, dass die Nachdruckwirksamkeit in den sehr dünnen Plättchen vor allem im angussfernen Bereich sehr gering war. Dies führt

zu der Schlussfolgerung, dass die Orientierung der Lamellen und Kristalle für ein verbessertes bruchmechanisches Verhalten des in dieser Arbeit verwendeten Materials beitragen. Mit PLM gestaltete es sich schwierig, den Übergang zwischen den verschiedenen Schichten in den spritzgegossenen Proben genau zu bestimmen. Daher wird eine weitere Untersuchung mittels Ätzen in Kombination mit Rasterelektronenmikroskopie empfohlen. Die Simulationen lieferten Auskunft über die unterschiedlichen Kristallgrößen der verschiedenen Prozessbedingungen. Jedoch waren die einzelnen Sphärolithe zu klein, um sie durch PLM quantifizieren zu können und daher konnten sie nicht mit den Ergebnissen aus der Simulation verglichen werden. Weiters gaben die Simulationen Auskunft über die Orientierungen der Kristalle. Die erhaltenen Werte konnten nicht direkt mit den Werten aus den Röntgenmessungen verglichen werden, da die Bezugsachse unterschiedlich war sowie die Röntgenmessungen nur eine einzelne Kristallebene betrachteten.

TABLE OF CONTENT

SYMBOLS AND ABBREVIATIONS

POM	Polyoxymethylene
DOE	Design of experiments
SAXS	Small angle X-ray scattering
WAXD	Wide angle X-ray diffraction
q, 2θ	Radial angle in SAXS and WAXD, respectively
ϕ	Azimuthal angle in SAXS and WAXD
PLM	Polarized light microscopy
LEFM	Linear elastic fracture mechanics
SENT	Single-edge notched tension specimen
K	Stress intensity factor
K_C	Fracture toughness
LP	Long period
o-POM	Orthogonal POM
t-POM	Trigonal POM
FCC	Folded chain crystal
ECC	Extended chain crystal
TM	Tie molecules
M	Molecular weight
MWD	Molecular weight distribution

LIST OF FIGURES

1 INTRODUCTION

Polyoxymethylene (POM) is an engineering thermoplastic, which is important both industrially and scientifically. Due to its high degree of crystallinity, excellent mechanical properties and high chemical resistance it is used in applications in many different industry sectors (e.g. bearing elements or gear wheels) (Berer and Major, 2010, 2012; Lüftl et al., 2014). In general, the mechanical properties of polymers are strongly dependent on their inner structure and are influenced by the production process and additives such as impact modifiers and nucleating agents. To understand the influence of different processing parameters on the mechanical properties and performance of the final part, it is necessary to completely understand the influence on the morphology first. Hence, the influence of the morphology on the mechanical behavior of POM was studied excessively (Berer et al., 2014; Berer et al., 2018; Halb, 2016).

The aim of the present thesis is to improve the knowledge of the influence of the injection molding process settings on the morphology and fracture mechanical behavior of a POM homopolymer. Furthermore, the correlation between the morphology and the mechanical properties was investigated. For a better understanding the structure of this thesis is illustrated in Fig. 1.1. Small platelets were produced by injection molding following a design of experiments (DOE). The DOE included a variation in mold temperature, injection speed and holding pressure. Small-angle X-ray scattering (SAXS), wide-angle X-ray diffraction (WAXD) and polarized light microscopy (PLM) were applied to analyze the morphology of the samples. To investigate the mechanical behavior, linear elastic fracture mechanics (LEFM) was applied. The analysis included monotonic fracture tests as well as cyclic fatigue fracture tests, which were used to obtain fracture mechanical fatigue curves. So called micro single-edge notched tension (µ-SENT) specimens, which were obtained from the injection molded platelets, were used for these tests. From the results of these characterization methods it was possible to deduce a correlation between process settings, the morphology and fracture mechanical properties.

Since simulations take an important part in the processing industry nowadays, injection molding simulations in MoldFlow were carried out as well. The focus here lied on the crystallization behavior of POM during the injection molding process. All parameters for the crystallization model for POM, which were used in these simulations, were determined by the Department of Industrial Engineering at the University of Salerno (Italy). The results from these studies were assessed by comparing them to the morphological information obtained by the X-ray experiments and PLM studies.

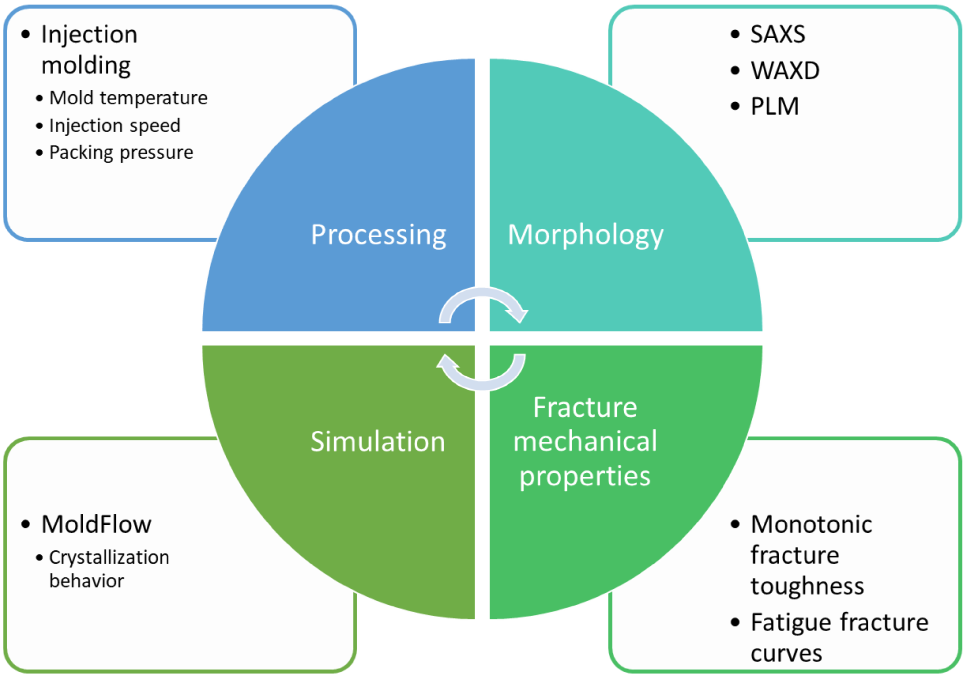

Fig. 1.1: Illustration of the aim of this thesis

2 THEORETIC BACKGROUND

2.1 Morphology of POM

Semi-crystalline polymers share a hierarchical morphology as one common feature and their structural details range from nanometers to millimeters. These polymers have a regular chain structure with a preferred chain conformation. Specific factors like chain branches at high concentrations, chain-end defects, atactic sequences or variations in molecular weight hinder the ability to form perfect crystals and lead to a separation into two phases: the highly ordered domain (crystalline phase) and the region containing randomly coiled chains (amorphous phase) (Gedde, 2013; Michler, 2008). This separation often leads to a lamellar structure, which will be described later. Different aspects like molecular weight, chain architecture (constitution, configuration), cooling rate and temperature during processing and the thermal and mechanical history of the material have an influence on the crystal formation and hierarchical structures (Michler, 2016). In semi-crystalline polymers the crystalline domains consist of folded polymer chains. Those chains form a lamellar layer with a distinct thickness. In between those lamellas are the remaining amorphous regions. The long period (LP), which is the average thickness of one lamella and one amorphous region, and the different layer thicknesses (lamellae or amorphous layer) can be used to describe the structure in semi-crystalline polymers (Gedde, 2013).

POM is a linear, semi-crystalline polymer consisting of the monomer unit $[\text{-CH}_2\text{-O-}]_n$. It can exist in two polymeric forms: the orthorhombic (o-POM) and the trigonal (t-POM) one. They distinguish themselves both in lattice structure as well as in conformation. The orthorhombic POM is a metastable phase with molecular chains of 2/1 helical conformation where two monomers are necessary for one turn of the helix. By heating the material, the metastable orthorhombic phase can easily be transformed into the stable trigonal phase. The stable trigonal form has a 9/5 (9 monomers in 5 turns) helical structure with a hexagonal unit cell structure (Kurosu et al., 1988; Zamboni and Zerbi, 1964). Due to their different physical properties, the two polymorphic forms can be detected through various methods e.g. wide-angle X-ray diffraction (WAXD). The different lattice constants of the crystalline systems lead to different peaks in the diffraction diagrams (Lüftl et al., 2014; Shimomura, 1993).

POM has three known crystal structures: the folded-chain crystals (FCC), the extended-chain crystals (ECC) and the shish-kebab structure. Compared to the ECCs, the FCCs can be regarded as imperfect crystals with folded-chain segments on two opposite sides and shorter stems. Therefore, FCCs start to melt at a lower temperature than ECCs. FCCs can be obtained as hexagonal-shaped lamellae by crystallization from a diluted solution. ECCs result from a cationic polymerization of trioxane, yielding in needle-like crystals where extended molecule chains align parallel to the needle axis (Kongkhlang et al., 2011; Lüftl et al., 2014). Shish kebab structures are a hybrid of FCCs and ECCs, where lamellae grow around a needle-shaped single crystal (Iguchi and Murase, 1975). The FCC and ECC have quite similar WAXD patterns, but they can easily be distinguished by Fourier transform infrared (FTIR) spectroscopy due to its higher sensitivity to morphological changes (Lüftl et al., 2014; Shimomura et al., 1988). (Hama and Tashiro, 2003a, 2003b) studied the formation of the crystalline phases in POM during cooling from the melt with non-isothermal SAXS and WAXD measurements as well as FTIR. They discovered that FCC-lamellae with ECC-stems instead of secondary lamellae form during crystallization from the melt. This phenomenon is not common in other polymers. These ECC-stems can be interpreted as a bundle of stretched tie molecules which pass through the continuously stacked lamellae. Fig. 2.1 illustrates the growth of FCC and ECC during melt-crystallization:

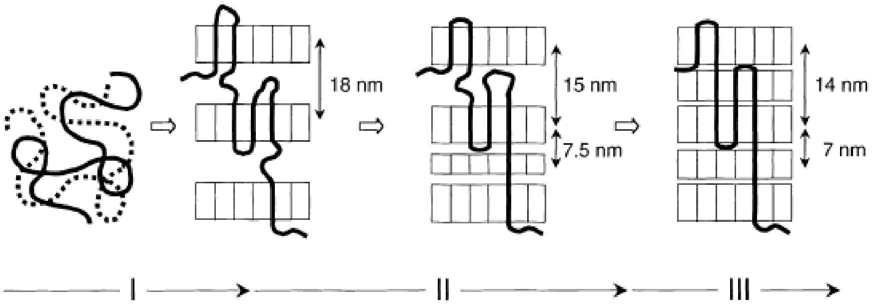

Fig. 2.1: Formation of FCC and ECC in POM during melt-crystallization (Hama and Tashiro, 2003a)

Foreign particles, the history of the material as well as the crystallization conditions strongly influence the final structure of crystals in polymers. For instance, melt crystallization leads to spherulites while crystallization from dilute solutions leads to single crystals of various shapes (Raimo, 2011). Spherulite structures are of greater importance for this work than single crystals and are therefore described hereafter. They are spherically symmetric crystal colonies with a diameter up to 5 mm and are composed of radially directed fibrils. These fibrils consist of ribbonlike crystals elongated in the growth direction. Amorphous chains fill the space between the crystalline areas. In the optical light microscope, spherulites display a typical Maltese cross (Crist and Schultz, 2016; Geil, 1967).

Both entanglements and tie molecules are two important morphological phenomena present in semi-crystalline polymers and thus in POM. Without those molecular connections, the crystalline areas would only be held together by weak van der Waals and hydrogen interactions, leading to an easy split away from each other under load. Entanglements are physically crosslinked chains. They can also be described as a kind of knots. Through solidification these crosslinked chains get preserved. Tie molecules are molecule chains which go through two adjacent lamellae and tie the lamellae together, serving as a connection or covalent bond. According to (Seguela, 2005), chains from adjacent lamellae are usually intertwined and cannot be separated easily due to their arrangement. This leads to an additional strength of the polymer. In Fig. 2.2 entanglements, tie molecules as well as loose loops are illustrated: l_c represents the thickness of a crystalline lamella, l_a the thickness of an amorphous layer.

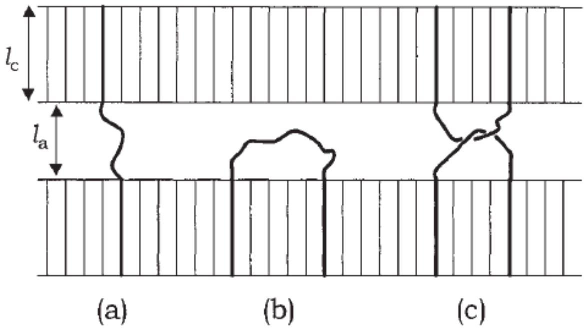

Fig. 2.2: Illustration of a tie molecule (a), a loose loop (b) and an entanglement (c) (Seguela, 2005)

2.2 Linear elastic fracture mechanics (LEFM)

Mechanical testing investigates the behavior of materials under load and is used in material development and the designing of components. Furthermore, these tests are fundamental when it comes to predicting the long-term behavior of structural components. Monotonous, static as well as cyclic fatigue loads are applied in mechanical tests. Cyclic fatigue loads are the most critical and lead to the fastest failure in mechanical tests. They can either be carried out using a fracture mechanical or a stress-based approach (using Woehler curves). Linear elastic fracture mechanics (LEFM) is a concept based on linear elasticity and is used as a tool for material ranking and life-time modelling. Polymeric materials do usually not show a linear elastic behavior, but LEFM is nevertheless suitable for describing crack growth in polymers (Hashemi and Williams, 1984). Different authors (Arbeiter et al., 2015; Berer et al., 2014; Berer et al., 2015; Berer et al., 2018; Halb, 2016) were able to successfully use LEFM on unfilled engineering thermoplastics like polyetheretherketone (PEEK) and POM and therefore, LEFM is used in this present study.

A crack can be subjected to different load types (modes), as shown in Fig. 2.3. The Mode I load leads to a pure tensile load, which opens the crack. The Mode II describes the shear loading in the crack plane and Mode III describes the shear loading out of the crack plane. Under these three modes, Mode I is considered to be the most critical one. In reality, very often an overlay of all three modes occurs (Anderson, 2005).

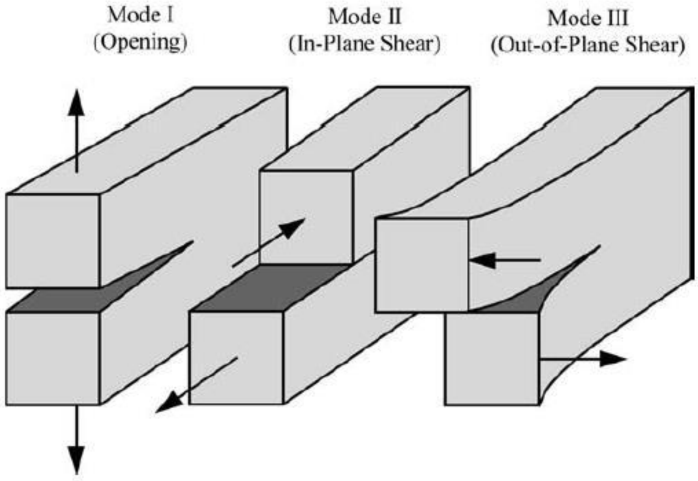

Fig. 2.3: The three different crack tip opening modes in fracture mechanics (Anderson, 2005)

In order to describe the stress state near a crack tip, the stress intensity factor K is used. According to Eq. (2.1), the stress intensity factor K_I is calculated from the global stress σ, the crack length a and a dimensionless form factor Y, which depends on the component and test piece geometry. The index I indicates the mode I loading. Y can be looked up in the literature for many specimen geometries. For complicated geometries, it is determined via FEM simulations The minimum value of K_I in a monotonous fracture test is called the fracture toughness of the material or K_{IC}. Failure occurs when $K_I \geq K_{IC}$, leading to a propagation of the crack (Anderson, 2005; Kinloch and Young, 1995).

$$K_I = \sigma \cdot \sqrt{a} \cdot Y \qquad (2.1)$$

LEFM was originally developed for materials, which show a linear-elastic behavior. Polymers never show an ideal linear-elastic behavior. They behave non-linear in a stress-strain diagram and show viscoelastic (time-dependent) mechanical properties. This later lead to the revision of LEFM to include materials with small scale plasticity and linear viscoelastic behavior (Anderson, 2005). Besides linear and non-linear viscoelastic behavior, polymers show history dependence of properties and hysteretic heating (Domininghaus et al., 2012). In the 1980s Hashemi and Williams as well as Lang developed a concept to apply LEFM for fatigue tests of polymers (Hashemi and Williams, 1984; Lang, 1984). Several aspects, which can have an influence on the results of LEFM tests carried out on polymers, have to be kept in mind. In the case of the measurements, the plastic zone in front of the crack tip can cause material changes, which can hinder the stable fatigue crack growth (Berer et al., 2014). The thermal and mechanical history of the polymer play an important part as well. During fatigue testing, every material element in the crack plane of the uncracked ligament is cyclically loaded. Under the assumption of stable crack growth, the crack moves continuously as it grows into a region of the specimen that has been subjected to a different loading history. This so-called far-field history not only introduces changes in the viscoelastic state of the material distant from the crack tip, but additionally influences the yield behavior of each element, as it gets approached by the crack. Accordingly, even tests with constant values of ΔK can show changes in crack growth rates (Lang et al., 2004).

Since Mode I is considered as the most critical loading case in service applications, it is used in this study. For monotonic crack tests, K_I can be calculated according to ASTM E 399. For fatigue crack growth tests, the difference of the maximum and minimum load (F_{max} and F_{min}) of the load signal is used to calculate ΔK_I. For a single-edge notched tension (SENT-) specimen (Fig. 2.4), which is used in this work, K_I can be calculated according to Eq. (2.2). In order to calculate ΔK_I, Eq. (2.2) can be used as well, F_Q just has to be substituted with F_{max}-F_{min} (ASTM E 0647-15; ASTM E 399 - 19; Grellmann and Seidler, 2011). In Eq. (2.2) B is the thickness of the specimen, W is the specimen width and a is the initial crack length as illustrated in Fig. 2.4.

$$K_I = \frac{F_Q}{B \cdot W} \cdot \sqrt{a} \cdot \left(1.99 - 0.41\left(\frac{a}{W}\right) + 18.7\left(\frac{a}{W}\right)^2 - 38.48\left(\frac{a}{W}\right)^3 + 53.85\left(\frac{a}{W}\right)^4\right) \qquad (2.2)$$

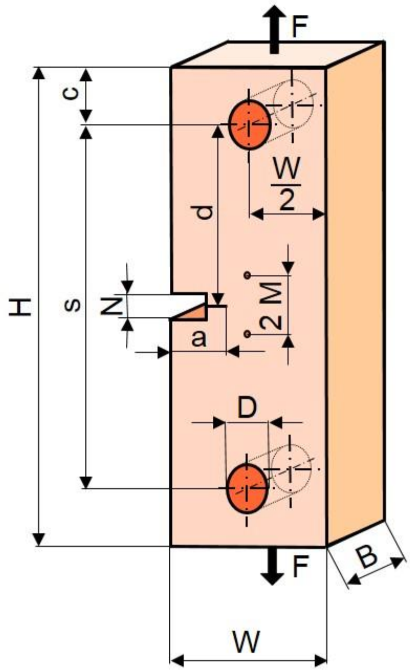

Fig. 2.4: SENT-specimen geometry; B: specimen thickness, W: specimen width, a: crack length (Lexikon der Kunststoffprüfung)

In order to compare different materials in fatigue testing, so-called “fatigue fracture curves” (ΔK_I as a function of the corresponding number of cycles at failure for different load levels) are plotted on a half logarithmic plot. Both slope and position of each curve can be used for material ranking (Arbeiter et al., 2015; Berer et al., 2014; Berer et al., 2018).

2.3 Relationship between morphology and fracture mechanical behavior

Numerous morphological aspects influence the crack propagation behavior in semi-crystalline polymers. They include entanglement and the molecule density, molecular weight (M), molecular weight distribution (MWD) or amount of crystallinity. With a high M the likelihood of crazing rises, ultimately leading to a reduction of the fatigue crack growth rate. With a high degree of tie molecules (TM) and entanglements the force needed to resolve those rises, resulting in an improved crack growth resistance. This can be achieved by a high M with a narrow MWD since long polymer chains form TM and entanglements more easily (Hertzberg and Manson, 1980) or by bimodal MWD to simultaneously reduce melt viscosity and increase both processability and crack growth resitance. Plummer et al. showed that the K_{IC} for crack initiation drops with decreasing entanglement density. A higher entanglement density can be achieved by increasing the cooling rate, resulting in higher K_{IC} values (Plummer et al., 1995).

The degree of crystallinity in semi-crystalline polymers has a crucial influence on the fracture mechanical behavior of such. Compared to amorphous polymers, semi-crystalline polymers show a better performance in fracture mechanical tests. This can be attributed to their crystalline structures. In addition to dissipating energy, when crystallites are deformed, they are also capable of reforming into exceedingly strong structures (Hertzberg and Manson, 1980; Koo and Roldan, 1972; Meinel and Peterlin, 1971). The mechanical properties of semi-crystalline polymers are largely determined by the presence of molecular bonds between the crystalline regions (TM and entanglements). Without those connections, which are composed of covalent bonds, the crystallites would be only held together by weak van der Waals and hydrogen interactions. This would cause the crystallites to easily slip past each other, leading to a more brittle material behavior. TMs have been recognized to not only improve the short-term properties, but to also have a tremendous influence on the long-term properties of semi-crystalline polymers as well. An increase in M as well as a reduction of lamellar thickness results in a higher TM and entanglement density, leading to an increase in tensile strength and improvement in resistance to slow crack growth (Seguela, 2005).

The previously mentioned influence of TM and entanglements on the fracture mechanical properties of semi-crystalline polymers is rather difficult to determine precisely. During crack propagation in semi-crystalline polymers, craze-like features have been observed, resulting in in load-direction oriented molecules in front of the crack tip. This means that a former isotropic material becomes non-isotropic when the crack passes by (Narisawa and Ishikawa, 1989; Plummer et al., 1994). Since folded chains get stretched while lamellae get broken during this process, it is difficult to assess the precise influence of the TM and entanglement density of the original isotropic material on the mechanical behavior (Seguela, 2005).

2.4 X-Ray scattering and diffraction

In polymer science, measurements with X-rays play an important role as non-destructive methods to examine the morphology of polymers. X-rays are transverse electromagnetic waves like visible light and radio waves. The wavelengths of X-rays used in material analysis methods range from 0.5 to 2.5 Å. When high-energy electrons impinge on a metal target like copper or iron, X-rays are emitted. During the measurement a collimated X-ray beam is sent through a specimen and gets scattered and diffracted by the inner structures of the material. The result is a specific pattern that is recorded by a detector, which is located on the backside of the sample (Alexander, 1969; Guinier, 2013).

Electromagnetic radiation satisfies Einstein’s law of the wave-particle duality and therefore both entities (wave and particle) must be considered during interpretation: the particle property leads to scattering of X-rays and the wave property causes diffraction. Patterns obtained from X-ray measurements are not only dependent on the material structure but also on the state of the sample in terms of various aspects like temperature, stress or processing history. Both sample thickness and especially the sort of X-ray radiation affect the measurement time. For instance, a high energetic radiation like from a synchrotron shortens the measurement time significantly (Alexander, 1969; Guinier, 2013).

2.4.1 Small-Angle X-ray Scattering (SAXS)

SAXS is an analytical methodn which is used to identify the structural properties of particle systems in relation to averaged particle sizes or shapes. The particle entity of electromagnetic radiation reveals information about the structure of the tested material in the range of 1-100 nm (Schnablegger and Singh, 2013). SAXS includes scattering angles up to 2 or 3° (Alexander, 1969). Photons (electromagnetic particles) have two different main interactions with the electrons of the matter: absorption and scattering. If a material is irradiated with X-rays, a fraction will be absorbed and transformed into other forms of energy, e.g. heat, a fraction will pass through the material without any interaction and a fraction will be scattered. These interactions between X-ray photons and electrons are illustrated in Fig. 2.5. Irradiation of atoms with X-ray photons can lead to expelling of electrons from such atoms. The energy of the X-ray is consumed by this process and an absorption of the photon occurs. Since no relevant information about the structure of the material can be obtained with absorption, it will not be further discussed. Scattering can either occur with or without the loss of energy. Compton scattering (inelastic scattering) not only leads to change of direction of the beam, but also to a loss of energy, which results in a change of the wavelength. Inelastic scattering only contributes background noise to a scattering pattern and does not carry any structural information. The more disordered the sample is, the more inelastic scattering occurs. This leads to the need to separate the inelastic from the elastic scattered parts of the curve for quantitative studies of amorphous or highly disordered polymers. Rayleigh scattering (elastic scattering) occurs, when photons collide with electrons without energy transfer. The photons get absorbed by the electrons, which start oscillating at the same frequency as the incoming radiation. Due to this oscillation, the electrons emit radiation with the same frequency but different direction. These waves can be detected at a detector leading to scattering patterns which give information about particle structure (Alexander, 1969; Schnablegger and Singh, 2013). Since more electrons lead to more scattering, this method can be used to characterize structures consisting of regions with different electron densities (Schnablegger and Singh, 2013). As the amorphous and crystalline regions of a polymer have different electron densities, information on the lamella thickness and the thickness of the amorphous layer can be obtained by SAXS. Furthermore, SAXS provides information about the arrangement of the lamellar and amorphous regions within a sample. Patterns of randomly oriented samples obtained from the SAXS measurements show circles. If the material is oriented, the patterns take an elliptical shape; the stronger a sample is oriented, the sharper the edges of the ellipse become. The orientation direction of the lamellae can be derived from such patterns. A two-point SAXS pattern is an indicator for a non-tilted, parallel arrangement of the lamellae. A tilting of the lamellar structure can lead to a four-point SAXS pattern (Gerasimov et al., 1974; Hirose et al., 2014). Fig. 2.6 displays an arrangement of a tilted lamellar structure and of a non-tilted lamellar structure as well as their corresponding SAXS patterns.

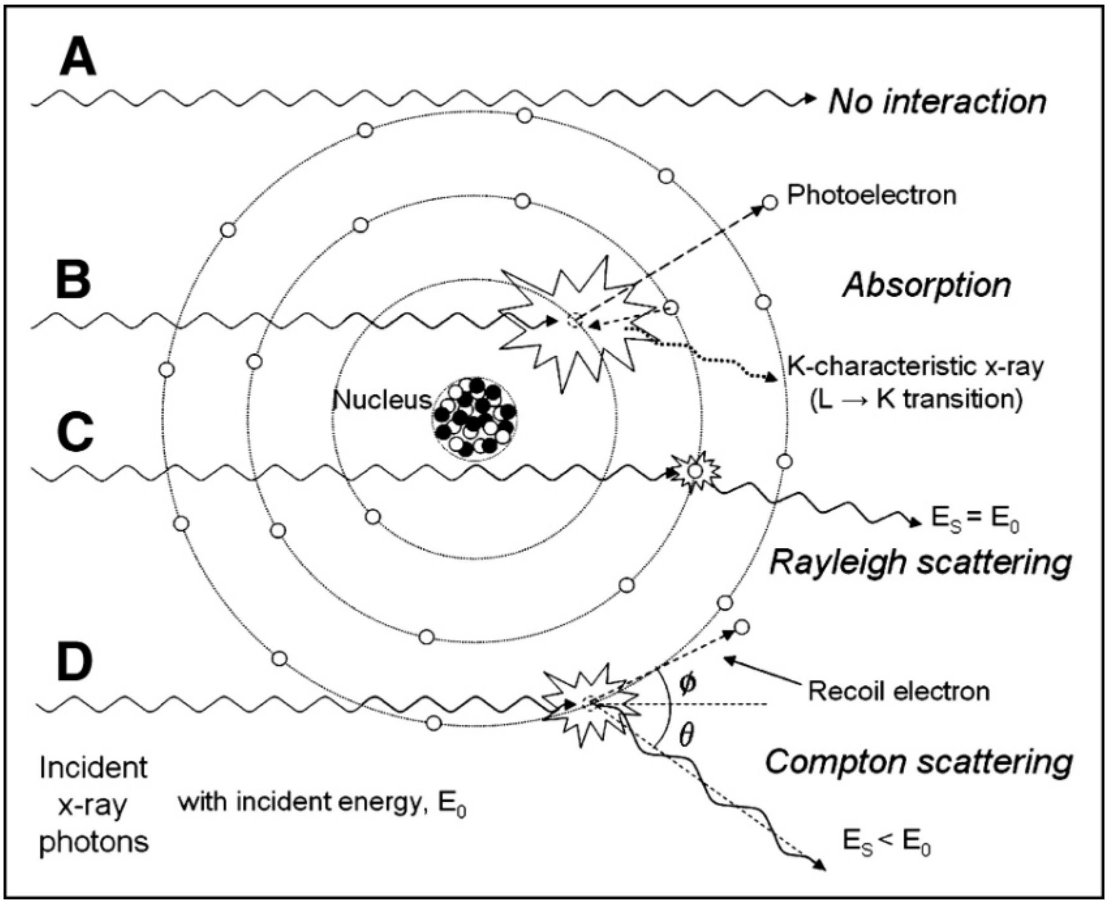

Fig. 2.5: The different ways of interaction between X-ray photons and electrons: (A) no interaction, (B) absorption, (C) inelastic scattering and (D) elastic scattering (Jeffries, 2014)

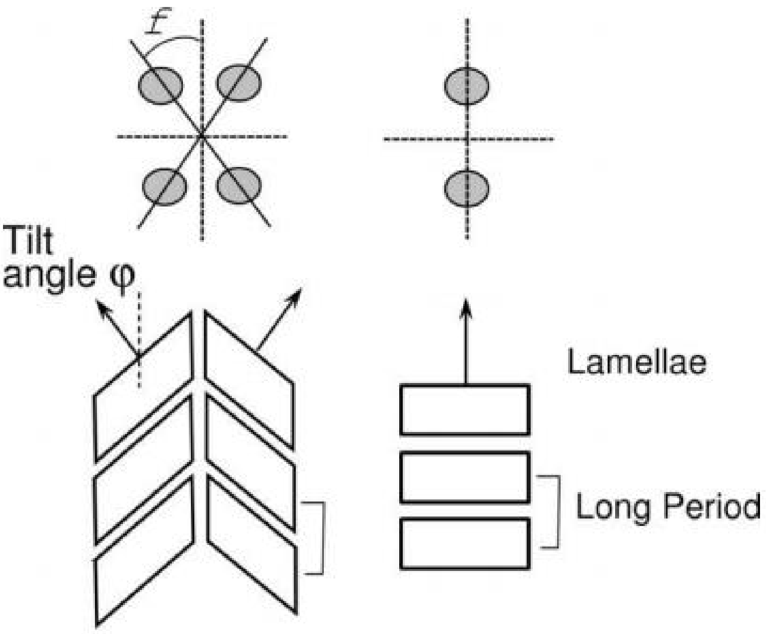

Fig. 2.6: Tilted lamellar structure (left) and non-tilted lamellar structure (right) with their corresponding SAXS patterns (Hirose et al., 2014)

2.4.2 Wide-Angle X-ray Diffraction (WAXD)

Diffraction is a sign for the wave nature of electromagnetic radiation and gives rise to positive (constructive) and negative (destructive) interference. Constructive interference can only be observed if the wavelength of the incoming wave is in the same order of the repeating distance between the diffracting objects. For instance, in order to obtain information about crystals, the wavelength should be in the order of Angstrom. This condition is fulfilled when using X-ray radiation and therefore, it gives information about the crystalline structure of the material (Pecharsky and Zavalij, 2009). If a beam hits a repetitive structure like a crystal, a part gets reflected by every single lattice plane of the crystal. After reflection, waves can interfere in a constructive or destructive way with each other. Waves cancel each other out when destructive interference occurs. Constructive interference occurs, when Bragg's Law (Eq. (2.3)) is satisfied. It gives rise to the characteristic diffraction pattern of the material (Bragg and Bragg, 1913). WAXD can theoretically include diffraction angles up to 180°, but for polymers the diffraction effects are observed at angles well below 90° (Alexander, 1969). In Fig. 2.7 the illustration of Bragg's Law is portrayed.

$$n\,\lambda = 2\,d\ \sin\theta \tag{2.3}$$

where n is the interference order, λ is the wavelength of the incidence beam, d is the lattice constant and θ is the half scattering angle.

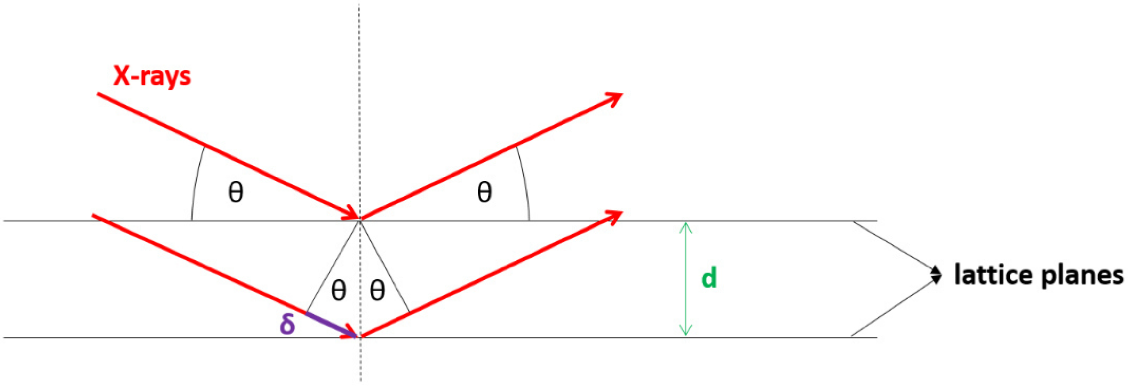

Fig. 2.7: Illustration of Bragg's Law (2θ: scattering angle; d: lattice constant; δ: path difference) (Schrank, 2019)

WAXD measurements on semi-crystalline polymers yield information about the crystalline fraction, the orientation of the crystalline structures and the crystalline structures themselves (more precisely about the crystal lattice as well as the unit cell on which the crystal lattice is based on). Patterns obtained by WAXD measurements consist of several Debye-Scherrer rings that give information about the orientation of the crystal lattice planes. Each group of lattice planes is responsible for a distinct ring in the pattern. The preferred orientation direction of such planes is perpendicular to the axis of the intensity maxima (Alexander, 1969). In order to better understand the various diffraction effects, the following chapter gives a short overview of unit cells, crystallographic planes and reciprocal lattices.

2.4.3 Unit cells, crystallographic planes and reciprocal lattices

A basic knowledge of morphological structures of matter and particularly of crystals is crucial for interpreting different diffraction patterns. The smallest repetitive units in a crystal are called unit cells. Unit cells are three-dimensional structures, which can be distinguished by the length of their edges (a, b and c) and the three angles defined by those edges (α = ∠bc, β = ∠ac and γ = ∠ab). All natural crystal structures can be assigned to one of seven crystal systems, from which one can derive 14 Bravais space lattices. The seven crystal systems as well as their properties are summarized in Table 2.1 (Alexander, 1969).

Table 2.1: The seven crystal systems occurring in nature

System	**Axial Translations (unit cell constants)**	**Angles between Crystal Axes (degrees)**
Triclinic	$a \neq b \neq c$	$\alpha \neq \beta \neq \gamma \neq 90$
Monoclinic	$a \neq b \neq c$	$\alpha = \beta = 90 \neq \gamma$
Orthorhombic	$a \neq b \neq c$	$\alpha = \beta = \gamma = 90$
Tetragonal	$a = b \neq c$	$\alpha = \beta = \gamma = 90$
Hexagonal	$a = b \neq c$	$\alpha = \beta = 90; \gamma = 120$
Rhombohedral	$a = b = c$	$\alpha = \beta = \gamma \neq 90$
Cubic	$a = b = c$	$\alpha = \beta = \gamma = 90$

A family of crystallographic planes is defined as a collection of planes that intersect all lattice points. Each plane in the same family is parallel to every other plane as well as equally spaced. By using the so-called Miller indices, three integer indices h, k and l, one can fully describe a family of crystallographic planes. In order to obtain the Miller indices, the reciprocal of each lattice vector a, b and c has to be formed. When describing a plane, a triplet of Miller indices is always parenthesized: (hkl). When a plane is parallel to a crystallographic axis, its corresponding Miller index is set to 0 (Pecharsky and Zavalij, 2009).

The concept of a reciprocal lattice was first introduced by (Ewald, 1921) and is a mathematical concept to help visualizing and describing periodic diffraction patterns. In Fig. 2.8, an example of the relationship between the direct and reciprocal lattices and the corresponding diffraction patterns is illustrated. Important to note is that a set of an infinite number of crystallographic planes in the direct lattice is represented by a single vector in the reciprocal lattice (Pecharsky and Zavalij, 2009).

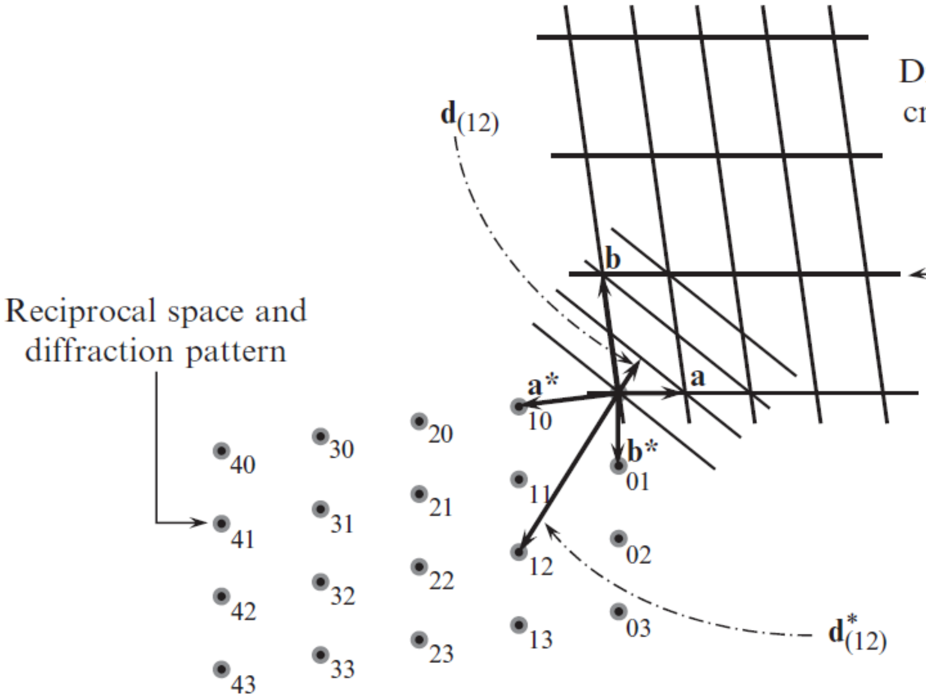

Fig. 2.8: Example of converting crystallographic planes in the direct lattice into points in the reciprocal lattice with corresponding Miller indices near the points in the reciprocal lattice (Pecharsky and Zavalij, 2009)

A specific characteristic of polymer crystals is that a unit cell can be built from monomers of one or more molecule chains. For an orthorhombic POM (o-POM) the unit cells are built of two neighboring chains while a trigonal POM (t-POM) consists of unit cells with only one polymer chain (Lüftl et al., 2014) (please refer to chapter 2.1 for more details).

2.5 Injection molding

Nowadays injection molding is the most important plastic manufacturing process with more than one-third of all thermoplastic materials being injection molded. It is an ideal method for producing complex mass-production parts requiring high dimensional precision. An injection molding machine consists of the following basic components: the plasticizing unit, the clamping unit and the mold (Isayev and Kamal, 2009; Osswald and Hernández-Ortiz, 2006). Fig. 2.9 illustrates an injection molding machine with these basic components.

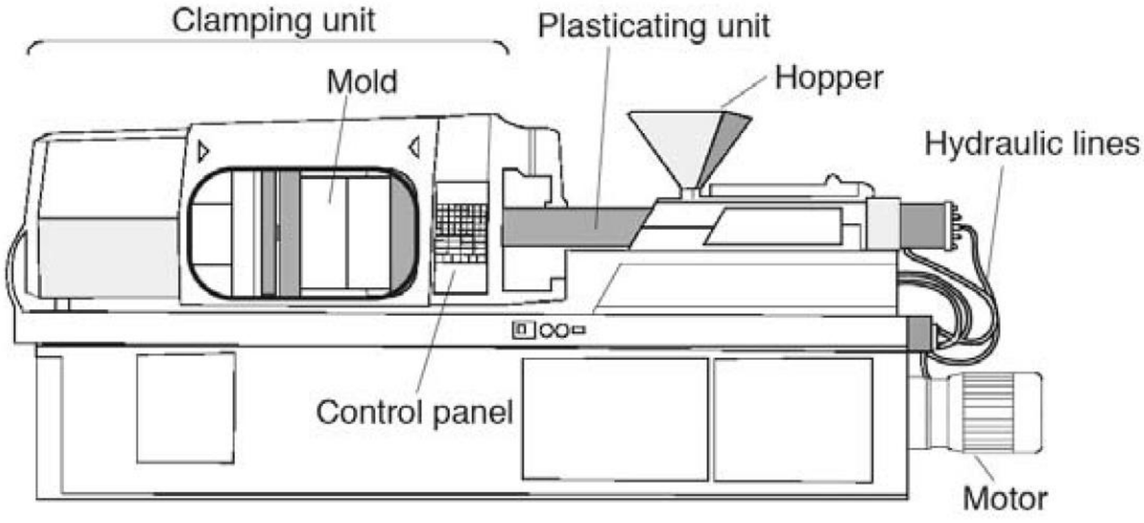

Fig. 2.9: Scheme of an injection molding machine (Osswald and Hernández-Ortiz, 2006)

Polymer granulate typically gets continuously fed into the plasticizing unit via a hopper and is melted within the barrel of the unit. The material is plasticized by using heating bands that are attached to the barrel and due to shear, which is induced by a rotating screw inside the barrel. The screw not only introduces shear, but also homogenizes and conveys the material. To create space for the molten material in front of the barrel, the screw also moves axially. During the plasticizing process, when the screw moves backwards, the space in front of the screw tip is filled with molten polymer. When this process is finished, the screw gets pushed forward, forcing the melt through a die into the mold. In order to compensate for the shrinkage of the material, additional material is pushed into the cavity during the so-called packing or holding phase. After the gate has frozen it is not possible to push more material into the cavities. The time until the gate is frozen is the so-called sealing time. As soon as the polymer gets pushed into the mold, the cooling phase starts. During this phase, the polymer remains in the mold and cools down further. The material cannot shrink and warp freely during this phase since it is partially constraint by the stiff mold. After the cooling phase is finished, the part is ejected by a suitable ejection system e.g. mechanically triggered ejector pins (Isayev and Kamal, 2009; Rosato et al., 2000).

A basic injection mold consists of two halves, one fixed on the side of the plasticizing unit and the other one attached on a moving part on the opposite site. The runner system in the fixed mold half is responsible for delivering the molten polymer from the die through the gate into the cavities, which determine the shape of the finished part. Temperature control is achieved via cooling channels in the mold, through which cooling fluids like pressurized water or oil is funneled. The clamping unit is responsible for sealing the two mold halves together. It applies a clamping force to overcome the separation force caused by the in-cavity pressure during the process to avoid molding defects such as flashing (Isayev and Kamal, 2009; Mennig and Stoeckhert, 2013).

2.5.1 Influence of different injection molding parameters on the morphology

In general, the morphology of polymers is determined by the manufacturing process. Since the properties of the part strongly depend on parameters like crystallinity and orientations, it is crucial to understand the influence of processing parameters on the morphological features and mechanical behavior of the final part. The degree of crystallinity is both dependent on the processing, especially the temperature conditions, and influencing the mechanical properties (Isayev and Kamal, 2009; Rosato et al., 2000). Due to higher shear rates, the melt temperature in the injection molding rises with increasing injection speed. This results in a higher degree of crystallinity due to longer crystallization times. A higher cooling rate (achieved by lower mold temperatures) leads to smaller spherulites and a lower degree of crystallinity in semi-crystalline polymers. A lower cooling rate, on the other hand, increases both the spherulite size and the crystallinity fraction, as the melt has time to crystallize more thoroughly (Singh and Moslé, 1988).

The cross-sectional morphology of injection molded semi-crystalline polymers shows a skin-core structure with usually three different layers. The skin region is located on the outside of the part, where the melt is in contact with the mold surface during the injection molding process. Due to the high cooling rate, which exists in this layer, the crystallinity is usually smaller in this area. The core region is found in the middle of the part, where a lower cooling rate is observed. This allows a better relaxation of the polymer chains and the growth of spherulites. The region that separates the skin and core layers is called the shear zone. It is predominantly defined by the high shear deformations near the wall. Each layers' thickness is dependent on a variety of process conditions like mold temperature, injection speed/pressure, holding pressure and cooling time (Liu et al., 2002; Rosato et al., 2000).

The cavity melt flow gives rise to the orientations in the finished part. Fig. 2.10 shows the flow of the polymer melt in a mold cavity in the direction from left to right. The polymer chains in the melt front get oriented perpendicular to the main flow direction as the melt front gets stretched. This orientation gets preserved due to fast cooling as the layer touches the cold mold surface. A zone, which is dominated by the shear flow is right behind the melt front. Here one part of the layer is connected to the skin region following its way, while the other one is dragged into the direction of the main flow. This results in an orientation in 45° to the main flow direction. The polymer chains in the core of the part also get oriented due to shear and velocity gradients. The closer to the centerline, the smaller the orientation is here (Isayev and Kamal, 2009; Rosato et al., 2000).

A higher injection speed increases the orientation in the skin layer. Such speeds lead to a high shear thinning of the material near the mold wall. As a result, the core flows in between those shear thinned layers. This reduces the shear in the core zone, minimizing the orientation in the center of the part. At a slower injection speed, shear thinning decreases and the mold has more time to cool the melt, resulting in a more uniform orientation over the entire part (Rosato et al., 2000). Compared to the injection speed, the mold temperature has a weaker influence on the orientations in the part. A colder mold increases the orientation in the core area as the melt cools down faster, reducing the time polymer chains have for relaxation. The orientation direction of the skin layer is not affected by the mold temperature (Liparoti et al., 2016). If the holding pressure is increased, the orientations increase as well. This can be explained both, with the creep flow, which can occur during the holding phase, and with the reduction of the melt relaxation (Rosato et al., 2000).

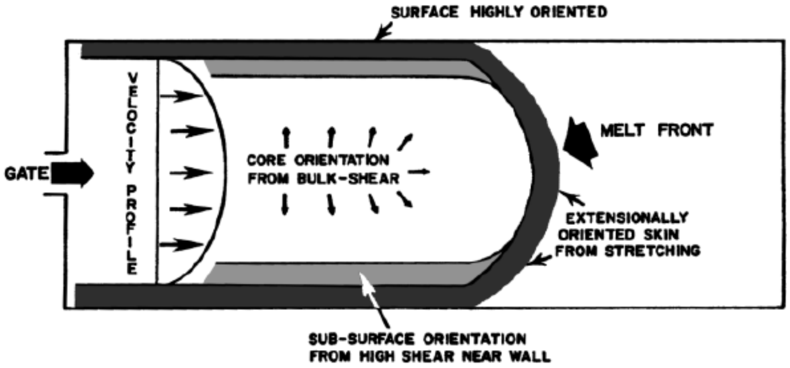

Fig. 2.10: Flow of the polymer melt during filling of the cavity (Rosato et al., 2000)

3 EXPERIMENTAL DETAILS

3.1 Material

In this study a POM homopolymer of the type Delrin 111PF provided by DuPont (DuPont de Nemours, Wilmington, United States) was analyzed. The average molecular weight (M_w) of this material is 149,000 g/mol and the polydispersity index (PDI) is 2.6. These values were obtained by gel permeation chromatography and published in (Berer et al., 2018).

3.1.1 Processing

In order to analyze the influence of the processing conditions on the morphology and fracture mechanical properties of POM, small platelets (26 mm x 15 mm x 0.8 mm) were produced in April 2018 at eight different injection molding conditions. The production was carried out on an Arburg Allrounder 470A 1000-400 Alldrive (ARBURG GmbH & Co KG, Loßburg, Germany) injection molding machine following a design of experiments (DOE), in which mold temperature (T_{mold}), injection speed (v_{inj}) and packing pressure ($p_{packing}$) were varied (Table 3.1). All other processing parameters were kept as constant as possible during the different conditions.

Table 3.1: DOE for the small platelets ($p_{packing}$ is given in % of the filling pressure)

Processing Condition	**T_{mold} (°C)**	**v_{inj} (mm/s)**	**$p_{packing}$ (%)**
C1	40	6	60
C2	40	6	100
C3	40	76	60
C4	40	76	100
C5	110	6	60
C6	110	6	100
C7	110	76	60
C8	110	76	100

3.2 Methods

3.2.1 X-ray scattering and diffraction

X-ray measurements were performed in two runs. To get an overview of the morphology of the platelet, the first run consisted of a scan over the whole specimen, where nine points on the sample were measured (Fig. 3.1). The second run consisted of measurements at point 6 and 8. This allowed a good comparison between the morphology and fracture mechanical properties of the specimen, since the notch for the fracture mechanical characterization was in the region of point 8 (refer to Chapter 3.2.2 for details). The measurements of point 6 were conducted to verify the stability of the injection molding process. One specimen per condition was analyzed in the first measurement series; in the second run three specimens per condition were tested. For each point, the SAXS and WAXD measurements were conducted simultaneously. Fig. 3.2 illustrates the position of the sample inside the measuring chamber. The ejection pin marks are on the side of the plate, which is not in contact with the sample holder (facing the detector).

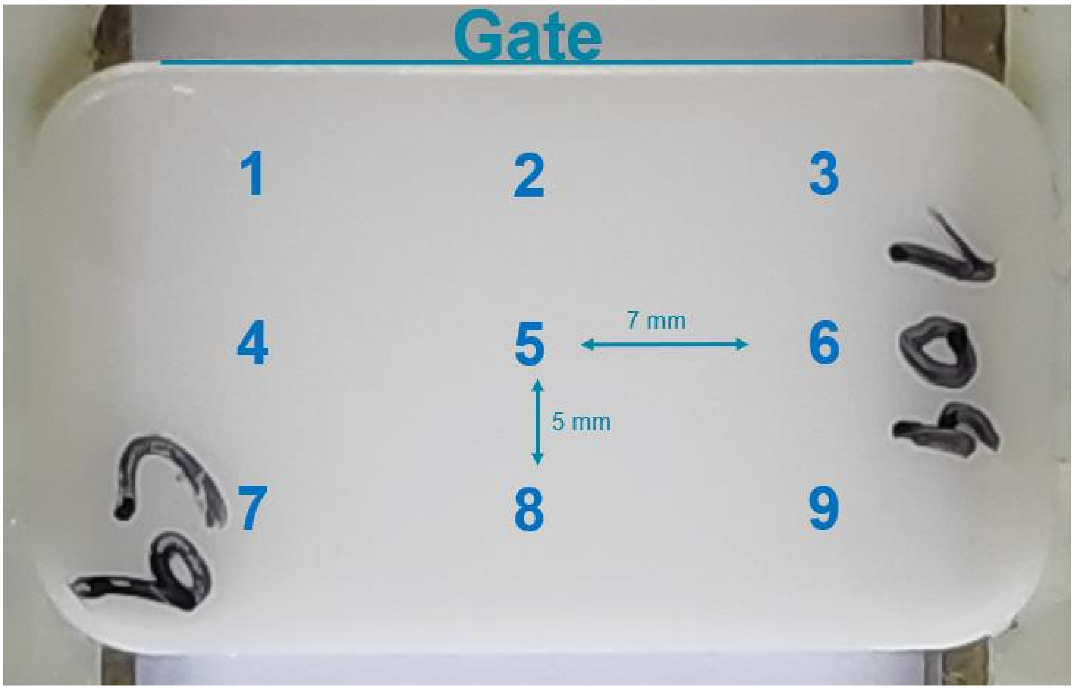

Fig. 3.1: X-ray beam positions for the SAXS/WAXD measurements

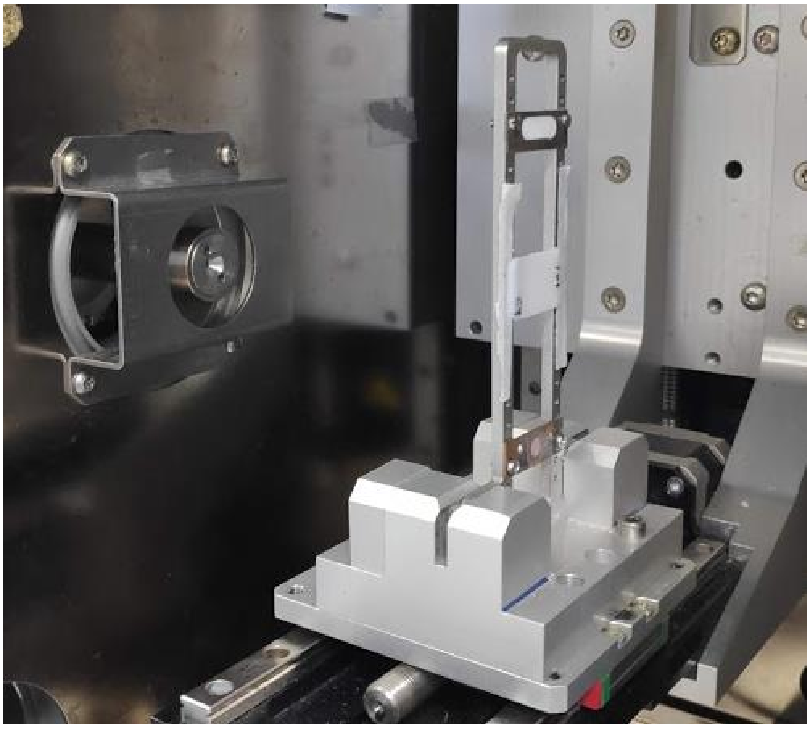

Fig. 3.2: Position of the sample inside the measuring chamber with the X-Ray source on the left side and the detector-side on the right

The X-ray measurements were performed on a Bruker Nanostar (Bruker Corporation, Massachusetts, USA) with an Iµ X-ray source (Incoatec GmbH, Geesthacht, Germany). The X-ray source provided monochromatic radiation with a wavelength of 1.5418 Å that was focused by circular slits with a diameter of 550 µm (first run) and 300 µm (second run). In order to record the SAXS measurements, an automatic detector of the type VÅNTEC-2000 2D MicroGap (Bruker Corporation, Massachusetts, USA) approximately 1097 mm behind the sample was used. The WAXD experiments were captured using an image plate with a central hole around 40 mm behind the sample. To determine the exact distances between the sample and the detectors, silver behenate standard for the SAXS detector and aluminum oxide standard for the WAXD detector were used. Fig. 3.3 illustrates the setup that allows simultaneous SAXS and WAXD measurements. For both measurement series the irradiation time was kept at 1500 s and the samples were placed in an evacuated measuring chamber. The integration of the SAXS and WAXD patterns was carried out using a software tool called "Fit2d" (Hammersley, 2016) which was provided by the European Synchrotron Radiation Facility (ESRF, Grenoble, France).

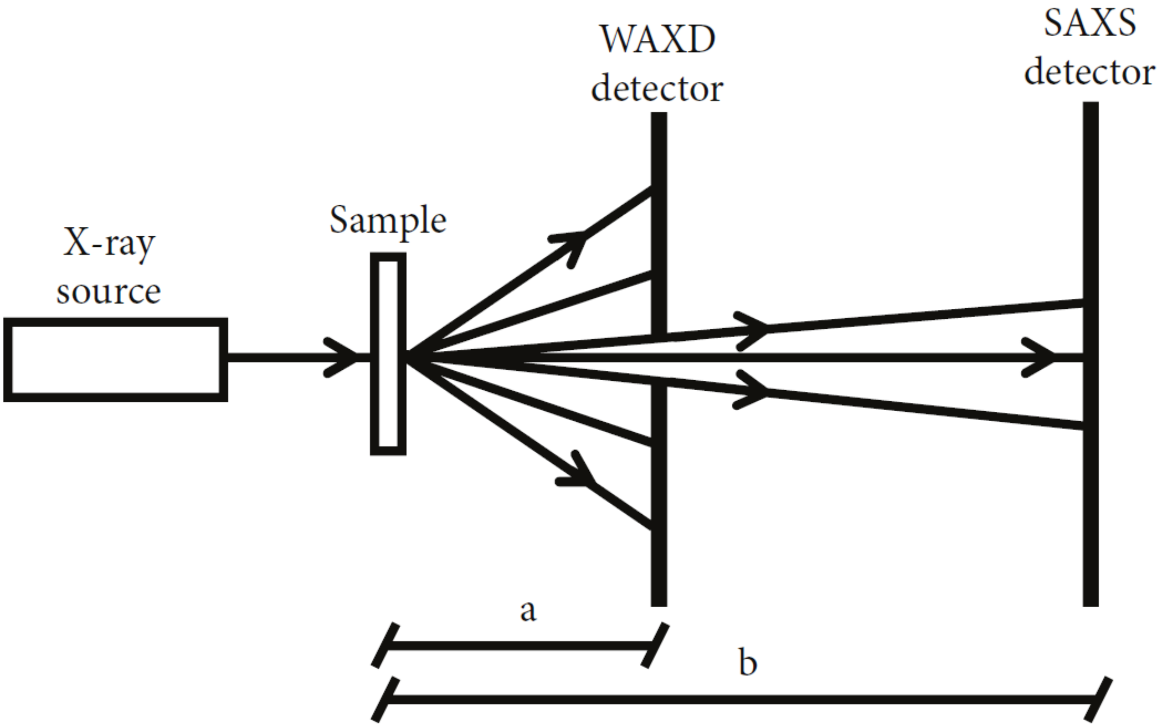

Fig. 3.3: Setup for simultaneous SAXS and WAXD measurements (a was around 40 mm and b was approximately 1097 mm for all tests) (Berer et al., 2018)

In order to better interpret patterns obtained from the X-ray measurements, they were converted into 1D-plots (profiles) by the use of the Fit2d software tool. There are two different ways to generate such profiles: the radial integration and the azimuthal integration. For the radial integration, the data points were integrated in a circle (ϕ-direction) for every radial point starting from the central point and moving outwards (q- or Θ-direction) following Eq. (3.1). For the azimuthal integration, the patterns were integrated in radial direction for every angle ranging from 0° to 360° following Eq. (3.2). The directions for the radial and the azimuthal integration of SAXS and WAXD patterns are displayed in Fig. 3.4.

$$I(q) = \int_0^{2\pi} I(q,\phi)\, d\phi \qquad (3.1)$$

$$I(\phi) = \int_{q_{min}}^{q_{max}} I(q,\phi)\, dq \qquad (3.2)$$

q is the scattering vector and ϕ is the pole angle around the beam center. Eq. (3.3) defines q, where 2θ is the scattering angle and λ is the wavelength of the incident X-ray beam (Alexander, 1969):

$$q = 4\pi * \sin\frac{\theta}{\lambda} \tag{3.3}$$

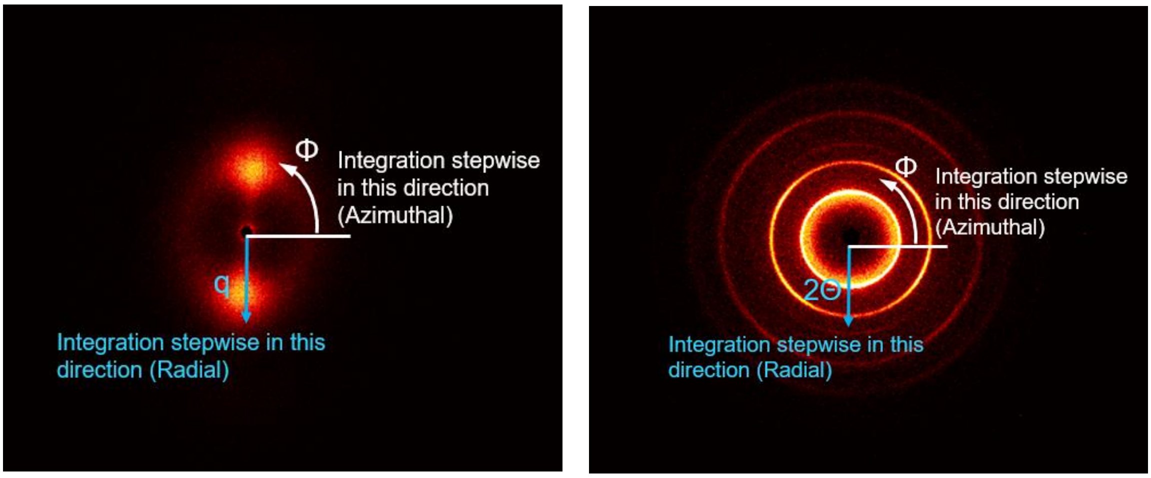

Fig. 3.4: Radial and azimuthal integration of SAXS (left) and WAXD (right) patterns

3.2.1.1 Evaluation of SAXS

Fig. 3.5 illustrates a typical SAXS profile obtained from radial integration. Two different approaches can be used to interpret these profiles: the “1D correlation” (Strobl and Schneider, 1980) and the “3-component model” (Hama and Tashiro, 2003b). When using the 1D correlation on POM, a part of the information about the morphological state is lost since it is based on a two-phase model. In order to prevent this loss of information, Hama and Tashiro developed the 3-component model, which assumes the existence of three distinct phases in POM (Hama and Tashiro, 2003b). A study by (Berer et al., 2018) on the same type of resin did not yield satisfying results, when using the 3-component model and thus only the 1D correlation was used for the analysis in the present study. MATLAB (MathWorks Inc., Natick, Massachusetts, USA) scripts, written and provided by Dr. Michael Berer (Polymer Competence Center Leoben, Austria), were used for the calculations and intermediate steps in the analysis.

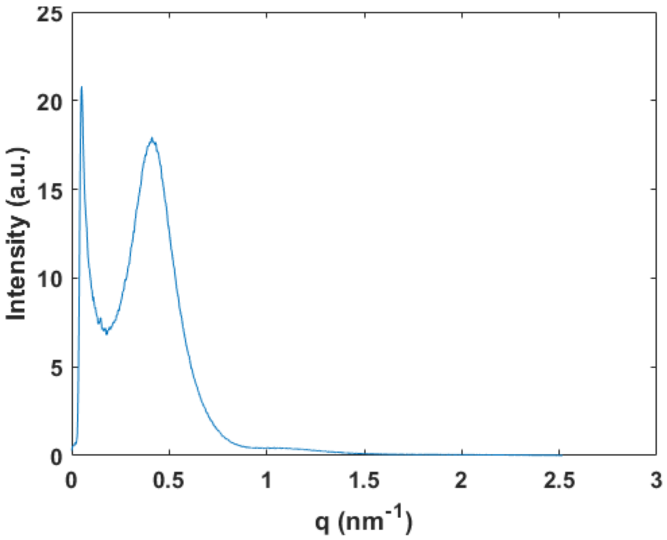

Fig. 3.5: SAXS profile obtained by radial integration

The analysis with the 1D correlation technique requires the entire SAXS profile (from q=0 to q->∞). Due to experimental limitations, it is not possible to obtain the whole curve with experiments alone. Therefore, the curve had to be extrapolated. The extrapolation to q=0 and to high q (q=∞) was carried out according to (Strobl and Schneider, 1980). Afterwards, the background scatter was subtracted from the entire profile. A normalized correlation function was generated since the measured intensities were not obtained as absolute values. Fig. 3.6 illustrates the analysis of this correlation function. The layer thicknesses as well as the volume degree of crystallinity were calculated using the first minimum and maximum of this function. For the calculation of the degree of crystallinity Eq. (3.4) was used. Important to note is that this equation is only valid for samples with a degree of crystallinity higher than 50% (Strobl and Schneider, 1980). (Berer et al., 2018) showed that the type of resin used in this study has a crystalline fraction of more than 60% and therefore Eq. (3.4) can be used on Delrin 111PF.

$$X_{C,1D} = 1 - \frac{l_a}{LP} \tag{3.4}$$

where l_a is the amorphous layer thickness and LP is the long period. These two parameters can be obtained from the correlation function (Fig. 3.6). The thickness of the lamella (l_c) can be calculated by Eq. (3.5).

$$l_c = LP - l_a \tag{3.5}$$

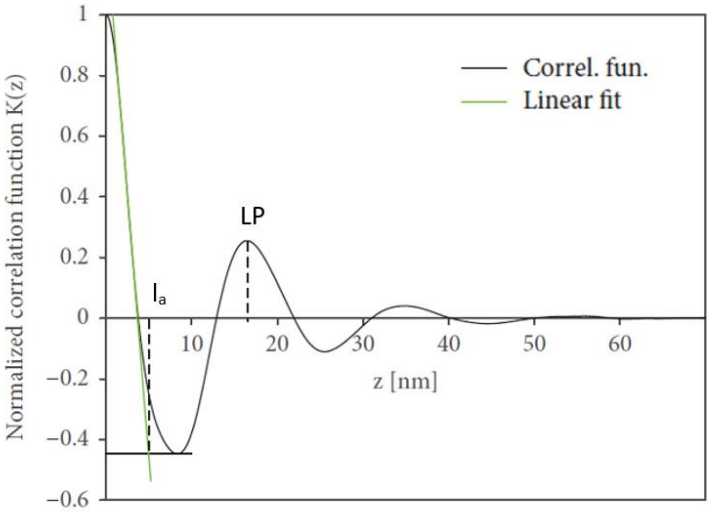

Fig. 3.6: Example of a correlation function of SAXS patterns obtained for POM (l_a - amorphous layer thickness; LP - long period) (Berer et al., 2018)

With a SAXS profile obtained by azimuthal integration, the orientation direction and the degree of orientation (ρ) of the lamellar structures in POM can be evaluated. The orientation direction can be determined by allocating the maxima of the profile. In Fig. 3.7 the determination of ρ in an azimuthal SAXS profile is illustrated; ρ is the ratio between the peak areas (turquois) and the whole area (turquois + green) (Alexander, 1969).

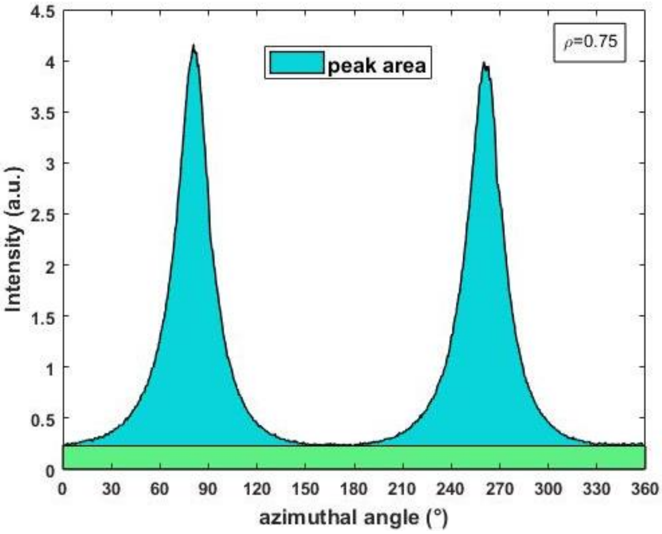

Fig. 3.7: Determination of the degree of orientation from an azimuthally integrated SAXS pattern

3.2.1.2 Evaluation of WAXD

A WAXD pattern consists of several defined Debye-Scherrer rings (Fig. 3.4), where each ring can be attributed to a specific group of parallel crystal planes. When radially integrated, each ring leads to a distinct peak in the obtained profile. A typical WAXD profile of POM with peaks fitted for the calculation of the crystalline fraction ($X_{C,WAXD}$) is given in Fig. 3.8. Additionally, the Miller indices of the corresponding crystalline planes are displayed for the peaks according to (Shimomura, 1993). To obtain the amount of the amorphous phase, the amorphous halo was fitted according to (Zhao and Ye, 2011). The mass degree of crystallinity was calculated from the areas of the fitted peaks by Eq. (3.6), where a_c is the area under the crystalline peaks and a_a the area of the amorphous halo.

$$X_{C,WAXD} = \frac{a_c}{a_c + a_a} \tag{3.6}$$

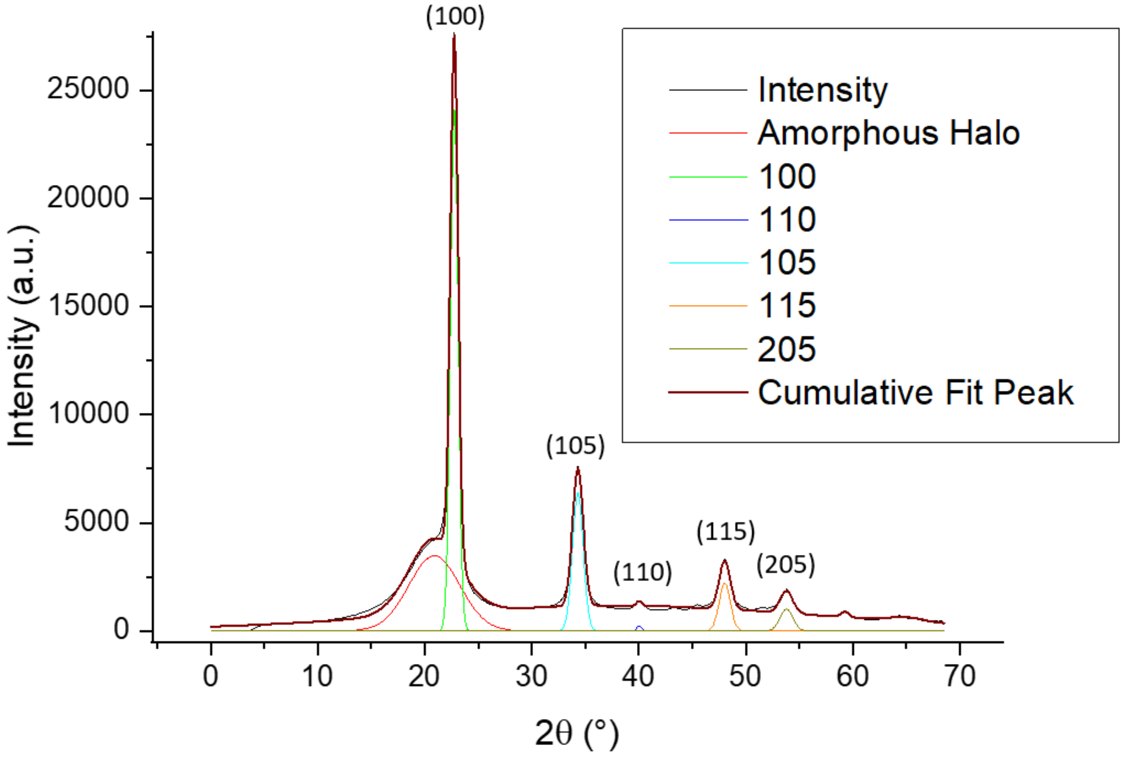

Fig. 3.8: WAXD profile obtained by radial integration with fitting curves

To evaluate the orientation of the crystalline structures in POM, the degree of orientation (ρ) (described in the previous chapter for SAXS) as well as the so-called "Herman's orientation function" (f_ϕ) were used. The Herman's orientation function gives the extent of orientation to the axis of interest as a function of the angle (ϕ) between the crystal axis and the axis of interest (Eq. (3.7)). It provides a value of -0.5 for perpendicularity to the axis, 0 for random orientations and 1 for parallel alignment with the axis (Alexander, 1969). The calculation of f_ϕ was done in Matlab. Fig. 3.9 displays the direction for the values -0.5 and 1 on a tested platelet. For this analysis only the most inner ring, which corresponds to the (100) plane, was used.

$$f_\phi = \frac{3 * \langle \cos^2 \phi \rangle - 1}{2} \tag{3.7}$$

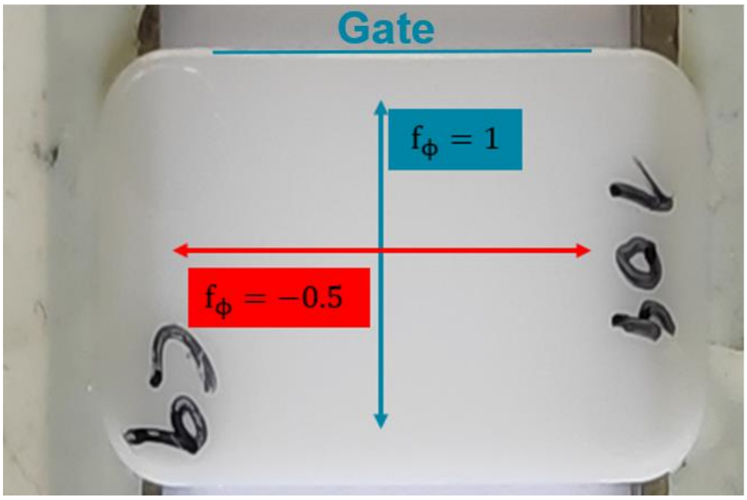

Fig. 3.9: Direction of the crystal plane orientations for the Herman's orientation function at values of -0.5 and 1 on a platelet (axis of interest is perpendicular to the gate direction)

3.2.2 Fracture mechanical characterization

For the fracture mechanical characterization of the different processing conditions, monotonic and fatigue fracture tests were carried out. So-called "µ-SENT specimens", which were cut out from the injection molded platelets, were used in all tests. In Fig. 3.10, the dimensions and cutting of the µ-SENT specimens as well as the position of the initial crack are displayed. The width of 8 mm was chosen to fulfill the requirement of the standards (ASTM E 0647 and ASTM E 399) ($\frac{W}{B} \leq 10$) and to obtain plane strain condition. An electro dynamic testing machine of the type ElectroForce 3230 (Texas Instruments Incorpareted, Dallas, United States) was used for the fracture mechanical tests. All tests were done at room temperature with a clamping length of 15 mm.

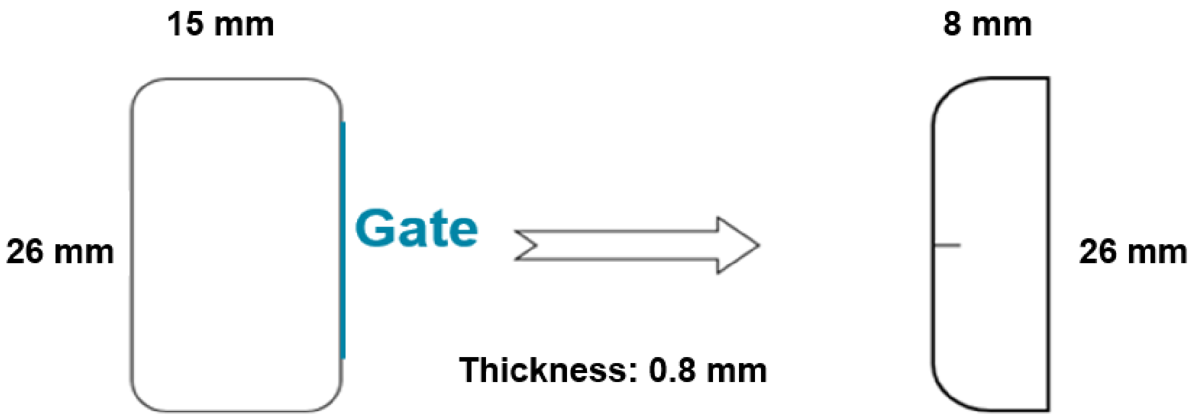

Fig. 3.10: Injection molded platelet (left) and µ-SENT specimen (right)

3.2.2.1 Monotonic testing

In monotonic testing, four samples per condition were used for each test setting. The tests were carried out using two different testing speeds (10 mm/min and 100 mm/min). A razor blade was pushed into the specimen to create a sharp initial crack of around 1 mm. In order to verify if the obtained values for the fracture toughness were independent on the initial crack length, additional tests with different initial crack lengths (0,5 mm, 2 mm and 4 mm) were carried out. Here, the initial crack was introduced by sliding a razor blade using a "LEICA RM2255" microtome (Leica Biosystmes, Wetzlar, Germany). Four specimens per condition at two different testing speeds (10 mm/min and 100 mm/min) were examined in this verification test. K_C was calculated according to (ASTM E 399 - 19).

3.2.2.2 Fatigue testing

For the fatigue tests, a load ratio R (minimum load/maximum load) of 0.1 and a sinusoidal signal with a frequency of 10 Hz were chosen. All tests were conducted in load-controlled mode. As in the monotonic tests, the initial crack of roughly 1 mm was introduced by pushing a razor blade into the specimen. For each processing condition, a fatigue fracture curve was generated. In the beginning, for each condition, two specimens per load level at three different load levels were tested. These load levels can be found in Table 3.2. In order to obtain missing data points to complete the fatigue fracture curve for each condition, additional load levels were chosen individually for every condition (Table 3.3). The load level 3 (F_{max} = 220 N, F_{min} = 22 N) was repeated for the processing conditions C3, C4, C6 and C7 since the starting crack length in the first measurement run slightly differed from 1 mm, which influenced the ΔK level to sum extend. At each additional load level, two specimens were tested. ΔK was calculated according to (ASTM E 0647-15).

Table 3.2: Basic load levels used for the fatigue fracture tests of all processing conditions (F_{max} and F_{min} are the maximum and minimum load of the signal)

Load level	**F_{max} (N)**	**F_{min} (N)**
1	150	15
2	185	18.5
3	220	22

Table 3.3: Additional load levels used for the fatigue fracture tests (F_{max} and F_{min} are the maximum and minimum load of the signal)

Load level	**F_{max} (N)**	**F_{min} (N)**	**Processing conditions**
4	120	12	C1, C2, C5, C8
5	170	17	C5
6	190	19	C8
7	200	20	C1
8	210	21	C2

3.2.3 Polarized light microscopy

Polarized light microscopy (PLM) was used to examine the microstructure on various cross sections of the POM platelets. Two samples per condition were analyzed with this method. One was cut in flow direction (middle and top), the other one was cut perpendicular to the flow direction (side) (Fig. 3.11). Both samples were embedded in resin after cutting. With a microtome (Reichert Jung, Heidelberg, Germany) thin films of around 20 µm were cut from the embedded samples, placed on a microscope slide and sealed with oil and a thin glass plate. The samples were analyzed using an “Olympus BX51” microscope (Olympus

Corporation, Tokyo, Japan). For the image recording, the transmitted light mode was used and the samples were positioned between two crossed polarizers.

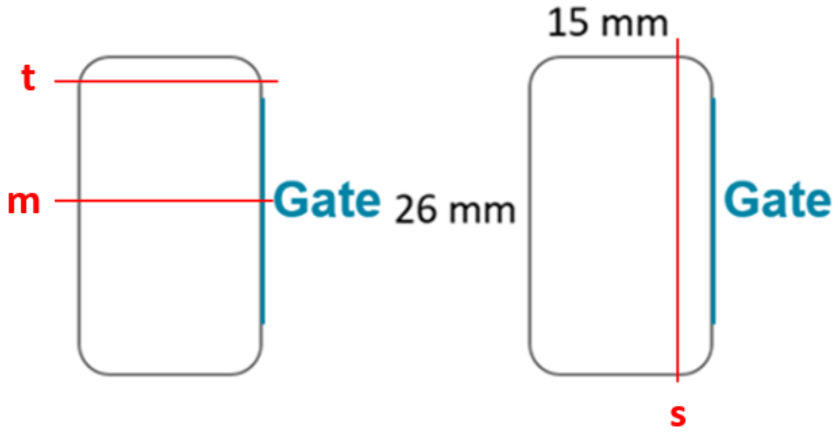

Fig. 3.11: Positions of the cuts for PLM: top (t) -cut was around 2.5 mm from the edge, side (s) -cut was about 3 mm from the edge and middle (m) -cut was around 3 mm from the middle of the sample

3.2.4 Injection molding simulation

Injection molding simulations were carried out in order to better understand the filling behavior in the mold and to help interpret the results obtained from the morphological analysis (especially from the X-ray measurements). The simulation tool used was MoldFlow from AUTODESK (Autodesk Inc., California, United States). 2.5D simulations were carried out to simulate the crystallization process during the manufacturing process. The crystallization parameters were determined experimentally and implemented into the Moldflow crystallization module by the Department of Industrial Engineering at the University of Salerno (Italy). To better display the filling of the mold, 3D simulations were carried out as well. The obtained residual stresses were not plausible and thus, the focus of these simulations was on the filling behavior. It is recommended to carry out further investigations regarding the residual stresses in future studies. In Fig. 3.12 and Fig. 3.13, the viscosity curve as well as the pvT-diagram of Delrin 111PF exported from MoldFlow are given.

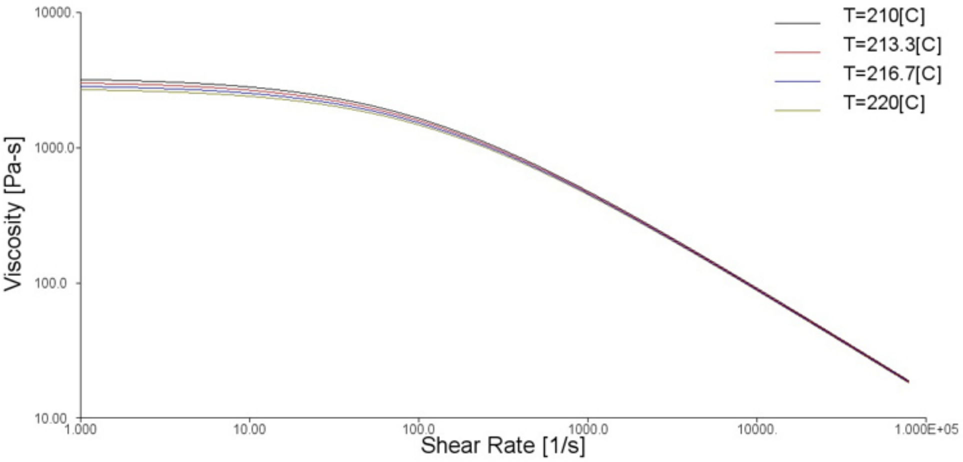

Fig. 3.12: Viscosity curve of Delrin 111PF (exported from MoldFlow)

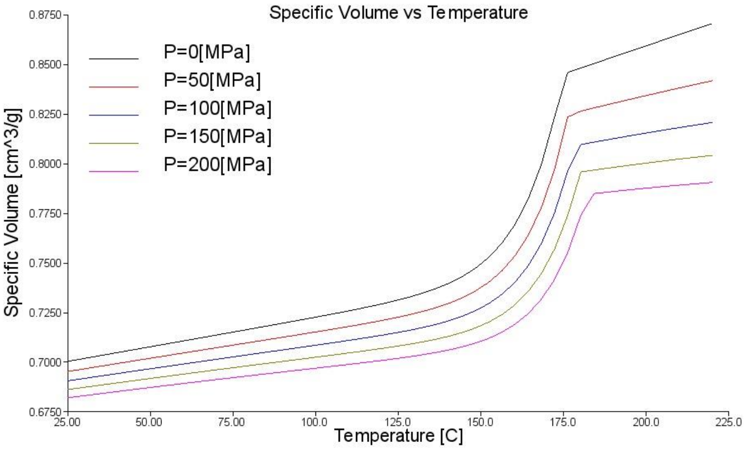

Fig. 3.13: pvT-diagram of Delrin 111PF (exported from MoldFlow)

All simulations were performed after the processing of the platelets. This enabled the implementation of measured processing parameters (e.g. injection time, melt temperature packing pressure) into the simulations. As an example, the (measured) process settings for C1, which were used in MoldFlow are shown in Table 3.4. The mesh for both types of simulations (2.5D and 3D) was generated using the auto-mesh function found in MoldFlow. Since the runner is a major pressure consumer and has a big influence on the filling of the mold, it was included into the model as well. The volume of the part was very small compared to the whole geometry. To assure a good representation of the filling of the part, a very fine mesh quality was chosen. In 2.5D, the sprue was modeled as a beam element (green part in Fig. 3.14). For the 3D simulations, the sprue was also meshed with a three-dimensional mesh.

Table 3.4: Measured process settings for C1, which were used in MoldFlow

Melt temperature	222 °C
Mold-open time	5.1 s
Injection time	2.5 s
Flow rate	1.53 cm³/s
Packing time	2.5 s
Packing pressure	41.4 MPa
Cooling time	5.5 s

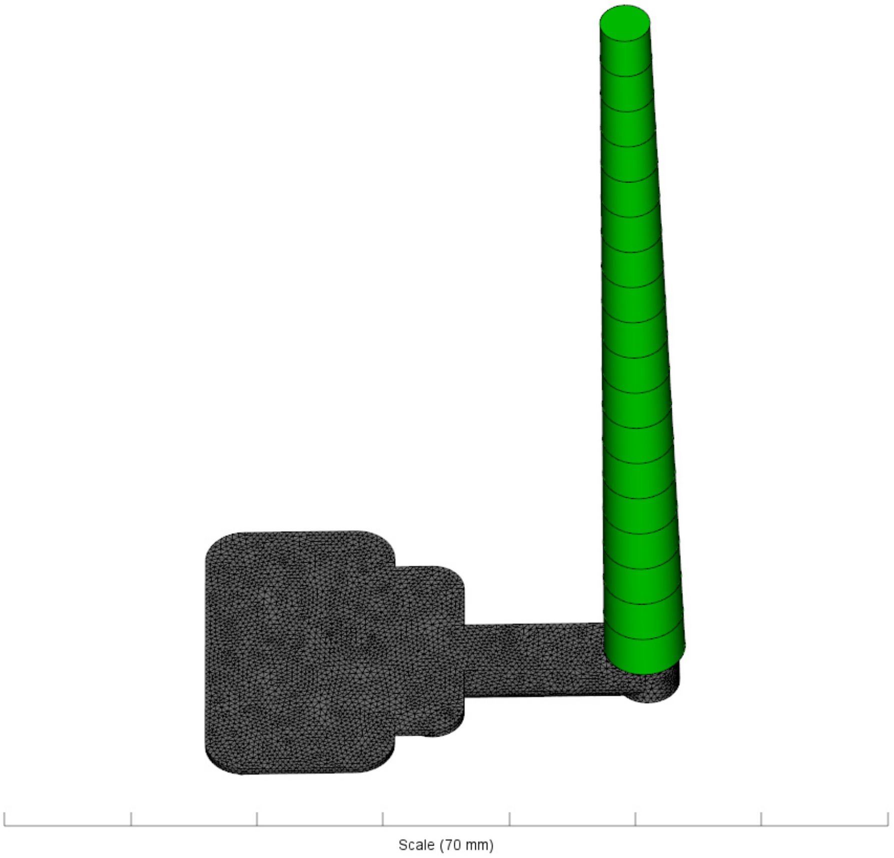

Fig. 3.14: Simulation model for the 2.5D simulations with the meshed geometry and the sprue represented by a beam element (green)

4 RESULTS AND DISCUSSION

It is known that during storage of POM at room temperature, post processing changes can take place. Since about half a year passed between the production and the first measurement of the platelets, it is expected that most of the material changes happened and were finished in that time period. SAXS and WAXD measurements as well as fracture mechanical analysis were very time consuming and thus, not all measurements could be completed within a short period of time. About 6 months passed between the first and last measurement. All test samples were stored in an air-conditioned laboratory at 23°C and protected from light. However, it cannot be fully excluded that the specimens still underwent some small post processing changes, which could have affected the measured properties of the material. The possible aging effect must be kept in mind when interpreting the results. The significance of the influence of the different processing parameters on a specific result was assessed with the statistic software “Minitab” (Minitab Inc., Pennsylvania, United States of America) and a significance level of 5%.

The different processing conditions 1 to 8 are denoted as C1 to C8 in the following. To display the deviation from the mean value (x_{mean}) in the tables, the difference to the maximum (x_{max}) and minimum (x_{min}) values will be used (Eq. (4.1) and Eq. (4.2)).

$$\Delta x_{max} = x_{max} - x_{mean} \tag{4.1}$$

$$\Delta x_{min} = x_{min} - x_{mean} \tag{4.2}$$

4.1 Morphology of POM

4.1.1 X-Ray scattering and diffraction

Hereafter, the results of the SAXS and WAXD measurements will be discussed. For a better understanding, the irradiated positions on the platelets are repeated in Fig. 4.1. The numbers 1 to 9 refer to the measurement positions on the samples. These measurement positions are termed as “p1” to “p9” in the following discussion.

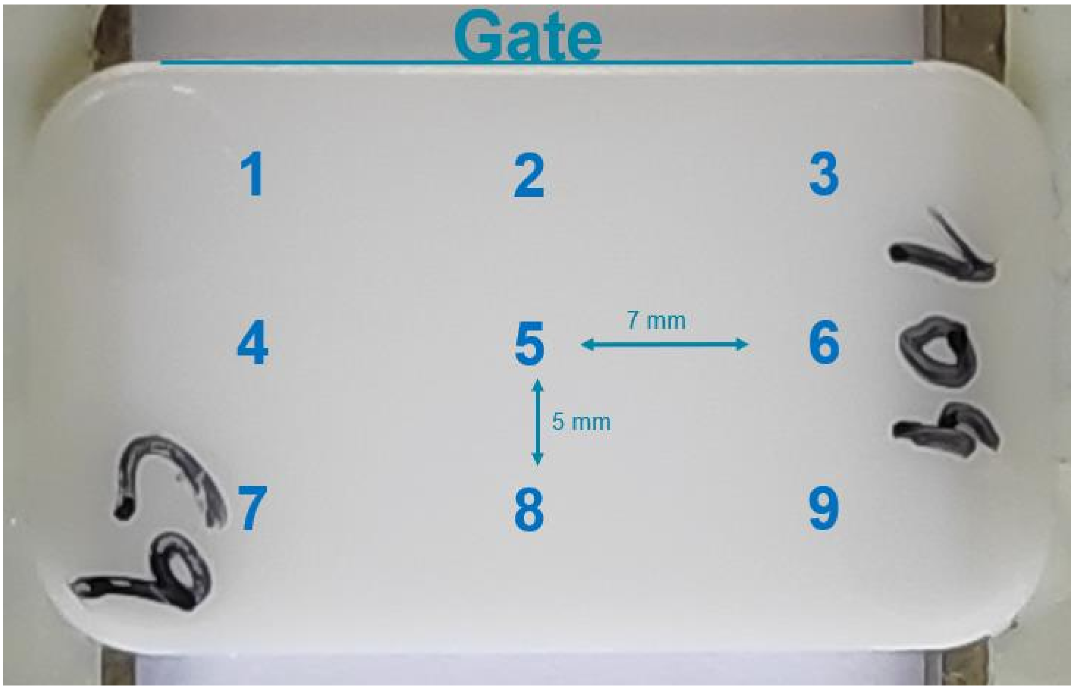

Fig. 4.1: Measurement positions for the analysis of the platelets using SAXS and WAXD

4.1.1.1 SAXS

In Fig. 4.2, SAXS patterns obtained from scans over the whole platelet are displayed for a sample from C1. For the patterns of the other processing conditions (C2 to C8), please refer to the appendix. The maximum intensity of the poles declines from top to bottom, meaning that the orientation factor (ρ) for points farther away from the gate is smaller. As with not fully oriented samples expected, the remaining intensity is distributed over the whole ring. The declining of the orientation is also shown in the azimuthal plots of p2, p5 and p8 (Fig. 4.3). The azimuthal plot for p8 shows a lower maximum intensity compared to p2 and p5 as well as a second orientation direction (0°-180°). However, both orientation directions are less pronounced, resulting in the lowest ρ on the platelet in p8. For a better visualization of the orientation state of the lamellae in the platelet, the suggested preferred lamellar orientations are sketched in Fig. 4.4. The SAXS patterns on both side edges of the platelet resemble a tilted lamellar composition, whereas those in the center (excluding the point at the end of the flow path) show a non-tilted composition of perpendicular to the flow-direction oriented lamellae. In p8, a higher amount of lamellae is oriented in flow direction. In order to explain this orientation of the lamellae, the exact filling behavior of the mold has to be known. For this, the filling simulations, which were carried out with MoldFlow, were used for further interpretations (see chapter 4.4).

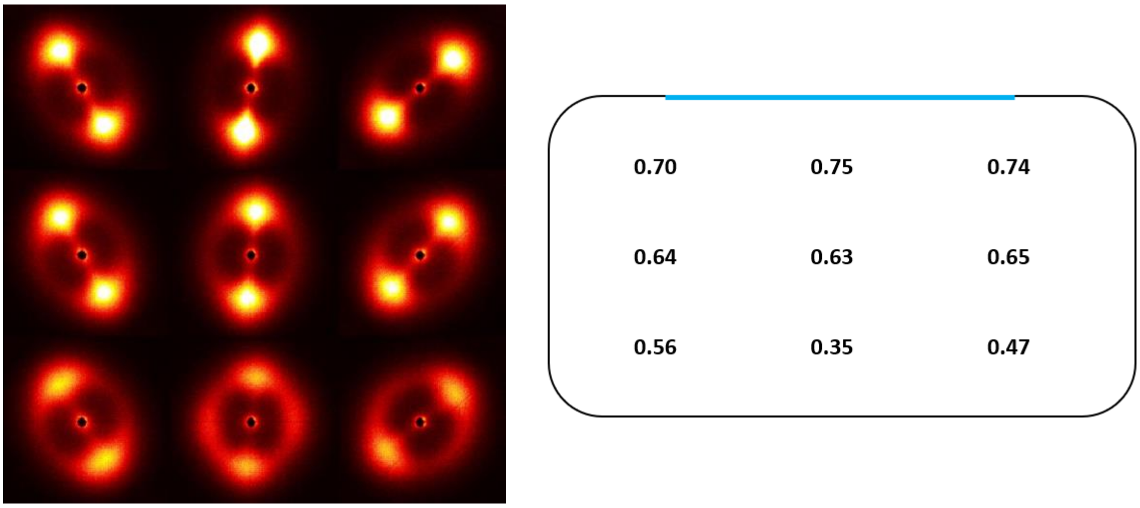

0.70	0.75	0.74
0.64	0.63	0.65
0.56	0.35	0.47

Fig. 4.2: SAXS patterns obtained from scans over the whole platelet for C1 (left) and values of the orientation factor ρ (right) with the blue line marking the gate side (same intensity scale for all plots)

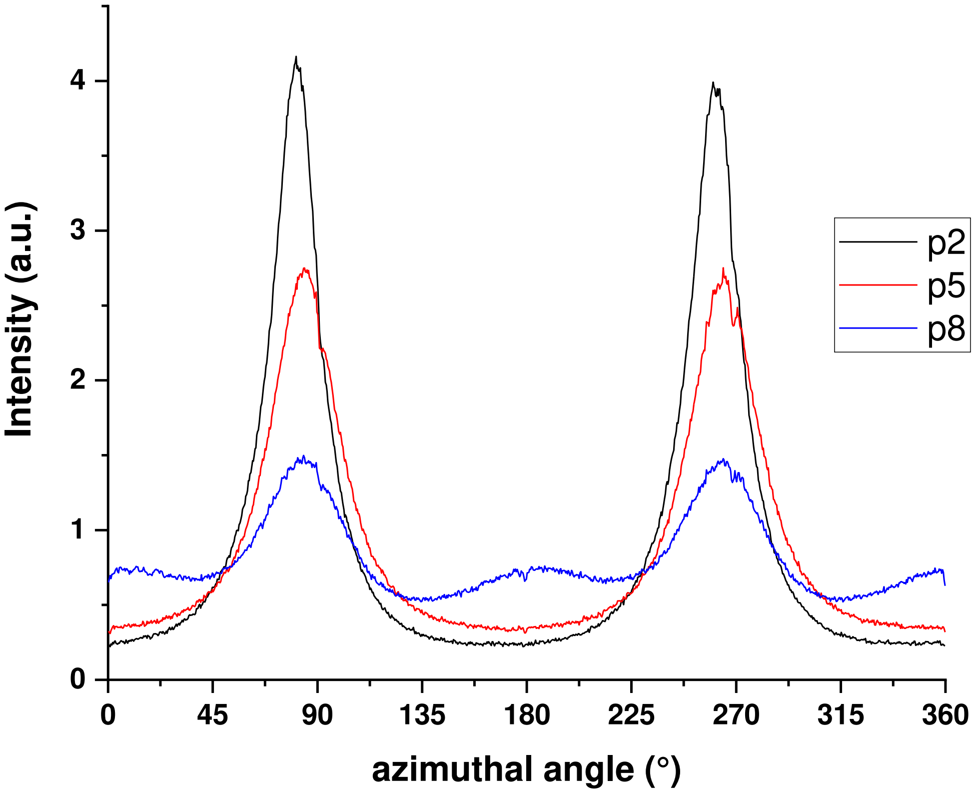

Fig. 4.3: Azimuthal SAXS plot for p2, p5 and p8 of C1

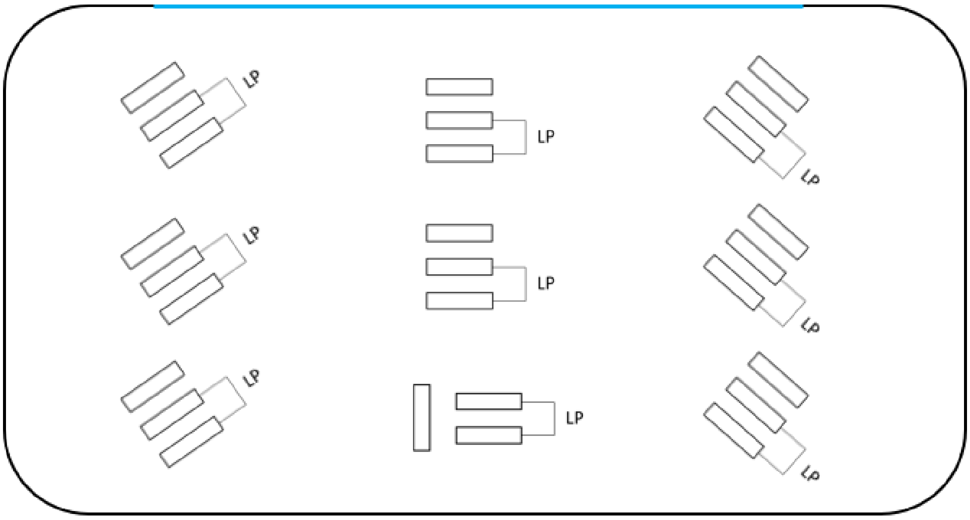

Fig. 4.4: Suggested orientations of the lamellae in a C1 platelet with the blue line marking the gate side

All other conditions except C5 and C6 (high mold temperature and low injection speed) showed a similar SAXS characteristic. For C5 and C6, the lowest ρ was found in the second row (p4-p6). Additionally, the SAXS patterns in p8 showed a more pronounced second orientation direction, meaning more lamellae are oriented perpendicular to the gate. Fig. 4.5 compares the SAXS patterns in p8 for C1 and C5. This suggests a different filling behavior in the mold with the process settings from C5 and C6 compared to the other settings.

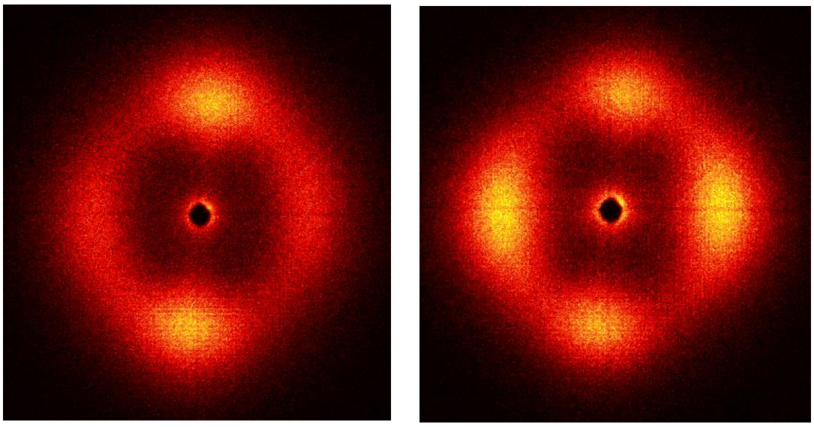

Fig. 4.5: SAXS patterns in p8 for C1 (left) and C5 (right) (same intensity scale for all plots)

The values of the long period (LP) as well as the lamellar thickness (l_c) in p8 for all conditions are given in Table 4.1. These values were used to calculate the volumetric degree of crystallinity, which is shown in Fig. 4.6. All values are average values of three measurements. At higher mold temperatures, an increase of crystallinity as well as LP and l_c can be observed. A smaller temperature difference between melt and mold temperature as well as a lower cooling rate are attributable to this increase. The influence of the injection speed and the packing pressure on the volumetric degree of crystallinity seems to be insignificant. An analysis with Minitab confirmed that both injection speed and packing pressure did not have a significant effect on the crystallinity. Fig. 4.7 illustrates the obtained Pareto chart as an example.

Table 4.1: Long period (LP) and lamellar thickness (l_c) obtained with the 1D correlation

Specimen	**LP (nm)**	**Δx_{max} (nm)** **Δx_{min} (nm)**	**l_c (nm)**	**Δx_{max} (nm)** **Δx_{min} (nm)**
C1	12.05	+0.02 -0.03	8.39	+0.04 -0.02
C2	12.05	+0.03 -0.03	8.36	+0.13 -0.08
C3	11.83	+0.00 -0.01	8.14	+0.06 -0.07
C4	11.79	+0.02 -0.01	8.18	+0.08 -0.06
C5	13.05	+0.02 -0.03	9.17	+0.17 -0.12
C6	12.99	+0.01 -0.03	9.18	+0.06 -0.04
C7	12.87	+0.05 -0.03	9.18	+0.03 -0.04
C8	12.62	+0.05 -0.04	8.90	+0.30 -0.35

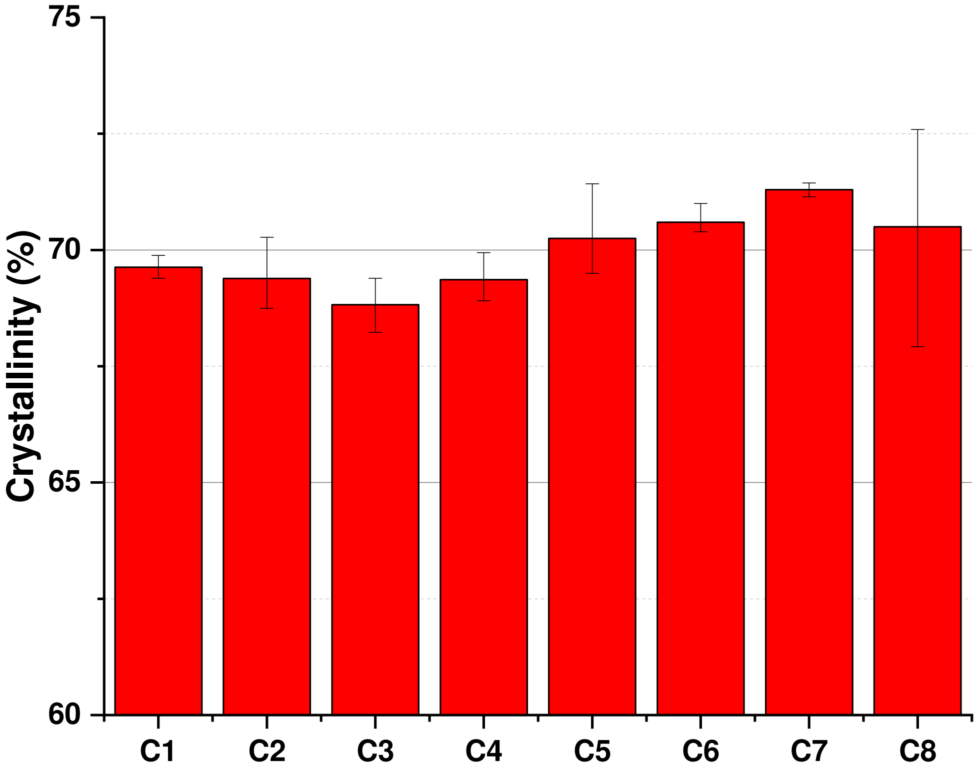

Fig. 4.6: Volumetric degree of crystallinity in p8 obtained with 1D correlation (error bars: maximum and minimum values)

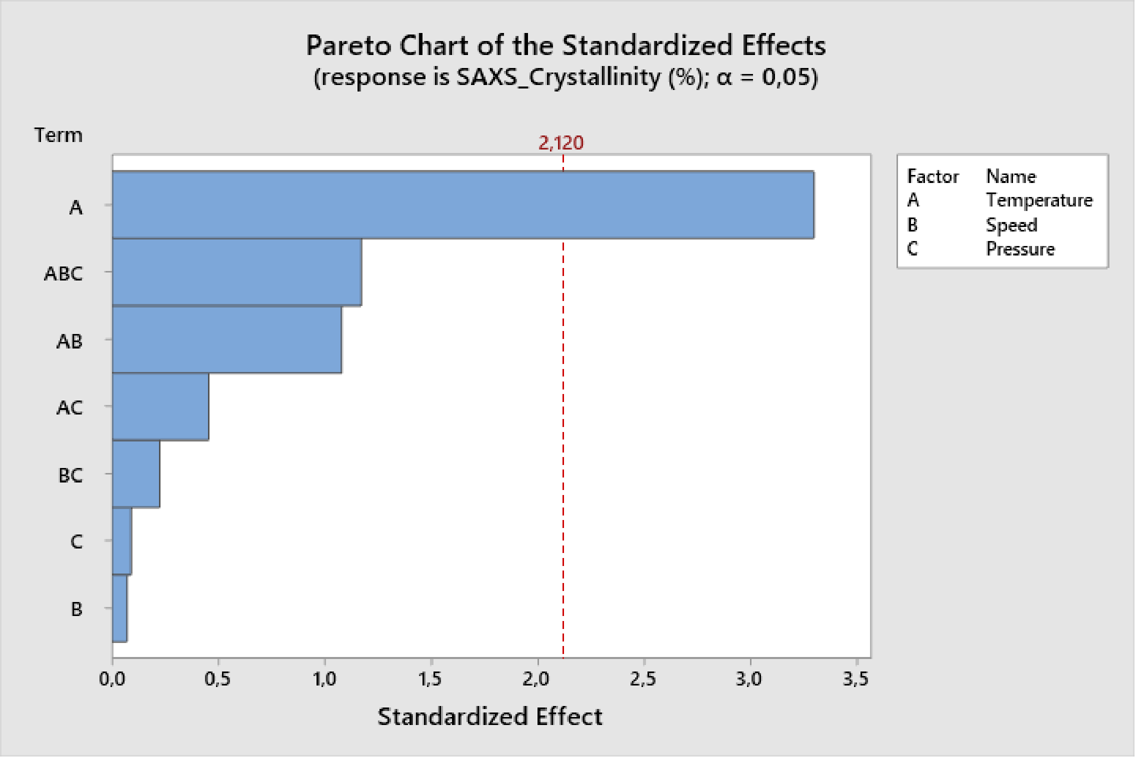

Fig. 4.7: Pareto chart of the standardized effects on the SAXS crystallinity

4.1.1.2 WAXD

Fig. 4.8 illustrates the WAXD patterns obtained from scans over the whole platelet for C1. For the patterns of the other processing conditions (C2 to C8), please refer to the appendix. With increasing distance to the gate, the overall intensity rises, but the intensity of the oriented amount decreases, resulting in a decrease of the orientation factor. For the azimuthal integration only the most inner ring, which corresponds to the (100) planes, was used. If the orientation direction of a set of crystal planes is known, the orientation direction of the whole crystal can be estimated. The decrease of orientation of this crystalline plane is shown by ρ (Fig. 4.8) as well as in the azimuthal plots of p2, p5 and p8 (Fig. 4.9). Contrary to the azimuthal plots obtained by SAXS, for WAXD not only p8 but also p2 and p5 show a second orientation direction. However, the peaks of the second orientation direction for both curves are rather small.

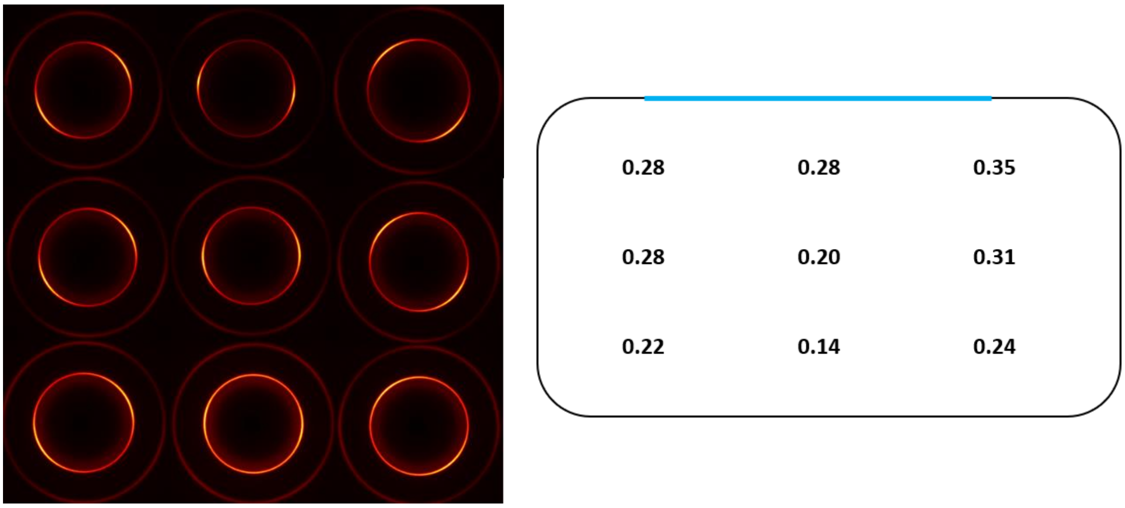

0.28	0.28	0.35
0.28	0.20	0.31
0.22	0.14	0.24

Fig. 4.8: WAXD patterns obtained from scans over the whole platelet for C1 (left) and values of the orientation factor (ρ) (right) with the blue line marking the gate side (same intensity scale for all plots)

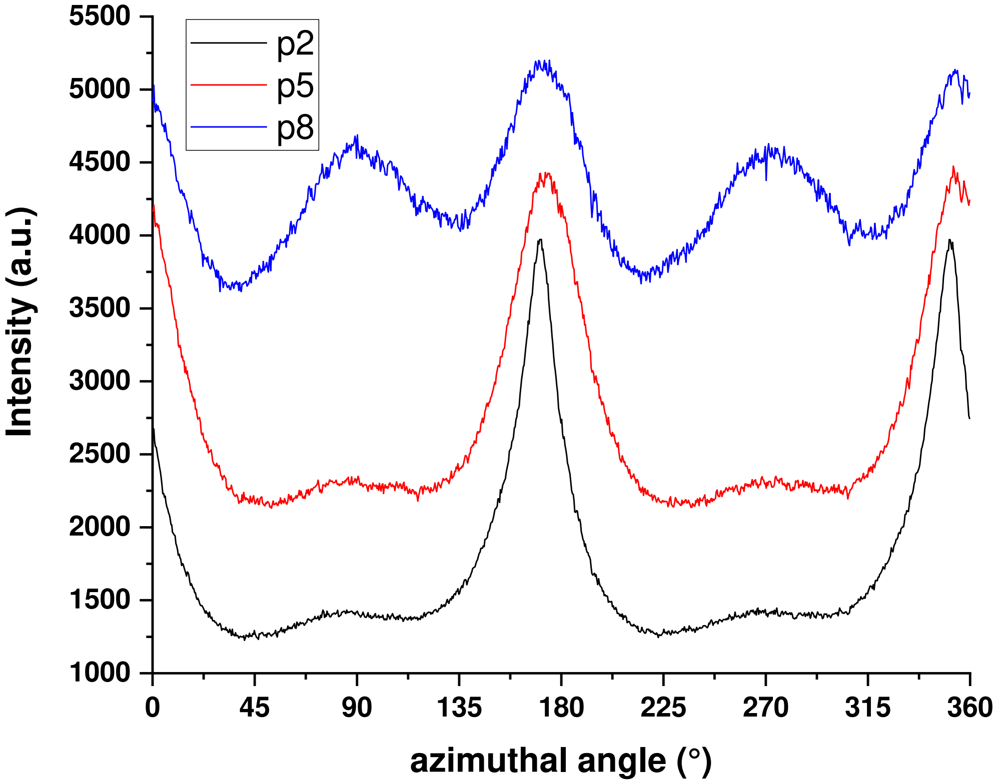

Fig. 4.9: Azimuthal WAXD plot for p2, p5 and p8 of C1

As in the SAXS measurement, from all conditions, only C5 and C6 showed a different behavior. For these conditions, the lowest ρ was in the second row (p4-p6). Fig. 4.10 shows the difference of the WAXD patterns of the (100) planes in p8 for C1 and C5. The change of the crystal plane orientation is apparent in these patterns. This change is attributable to the change of the orientation direction of the whole lamellae as observed in the corresponding SAXS patterns. In POM, the (100) planes are perpendicular to orientation of the lamellae, meaning that the WAXD pattern of the (100) planes has to be perpendicular to the SAXS patterns. This is confirmed by comparing Fig. 4.5 to Fig. 4.10. The WAXD pattern of C1 shows intensity maxima on the left and right side while the corresponding SAXS pattern has its intensity maxima on the top and bottom side.

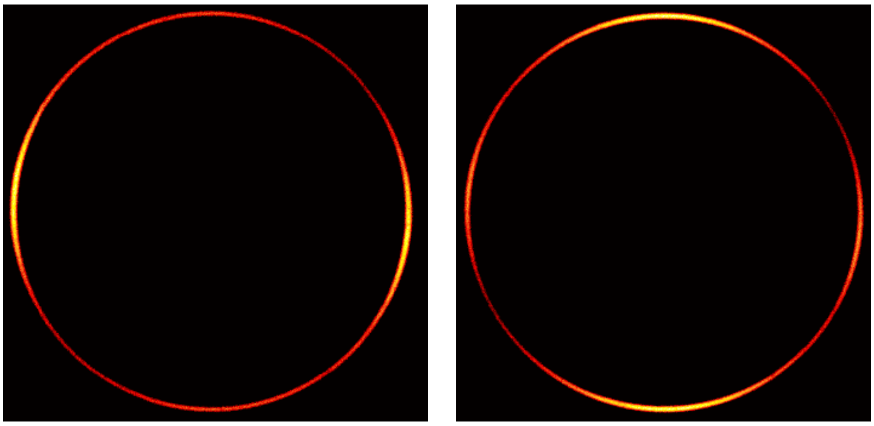

Fig. 4.10: WAXD patterns showing the Debye-Scherrer ring of the (100) planes in p8 for C1 (left) and C5 (right) (same intensity scale for all plots)

The Herman's orientation function was used to help interpret the overall orientation direction of the (100) planes. In Fig. 4.11, the results of the Hermann's orientation function for the whole C1 plate are illustrated. The reference axis of the function is perpendicular to the gate (refer to Fig. 3.9). Hence, a value of 1 represents full orientation in flow direction, -0.5 full orientation perpendicular to the flow direction and 0 no preferred orientation. In p2 and p5, the (100) planes seem to favor one direction. The value at p8 suggests a random orientation of the (100) planes, but the corresponding azimuthal plot clearly shows two defined orientation directions. It has to be mentioned that if the (100) planes have two preferred orientation directions, which are perpendicular to each other, the Hermann's orientation function takes a value close to 0. Since it was designed for one preferred orientation only, it interprets two of them as random orientation. This has to be kept in mind, when interpreting the results of the Herman's orientation function. A further weakness of this function is visible, when Fig. 4.8 and Fig. 4.11 are compared. Although there are clear poles in Fig. 4.8 (e.g. in p1 and p3), the Herman's orientation function indicates random orientation. Hence, for a 45° alignment to the axis of interest in p1 and p3, the Herman's orientation function gives ambiguous results. This makes the method unreliable for the comparison of different positions on the plate. However, the comparison of the different processing conditions at one fixed position is expected to be reliable. Such a comparison will be made in the following for p8.

Fig. 4.11: Herman's orientation function of the platelet for C1 with the blue line marking the gate side

Fig. 4.12 displays the results obtained at the position p8 for the second run (three specimens per condition). At p8, the (100) planes seem to favor an orientation parallel to the gate and thus, perpendicular to the flow direction. According to the results obtained, a higher mold temperature leads to a more pronounced orientation of the (100) planes parallel to the gate. The influence of injection speed as well as packing pressure is higher at lower mold temperatures (C1-C4). A higher injection speed leads to a higher amount of (100) planes being oriented parallel to the gate at lower mold temperatures while a higher packing pressure favors an alignment in two directions (C1-C3). The bigger influence of the injection speed at lower mold temperatures can be explained by the fact that the more oriented polymer chains caused by higher injection speeds are frozen quicker. At higher mold temperatures, the polymer chains have more time for the relaxation process.

Fig. 4.13 illustrates the degree of crystallinity obtained from the WAXD measurements over the whole platelet (p1-9) for C1. If the degree of crystallinity on the left side (p1, p4, p7) is compared to the degree on the right side (p3, p6, p9) of the platelet, it is obvious that the crystallinity is not distributed symmetrically. All other conditions also showed differences between the left and the right side of the platelet regarding the degree of crystallinity, although some had a higher crystalline fraction on the right side. This might be an indicator that the gate is partially frozen at the edges, which leads to a non-symmetrical filling. Which side of the specimen is affected seems to be statistically distributed, but the same side is affected within a certain condition. Regarding the distance to the gate, the crystallinity of the platelet does not change significantly.

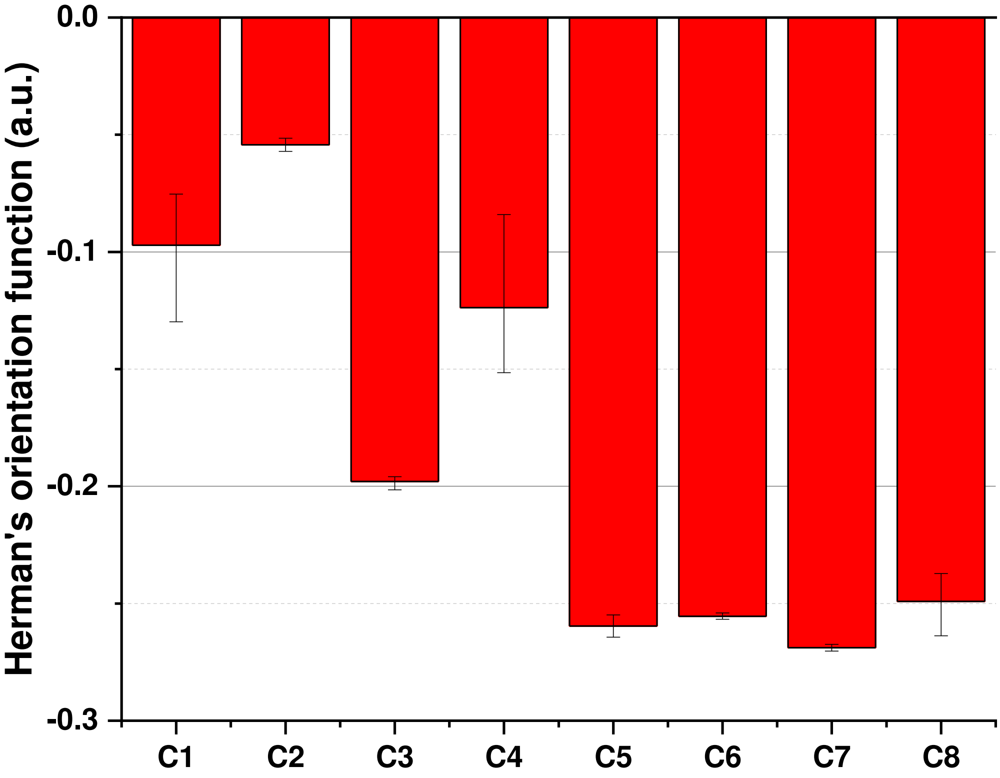

Fig. 4.12: Herman's orientation function for the platelet position p8 (error bars: maximum and minimum values)

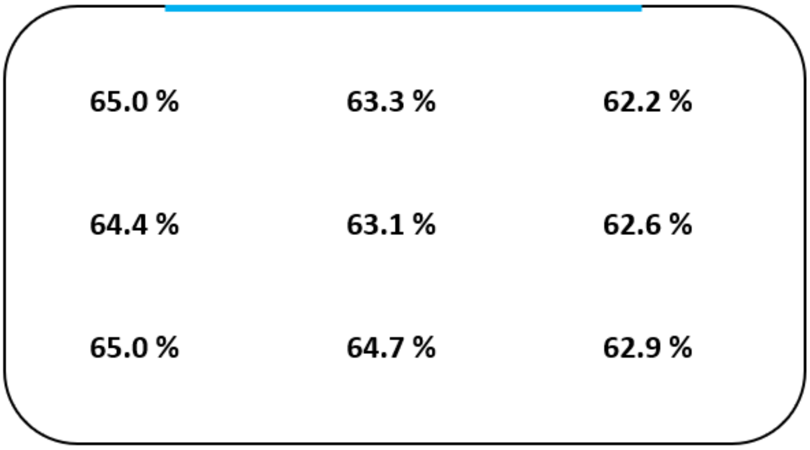

65.0 %	63.3 %	62.2 %
64.4 %	63.1 %	62.6 %
65.0 %	64.7 %	62.9 %

Fig. 4.13: WAXD determined degree of crystallinity of the platelet for C1 with the blue line marking the gate side

Fig. 4.14 displays the mass degree of crystallinity in p8 for all processing conditions. All values are average values of three measurements. As with the results from the SAXS crystallinity, a higher mold temperature leads to a higher amount of crystalline fraction. The injection speed and packing pressure do not have a significant influence on the WAXD crystallinity according to the analysis with Minitab. In Table 4.2, the contribution of each peak to the total crystallinity in p8 for all processing conditions are shown. The (100) lattice planes have the biggest contribution on the degree of crystallinity in POM. Both changes in (100) and (105) are mainly responsible for the total increase of the crystalline fraction.

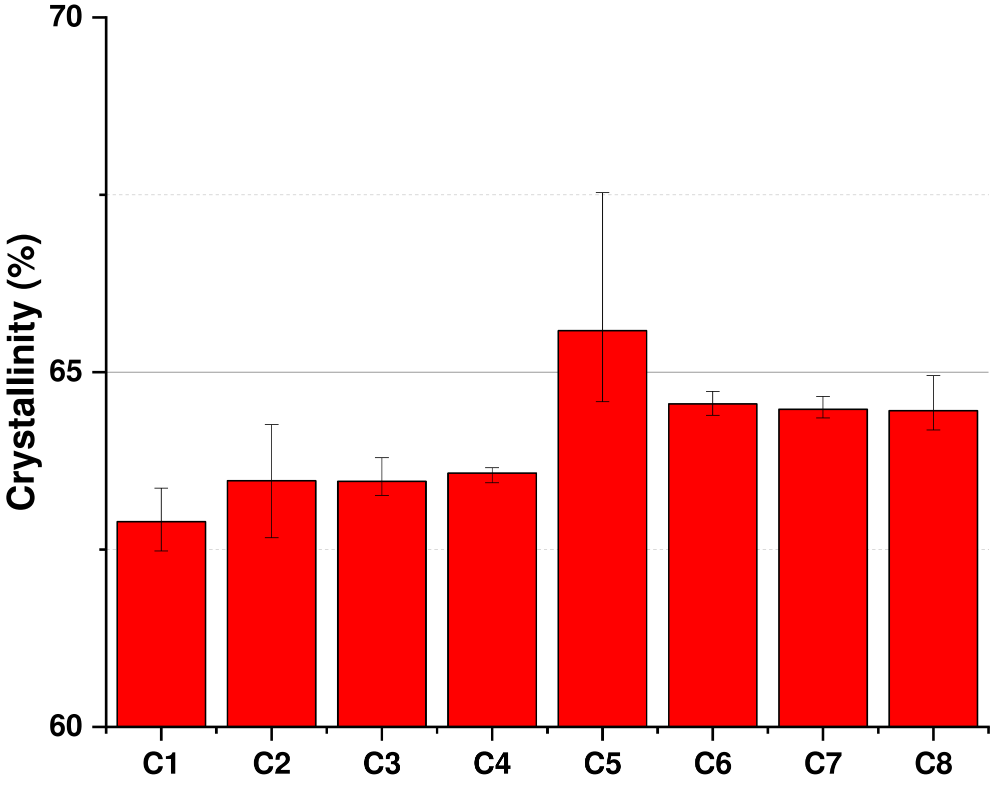

Fig. 4.14: WAXD determined degree of crystallinity in p8 for all processing conditions (error bars: maximum and minimum values)

Table 4.2: Contribution of the single peaks to the crystallinity of p8 for all processing conditions

Specimen	**Crystallinity (%)**	**Δx_{max} (%)** **Δx_{min} (%)**	**(100) (%)**	**(105) (%)**	**(110) (%)**	**(115) (%)**	**(205) (%)**
C1	62.9	+0.47 -0.41	39.9	14.3	0.28	5.28	2.27
C2	63.5	+0.79 -0.80	39.9	14.4	0.28	5.41	2.47
C3	63.5	+0.33 -0.20	41.0	13.7	0.28	5.26	2.37
C4	63.6	+0.08 -0.14	41.2	13.8	0.28	5.23	2.32
C5	65.6	+1.94 -1.00	41.8	15.3	0.27	5.10	2.13
C6	64.6	+0.18 -0.16	40.8	14.6	0.29	5.44	2.40
C7	64.5	+0.18 -0.12	42.2	13.9	0.32	5.16	2.13
C8	64.5	+0.49 -0.27	42.0	14.2	0.31	5.14	2.11

4.1.2 Polarized light microscopy (PLM)

Images obtained using polarized light microscopy allow a qualitative study of spherulite size and distribution and of the typical skin-core structure found in injection molded parts. In the following “t”, “m” and “s” will refer to the positions of the cut (top, middle and side) on the platelets. In Fig. 4.15, the analyzed areas are illustrated for the different cuts. The filling direction for t and m is always from right to left. Fig. 4.16 displays a representative image for Delrin 111PF with the marked layer structure suggested in literature (Liparoti et al., 2016; Liu et al., 2002). Since it is quite sophisticated to determine the exact transition between two adjacent layers, the marks for the different layers must not be taken as absolute, but rather as indication. A nucleation agent in the Delrin resin leads to rather small spherulites which can be observed in the core layer. Due to the small size, a quantitative determination of the spherulite size was not possible.

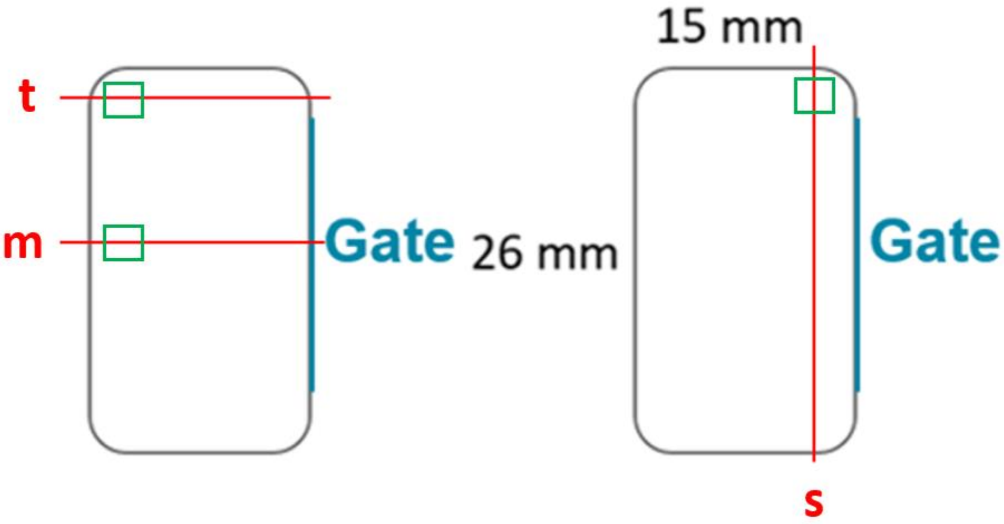

Fig. 4.15: Areas examined for the different cuts (green rectangles)

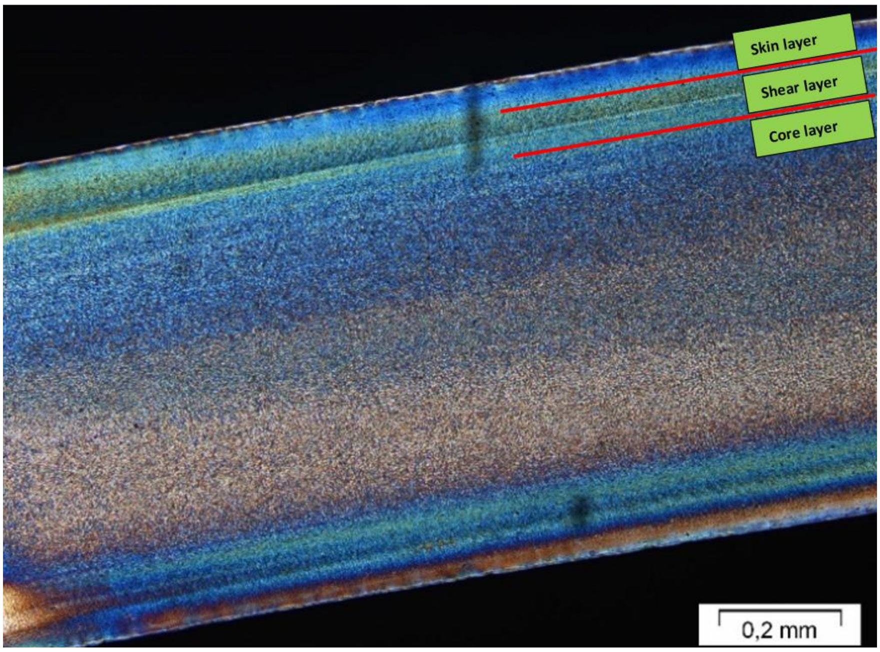

Fig. 4.16: PLM image taken from the t-cut of C1

The influence of the packing pressure, the injection speed and the mold temperature on the cross-section microstructure in flow direction is displayed in Fig. 4.17 (t) and Fig. 4.18 (m). For both cuts it is apparent that a higher mold temperature leads to a thinner skin layer. A higher cooling rate, achieved by a lower mold temperature, gives less time for the crystallization, leading to a thicker skin layer. The expected increase of the spherulite size with a lower cooling rate cannot be observe, because of the small size of the spherulites. As the wall thickness of the platelets is very small (0.8 mm), it is expected that the packing pressure does not have a major influence on the microstructure (especially far from the sprue). This assumption is confirmed by the PLM images, since no significant

C1	**C2 (higher $p_{packing}$)**
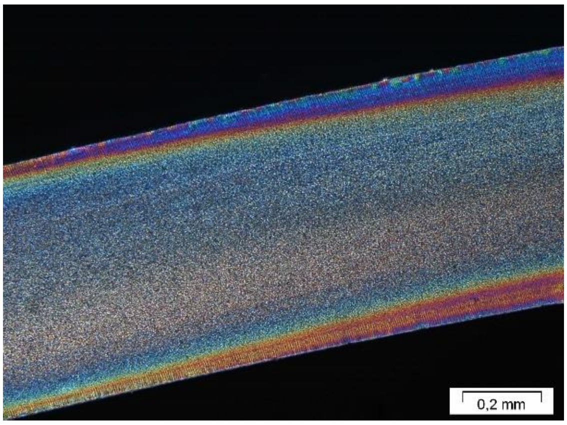	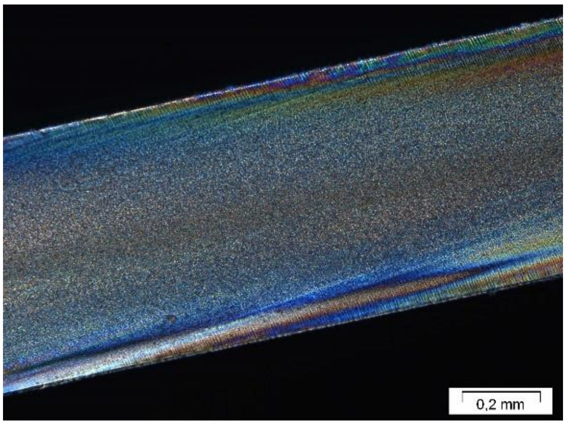
C3 (higher v_{inj})	**C5 (higher T_{mold})**
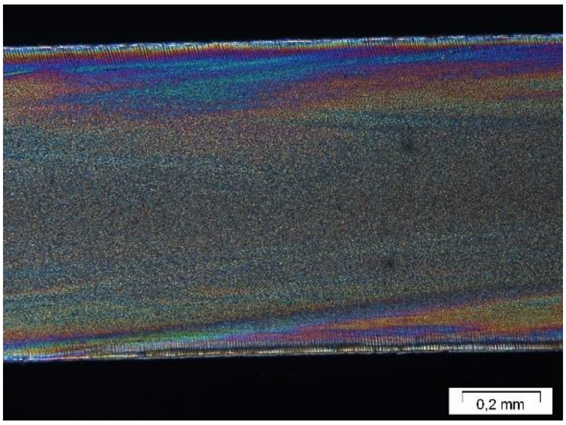	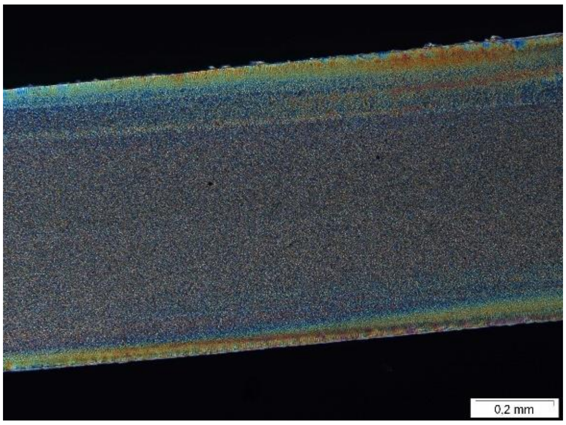

Fig. 4.17: PLM images from the t-cut of the processing conditions C1, C2, C3 and C5 far from the sprue

change between C1 and C2 can be observed. Images closer to the sprue also did not show any significant change in the morphology for a higher packing pressure. Higher injection speeds lead to a higher orientation in the platelets, which is especially visible in the shear layer of both cuts. However, the influence on the orientation of the core layer cannot be deduced from the PLM images. For the m-cut (Fig. 4.18), the influence of the injection speed is more apparent. Here, the thickness of the core layer increases with higher injection speeds, leading to a more pronounced shear layer. Due to higher shear rates, the melt temperature rises with increasing injection speed, resulting in a longer crystallization time. If one compares the pictures of both cuts, one can see that the skin layer is more

C1	**C2 (higher $p_{packing}$)**
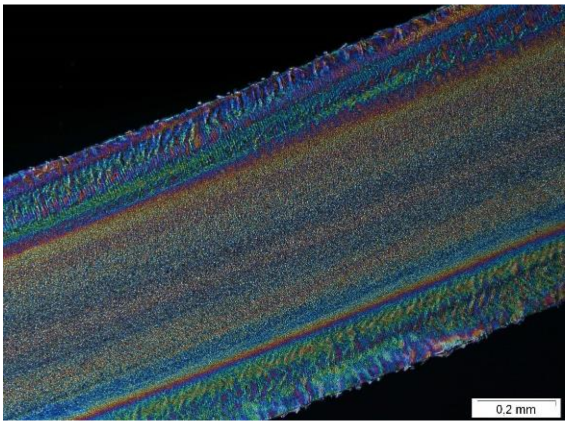	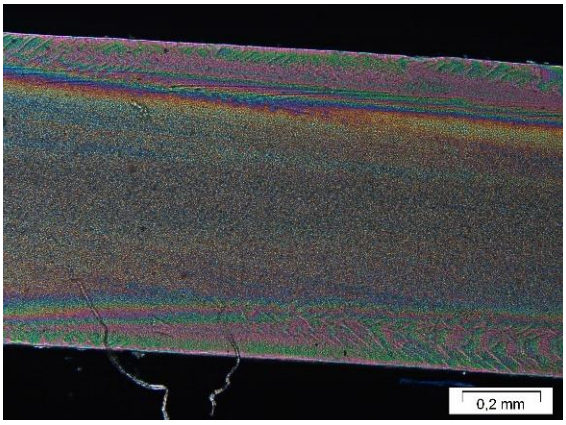
C3 (higher v_{inj})	**C5 (higher T_{mold})**
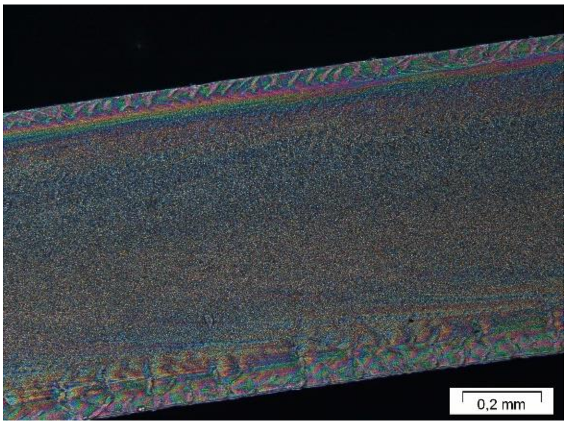	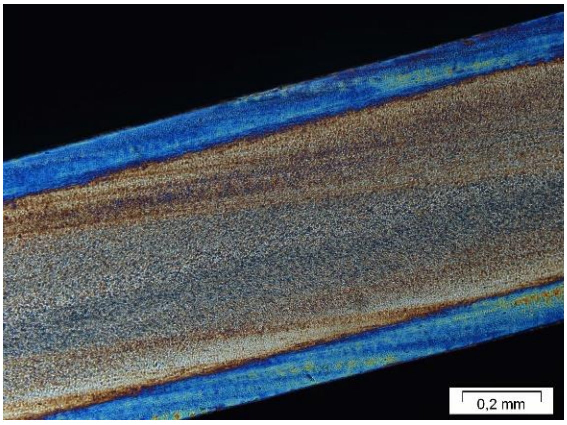

Fig. 4.18: PLM images from the m-cut of the processing conditions C1, C2, C3 and C5 far from the sprue

developed in the m-cut. The different filling behavior in the cuts are expected to be responsible for that occurrence. The ripple in the skin layer, especially in the m-cut, was assumed to be an effect of the sample preparation. However, a recent etching study has indicated that this is rather a morphological characteristic.

Fig. 4.19 illustrates the influence of the three different process parameters on the cross-sectional microstructure perpendicular to the flow direction. Here, the left side of the images is close to the edge of the sample. As with the other cuts, a higher mold temperature leads to a smaller skin layer. Neither the packing pressure nor the injection speed were found to significantly influence the layer structure in this cross-section.

C1	**C2 (higher $p_{packing}$)**
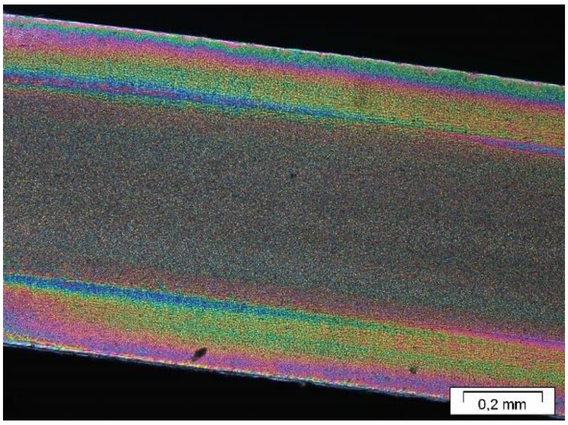	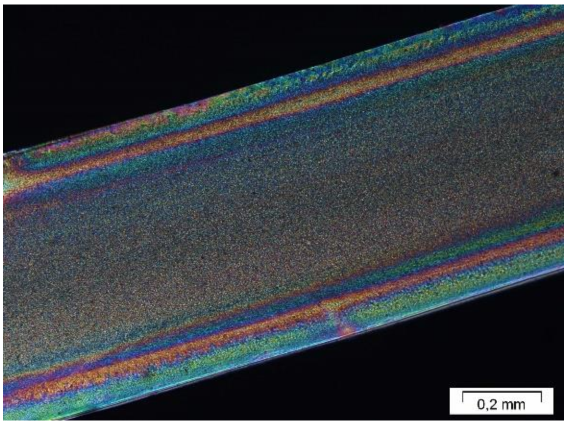
C3 (higher v_{inj})	**C5 (higher T_{mold})**
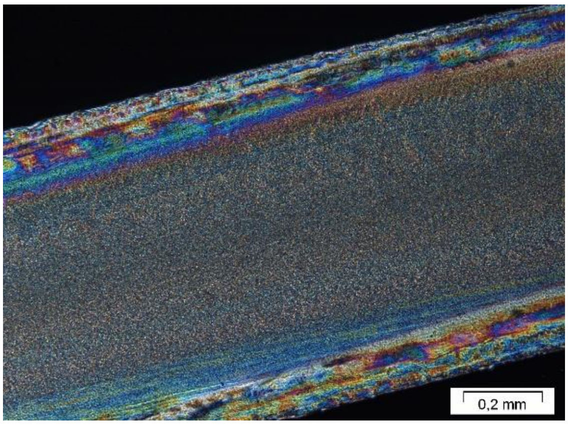	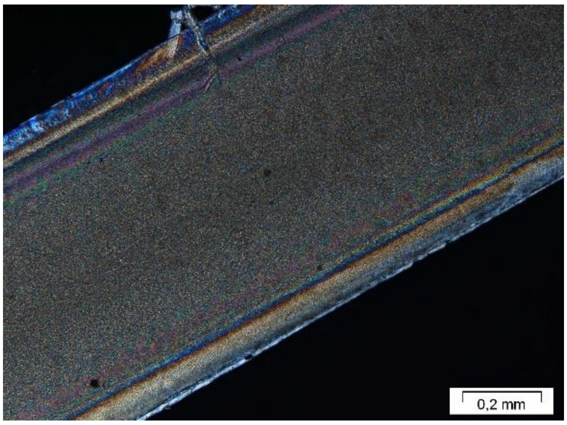

Fig. 4.19: PLM images from the s-cut of the processing conditions C1, C2, C3 and C5 close to the gate

The small black dots and bubbles, which are visible in some pictures, are the result of the specimen preparation (dust particles, trapped air, etc.) and are not attributable to any injection molding effect. Based on the results from this PLM study, it is recommended to include further techniques in the future to get a more detailed information on the microstructure of this POM resin. Especially, the combination of etching and the subsequent surface analysis using Scanning Electron Microscopy is anticipated to give additional information.

4.2 Fracture mechanical characterization

4.2.1 Monotonic fracture tests

Fig. 4.20 displays the critical stress intensity factor (K_C) for all conditions with an initial notch depth of around 1 mm and both testing speeds (10 mm/min and 100 mm/min). All values are average values of four measurements. In comparison to K_{IC} values for SENT specimens found in literature (Bandyopadhyay et al., 1993), the obtained values are lower. However, in a parallel study at the Polymer Competence Center Leoben GmbH, notched tensile bars of the same material were tested. The obtained K_C values were in the same range as the values obtained in this study. Nevertheless, the values can still be compared among themselves. Generally, it is expected that the values for a testing speed of 100 mm/min are lower than for 10 mm/min, but due to the rather big scatter, it is not possible to make a statement regarding the different testing speeds. Furthermore, the values for a testing speed of 100 mm/min were found to be more sensitive to a change in the conditions and their scatter is bigger. Since it was not possible to deduce a clear tendency regarding the influence of the processing settings on K_C, an analysis with Minitab, where the testing speed was implemented as a fourth factor, was carried out. It confirmed that the packing pressure and the testing speed did not have a significant influence on the K_C values of this test series. It was found that a higher mold temperature leads to a more brittle behavior of POM, resulting in a decrease of the K_C. Higher injection speeds lead to higher K_C values for both testing speeds. As an example, the force-displacement curve for the processing condition C1 for a testing speed of 100 mm/min is illustrated in Fig. 4.21.

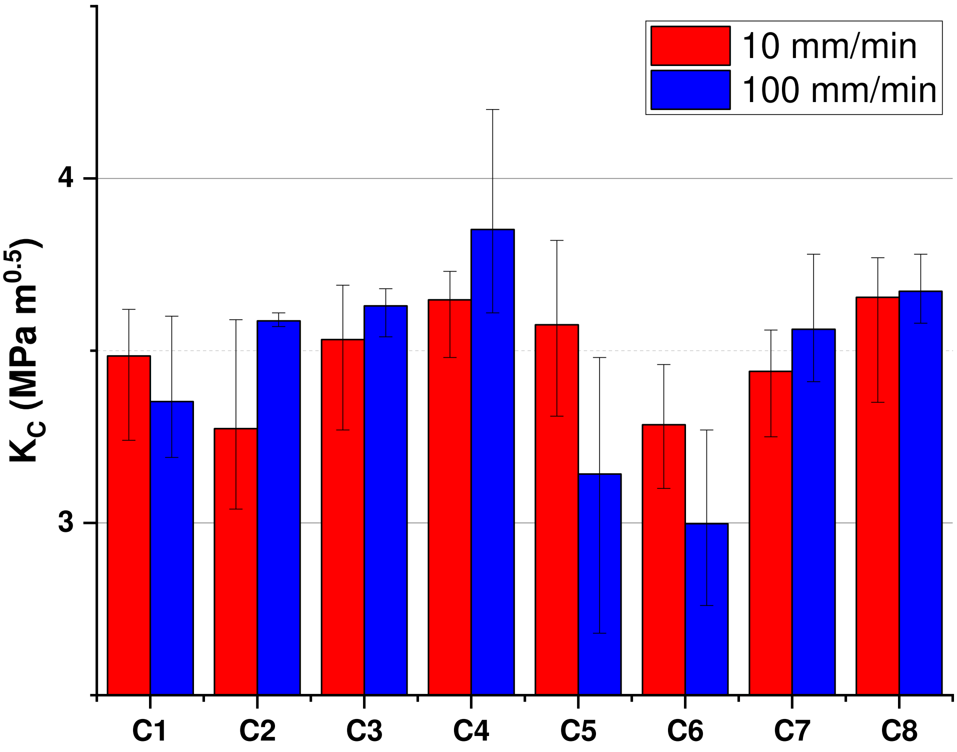

Fig. 4.20: Critical stress intensity factor for all conditions and both testing speeds (10 mm/min and 100 mm/min) (error bars: maximum and minimum values)

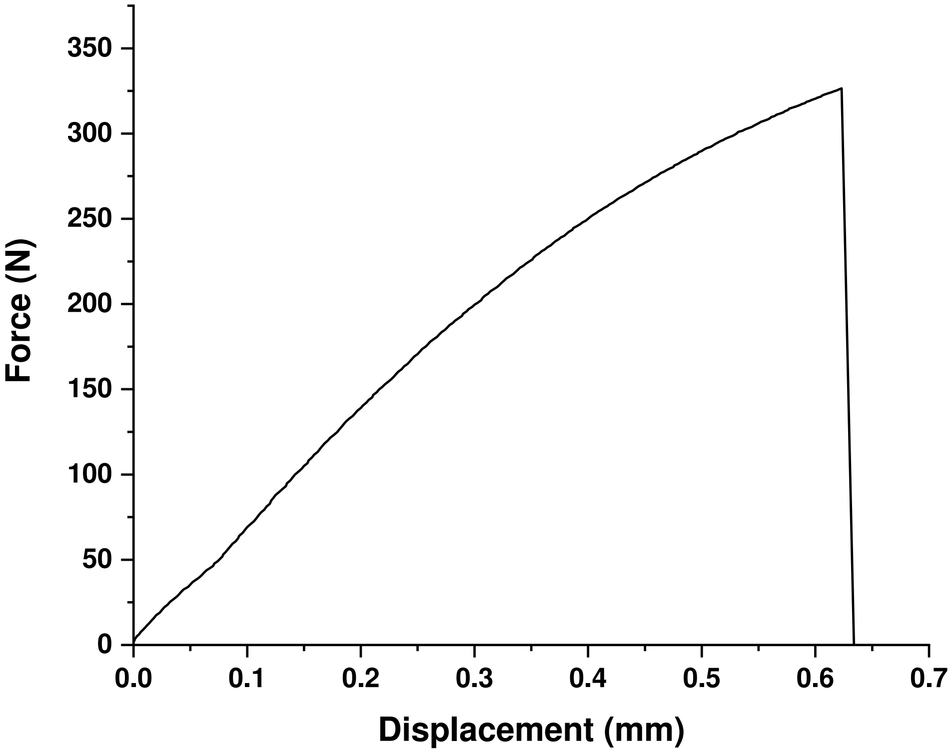

Fig. 4.21: Example of a force-displacement curve for the processing condition C1 for a testing speed of 100 mm/min

In order to verify if the monotonic tests fulfilled the requirements to apply LEFM, tests with different initial crack lengths were carried out. All values (except for a starting crack length of 0.5 mm and a testing speed of 100 mm/min) are average values of four measurements and are displayed in Fig. 4.22. Due to a limited number of test specimens, only one successful test on the specimen with an initial crack length of 0.5 mm with a testing speed of 100 mm/min was carried out. The results clearly show that the K_C values obtained with the µ-SENT specimens are dependent on the initial crack length and thus the results obtained with the previous tests did not yield any material parameters. Nevertheless, although the requirements for the linear elastic fracture mechanics are not fulfilled, the µ-SENT specimens are still advantageous for the comparison of the different processing conditions. Moreover, only this small plate geometry allowed the suitable investigation of the rather harsh processing conditions used in this study.

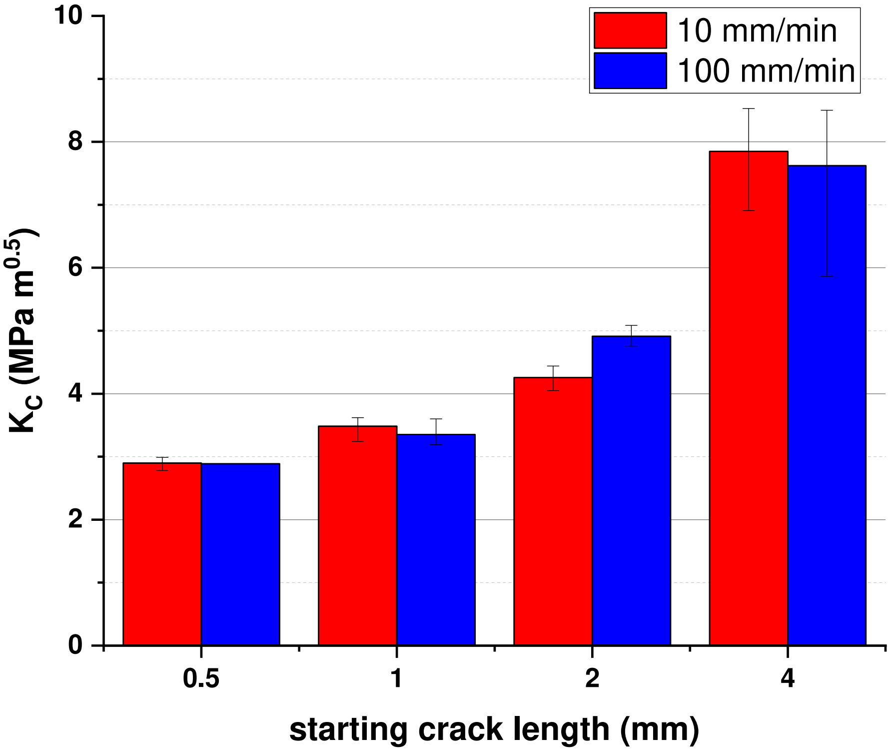

Fig. 4.22: Critical stress intensity factor for C1 with different starting crack lengths and two different testing speeds (10 mm/min and 100 mm/min) (error bars: maximum and minimum values)

4.2.2 Fatigue fracture tests

Each point in the figures in this chapter represents a single measurement. The plots will be referred to as "fatigue fracture curves". For a better overview, the results of the fatigue fracture tests for lower (C1-C4) and higher (C5-C8) mold temperatures are displayed in Fig. 4.23 and Fig. 4.24. The implemented lines are trend lines with the intend to support the qualitative ranking rather than show quantitative trends. In the regions, where the requirements for LEFM are not fulfilled, a polynomial fit of the second order was used. The half-filled points indicate the specimens, which broke within the low cycle fatigue area. At a ΔK-level of around 2 MPa $m^{0.5}$, the ductile-brittle transition is located.

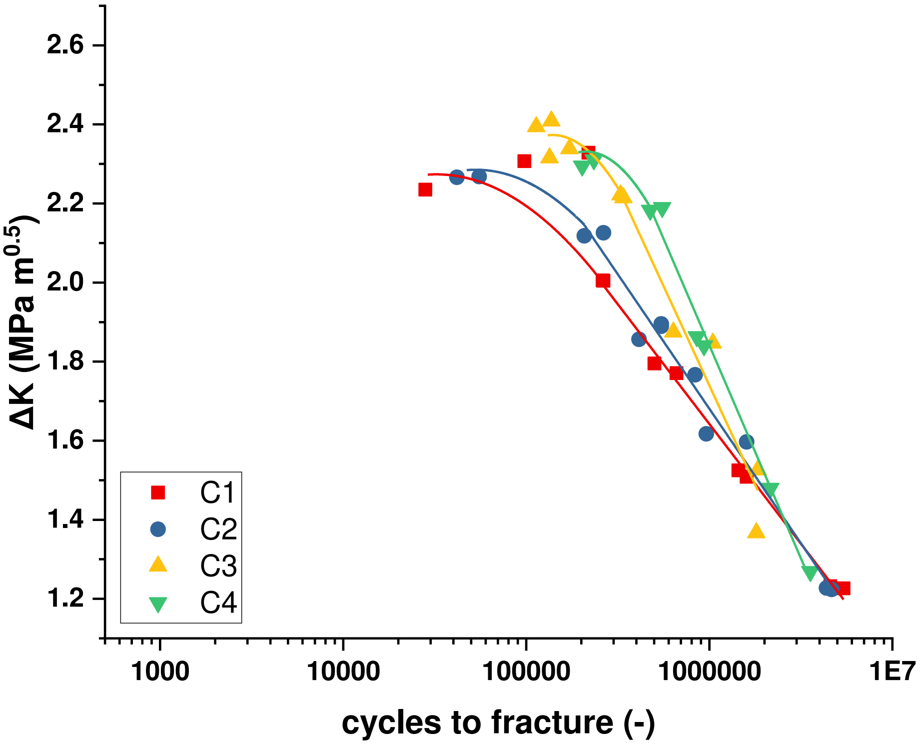

Fig. 4.23: Fatigue fracture curves for the processing conditions C1-C4

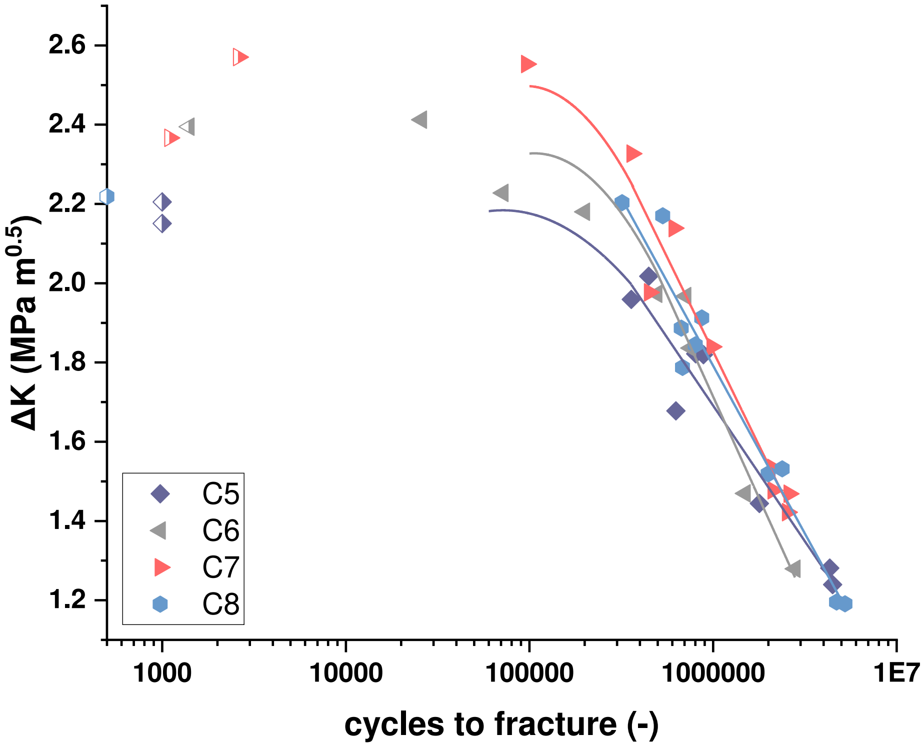

Fig. 4.24: Fatigue fracture curves for the processing conditions C5-C8

To better display the influence of the different process parameters on the fatigue fracture behavior of POM, only a section (beginning with a cycle count of 4x10^4) of the graph will be shown. Fig. 4.25 illustrates the influence of the mold temperature on the fatigue fracture curves for two different injection speeds. Other curves (C2 and C6 as well as C4 and C8) showed a similar behavior as the C1 and C5 curves regarding the influence of the mold temperature. Here, a small shift to higher number of cycles to fracture at high load levels occurs. Only at a high injection speed and a low packing pressure (C3 and C7), a higher mold temperature seems to shift the whole fatigue curve to a slightly higher number of cycles to fracture.

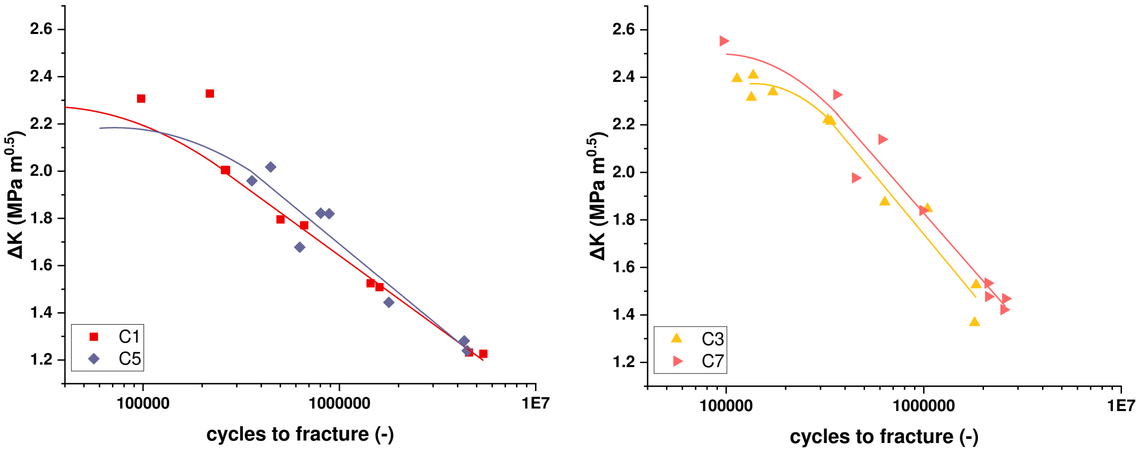

Fig. 4.25: Fatigue fracture curves for C1 and C5 (left) as well as C3 and C7 (right)

The influence of the injection speed on the fatigue fracture behavior is illustrated in Fig. 4.26. At high load levels, a stronger discrepancy between the curves is present. With a higher injection speed, the curve gets shifted to a higher number of cycles to fracture, leading to an improved fatigue behavior in these regions. The slope of the curves is steeper for the conditions processed with higher injection speeds. This leads to a similar number of cycles to fracture at low load values. If one extrapolates the trend lines to even lower load levels, the conditions with a lower injection speed may have a better fatigue behavior. This shows that the injection speed improves the fatigue fracture behavior in the region examined, but it does not guarantee an improvement of the whole fatigue fracture behavior, especially in the region, where the long-term behavior dominates.

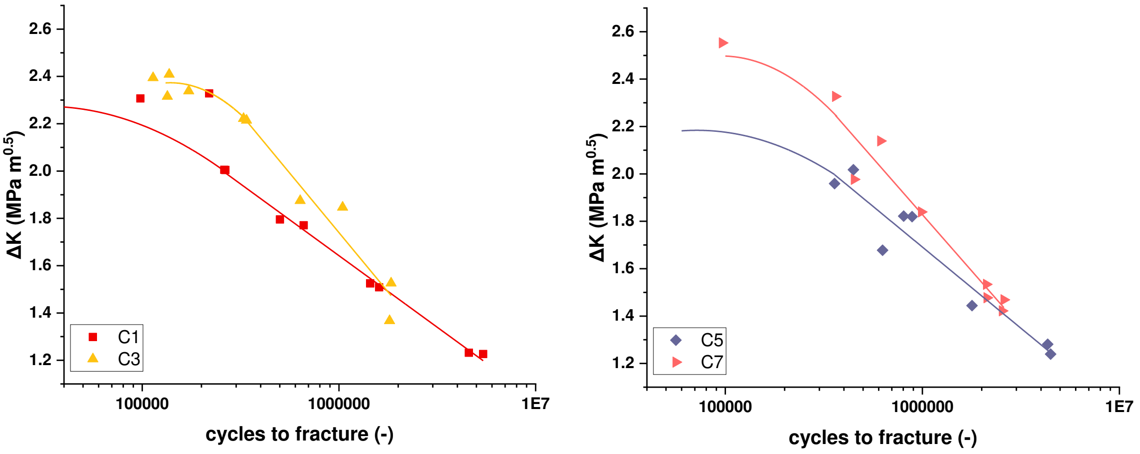

Fig. 4.26: Fatigue fracture curves for C1 and C3 (left) as well as C5 and C7 (right)

In Fig. 4.27, the influence of the packing pressure at two different mold temperatures is shown. A higher packing pressure leads to a small shift to higher number of cycles to fracture at high load levels. The other conditions processed with a lower mold temperature (C3 and C4) showed a similar behavior like C1 and C2. At a higher mold temperature, a higher packing pressure leads to a steeper slope of the curve, resulting in an inferior fatigue fracture behavior at low load levels. C7 and C8 (high mold temperature) did not show a significant influence of the packing pressure. This indicates no further improvement in packing behavior and the formation of a plateau in fracture mechanical behavior with higher packing pressure at elevated mold temperature and injection speed.

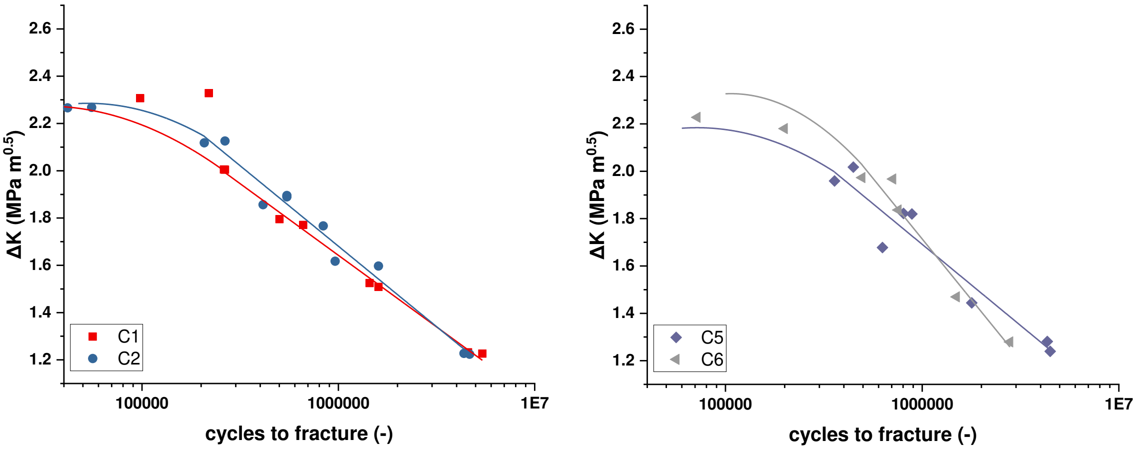

Fig. 4.27: Fatigue fracture curves for C1 and C2 (left) as well as C5 and C6 (right)

4.3 Correlation between morphology and fracture mechanical behavior

The nucleating agent in the resin examined leads to a very small size of the spherulites, so small that they could not be quantified with PLM. Nevertheless, they were found to be very evenly distributed in the core layer. This uniform composition reduces the risk of having defects that could potentially reduce the material’s performance. For this resin, a higher density of tie molecules (TM) and entanglements is expected due to its high molecular weight, the small spherulites and lamellae (compared to (Berer et al., 2018)), resulting in an improved crack growth resistance. On the other hand, the crystallinity is rather high, which usually reduces the TM and entanglement density.

Specimens produced with a higher mold temperature showed a higher degree of crystallinity and a higher lamellar thickness as well as a lower fracture toughness. One would expect an increase in the fracture toughness with a higher crystallinity since more energy would be required to deform a unit volume of material. The increase (around 2%) of the crystalline fraction is expected to be too small to have a significant influence on the fracture mechanical behavior. (Plummer et al., 1995) reported higher K_{IC} values with increasing entanglement density. A higher density of entanglements can be achieved by a lower mold temperature (higher cooling rate). This is interpreted to be the reason for the higher values of K_C at lower mold temperatures. Contrary to that, a higher mold temperature resulted in a small improvement of the fatigue fracture behavior at higher load levels. Nevertheless, the differences are very small. It is speculated if this is the influence of experimental scatter.

A higher injection speed led to more oriented crystals along the fracture mechanical loading direction and a higher orientation in the shear layer as well as a higher K_C and a better fatigue behavior. Since the injection speed did not have any effect on the total crystallinity, it is expected that the fracture mechanical behavior of the specimens is mostly influenced by the orientation state in the specimens. At high load levels, a higher oriented state led to a shift of the fatigue fracture curve to a higher number of cycles to fracture, resulting in an improved material behavior. Only at low load levels, the orientation state did not have a significant influence on the fatigue fracture behavior.

The packing pressure did not show a significant influence on the analyzed morphological parameters and the K_C. As with the mold temperature, an increase of the packing pressure led to a small shift of the fracture curve to higher cycles to fracture at higher loads. At a higher mold temperature, a higher packing pressure led to a steeper slope of the fracture curve, resulting in a worse fatigue fracture behavior at low load levels.

4.4 Simulation results

The filling of the platelet obtained from the 3D simulation is illustrated in Fig. 4.28 for C1. To ensure a simultaneous propagation of the flow front in the mold, a film gate was used. It is apparent that the film gate did not have the desired effect, since the flow front in the middle runs ahead of the flow front on both sides, resulting in a pronounced fountain flow during filling of the mold. Through the elongational flow, the molecules are stretched and oriented perpendicular to the main flow direction. The lamellae then grow from these molecules, resulting in an orientation more in the main flow direction. This explains the orientation of the lamellae from the SAXS measurements on the sides of the platelet. The orientation of the molecules in the middle of the platelet is dominated by the shear flow, resulting in a lamellae orientation perpendicular to the main flow direction.

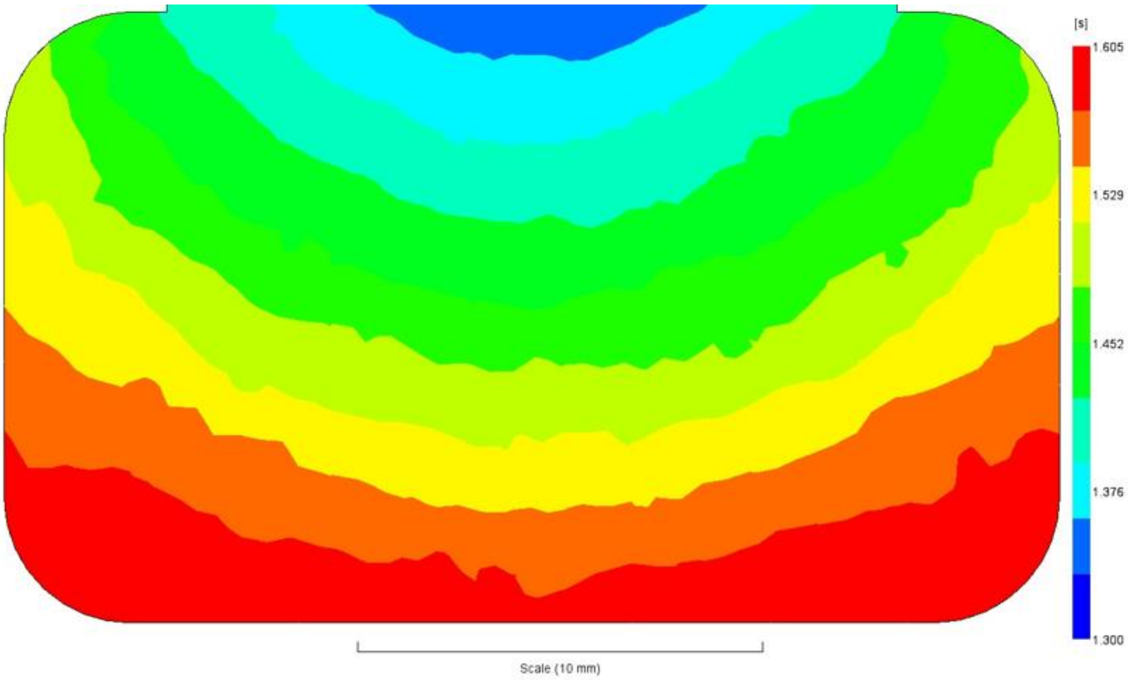

Fig. 4.28: Mold flow simulated filling of the platelet for C1 (the legend represents the filling time including the pre-filling of the runner system)

The simulations of C5 and C6 did not show a different filling behavior compared to the other conditions. This is contrary to the results obtained from the X-ray measurements. Hence, a different filling behavior was expected. Nevertheless, it is assumed that the filling behavior of these two conditions is different since real specimens were analyzed with X-ray measurements and every single measurement of such showed the same trend. It could be speculated that this difference is attributed to the different filling times in combination with the high mold temperature, which allows for significant relaxation of oriented molecules. However, this is contradicted by Table 4.3, in which the filling time for each processing condition is displayed.

Table 4.3: Filling time of all processing conditions (obtained from the 3D simulations)

Processing condition	**Filling time (s)**	**Processing condition**	**Filling time (s)**
C1	1.61	*C5*	1.58
C2	1.60	*C6*	1.58
C3	0.13	*C7*	0.13
C4	0.13	*C8*	0.13

Fig. 4.29 and Fig. 4.30 display the influence of the different process settings on the spherulite size in the middle layer obtained from the 2.5D simulations. The simulations confirm a rise of the spherulite size with increasing mold temperature. A higher injection speed leads to a more uniform distribution of the spherulites in the platelet. Results obtained from the X-ray measurements showed a pretty uniform distribution of the crystallinity over the whole platelet. It has to be kept in mind that the results obtained from the X-ray measurements detect all crystalline fractions and display average values over the whole thickness, while the simulation results show only the spherulite size distribution in the middle layer. The other layers showed the same behavior regarding the influence of the different processing settings and showed a lower spherulite size in the outer layers.

C1
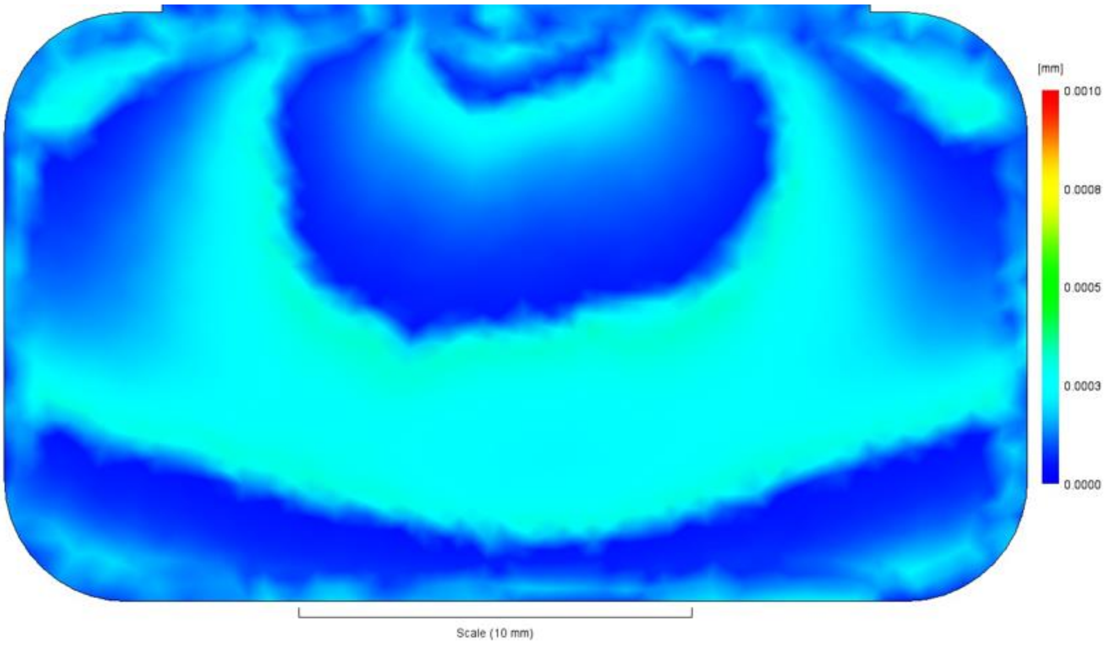
C2 (higher $p_{packing}$)
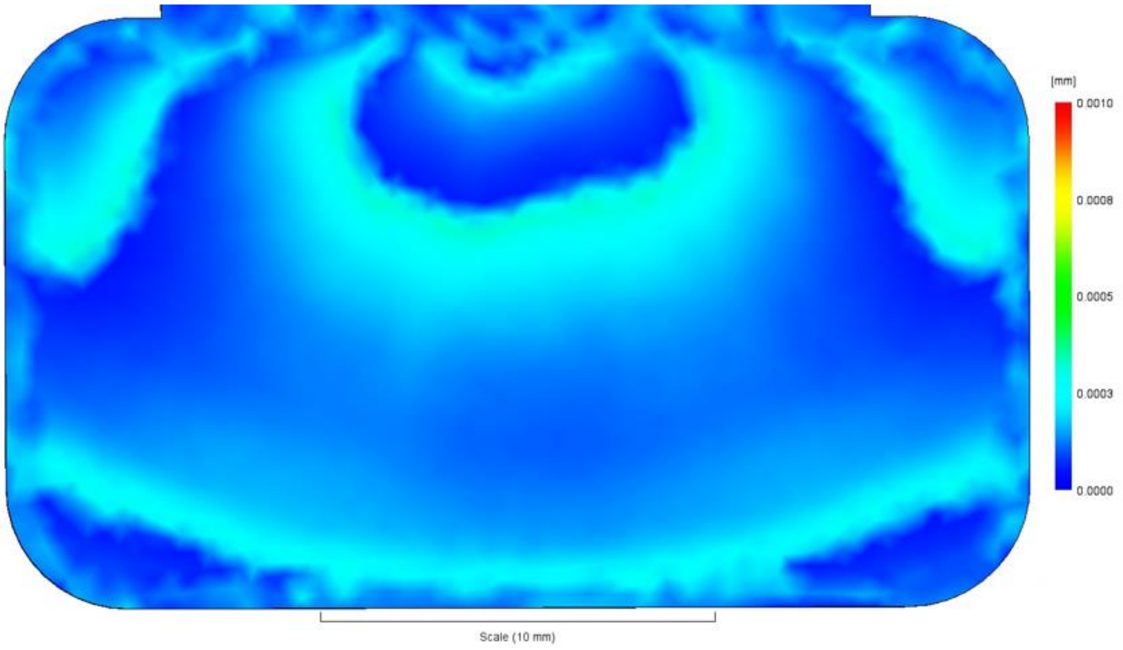

Fig. 4.29: Crystal size over the platelet in the middle layer for C1 and C2 (obtained from the 2.5D simulations)

C3 (higher v_{inj})

C5 (higher T_{mold})

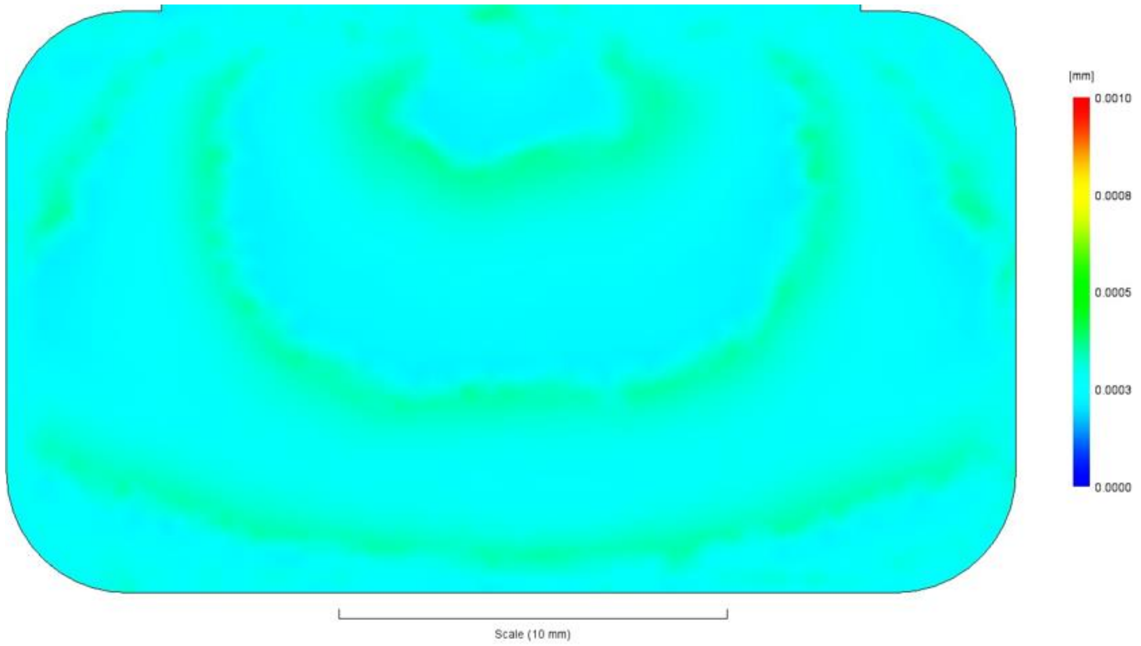

Fig. 4.30: Crystal size over the platelet in the middle layer for C3 and C5 (obtained from the 2.5D simulations)

In Fig. 4.31, the spherulite size over the normalized thickness near the position p8 from the X-ray measurements is displayed. A value of 0 for the normalized thickness corresponds to the layer in the middle of the platelet, 1 and -1 are the values at the top and bottom surface. Here, it is apparent that a higher mold temperature leads to bigger spherulites in each layer and therefore, a higher degree of crystallinity is assumed. This also fits to the crystallinity values determined by WAXD, which were shown in Fig. 4.14. For every condition, the smallest spherulite dimensions are found in the most outer layer, where there is little time for the crystals to grow, since the material gets frozen almost instantly at the mold wall. Interestingly, the size of the spherulites inFig. 4.31 is in the order of the wavelength of the visible light, except for the outermost layers produced with the low mold temperature (C1, C2, C3 and C4), where it is clearly below. Hence, it is speculated that these outermost layers are transparent to visible light, while core and the outermost layers of the specimens produced with high mold temperature are not. For the further research, it is recommended to conduct coresponding experiments for microtome cuts in the light microscope. The results can be used to judge and in the best case to confirm the simulation results presented in this work.

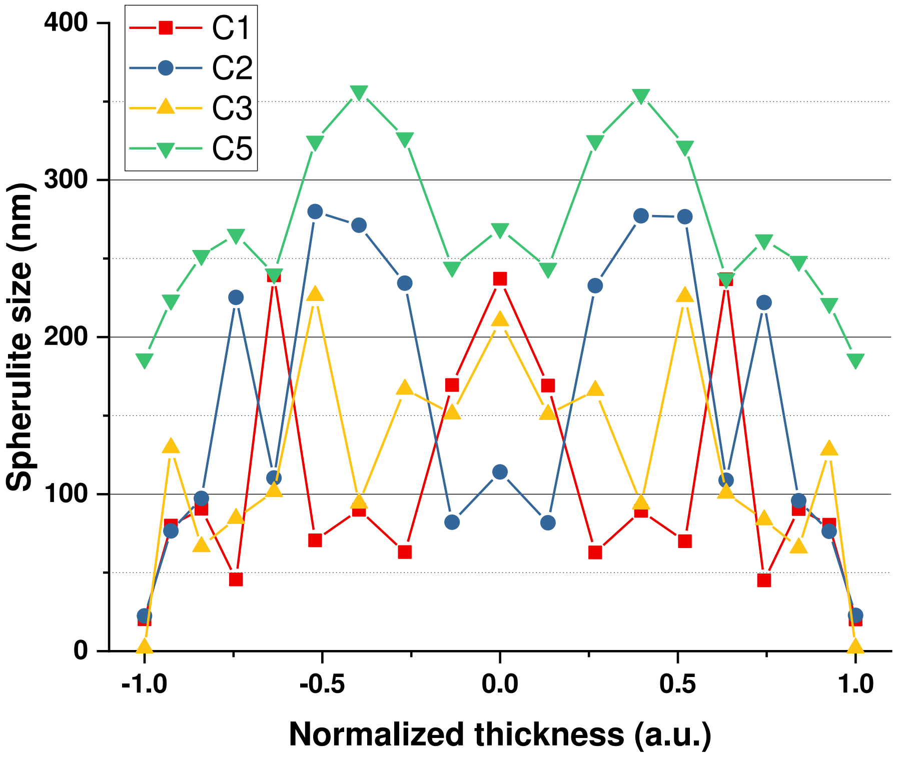

Fig. 4.31: Spherulite size at the position p8 over the normalized thickness for C1, C2, C3 and C5 (obtained from the 2.5D simulations)

Fig. 4.32 illustrates the crystalline orientation factor over the normalized thickness near the position p8 for the four conditions examined above (C1, C2, C3 and C5). It gives the orientation of the crystals in regard to an axis of interest and varies from 1 (parallel to the axis) to -0.5 (perpendicular to the axis). In MoldFlow, the axis of interest is the flow direction. The values of 0 at both outer sides of the platelet are due to the quick freezing of the material at the mold wall. Platelets produced with a higher mold temperature favor a more unoriented state of the crystals over the whole thickness. Due to high shear forces close to the most outer layer, a high orientation in flow direction of the crystals is present in this zone. The values of the Herman's orientation function obtained from the X-ray measurements cannot be directly compared to these values since the X-ray measurements only considered the orientation of one specific plane as well as give an average value over the whole thickness of the platelet. However, the results from the X-ray measurements suggested a second orientation direction at lower mold temperatures (Fig. 4.12), which is contrary to the results obtained from the simulations. In order to better compare the crystalline orientation factor to the results obtained from the X-ray measurements, it was averaged over the whole thickness. This did not yield any sufficient results.

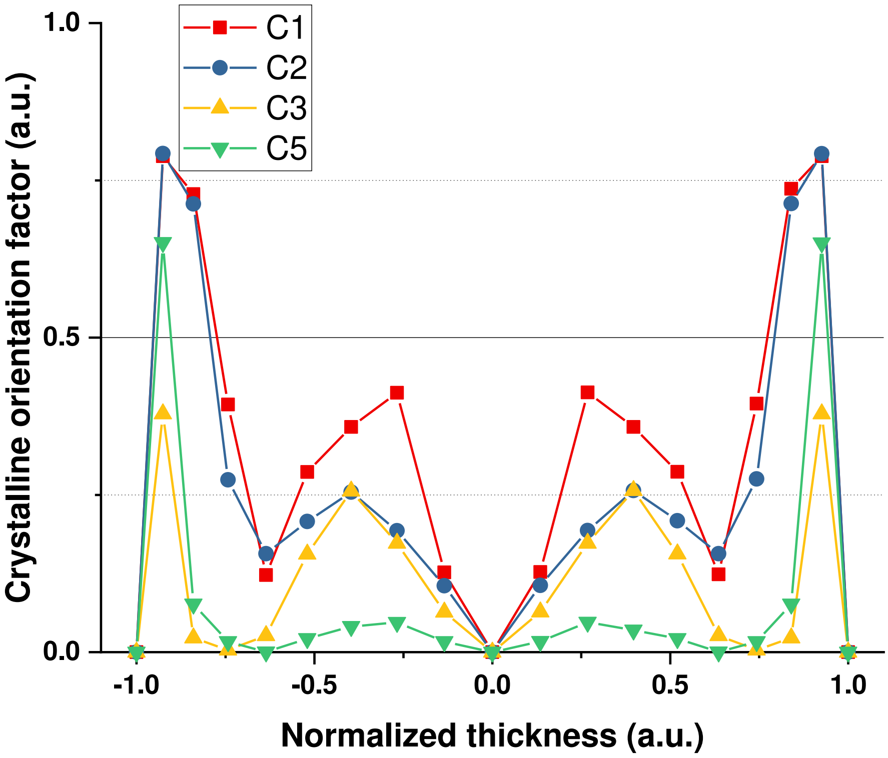

Fig. 4.32: Crystalline orientation factor at the position p8 over the normalized thickness for C1, C2, C3 and C5 (obtained from the 2.5D simulations)

5 SUMMARY, CONCLUSIONS & OUTLOOK

POM is a semi-crystalline thermoplastic with a high degree of crystallinity. It is used in a wide range of industry fields (e.g. mechanical engineering or automotive) and is often processed by injection molding. This process has a big influence on the morphology of a polymeric material and thus, determines the properties of the finished part. In order to guarantee the desired properties of the processed parts, it is crucial to know the link between the processing parameters and the morphology as well as between the morphology and the properties of the finished part. For that purpose, small platelets were produced by injection molding following a design of experiment (DOE). Within the DOE, the mold temperature, the injection speed and the packing pressure were varied. To assess the morphological state, X-ray measurements consisting of small-angle X-ray scattering (SAXS) and wide-angle X-ray diffraction (WAXD) as well as an analysis with a polarized light microscope were carried out. Monotonic fracture tests and fatigue fracture tests were used to determine the fracture mechanical properties of the platelets. Since simulations take a very important part in the industry nowadays, filling simulations were carried out in MoldFlow. MoldFlow allowed to simulate the crystallization and morphological changes during processing by implementing crystallization parameters of POM. These results were then compared to the results obtained from the morphological analysis.

The X-ray measurements consisted of a scan over the whole platelet as well as additional scans for the area close to the notch for the fracture mechanical tests. SAXS and WAXD tests allowed to determine the orientation state of the lamellae and the crystals in the tested platelets. With the distance to the gate, the orientation decreased and a second orientation direction formed. Samples produced with a higher mold temperature showed a higher degree of crystallinity. In general, the increase of the crystalline fraction for the investigated resin was rather small. An increase of the injection speed mainly had an influence on the orientation state in the samples and did not affect the total crystallinity at all. The packing pressure did not show any significant influence on the morphology of the tested specimens. It is suspected that the platelets froze too quickly for the packing pressure to have a significant influence.

For the tests with the polarized light microscope, three different cross-sections (two in flow direction and one perpendicular to the flow direction) were analyzed. A uniform distribution of the very small spherulites in the core layer was identified, but the resolution was not high enough to accurately determine the size of them. Furthermore, it was difficult to precisely determine the transition from core to shear layer and from shear to skin layer. Hence, further investigations are recommended. Various methods such as etching in combination with Scanning Electron Microscopy have the potential to provide more detailed information.

So-called “µ-SENT”-specimens, which were cut out from the injection molded platelets, were used in the monotonic and fatigue fracture mechanical tests. The fracture toughness (K_C) decreased with increasing mold temperature, while the fatigue fracture behavior showed a small improvement at higher loads. An increase of the injection speed led to an increase of K_C and improved the fatigue fracture behavior up to a number of cycles to fracture of around 10^7. The packing pressure only led a minor improvement of the fatigue fracture behavior at high load levels.

The filling simulations gave information about the size-distribution of the spherulites over the thickness of the plate. As expected, the smallest spherulites were found in the skin layer and specimens produced with a higher mold temperature showed bigger spherulites over the whole thickness. Furthermore, the orientation factor of the crystalline fraction was studied. Unfortunately, it was not possible to directly compare them to the results obtained from the X-ray measurements due to several factors: the X-ray measurements only considered one crystalline plane, not the whole crystal and only provided an average value over the whole thickness. Averaging the results obtained from the simulations over the whole thickness did not provide plausible and comparable results.

To sum it up, the most influential parameter on the fracture mechanical behavior was the injection speed. The monotonic fracture toughness as well as the fatigue behavior were improved, while, regarding the morphology, only a different orientation state in the sample occurred. A higher mold temperature lead to a higher degree of crystallinity while K_C decreased. The packing pressure did not influence the morphology or the fracture mechanical behavior significantly. This leads to the conclusion that the orientation of the lamellae and crystals is most influential on an improved fracture mechanical behavior for the resin studied in this thesis.

Finally, some critical comments on the techniques and analysis methods used in this study are given. Regarding WAXD analysis, the Herman’s orientation function alone was not suitable for a quantitative assessment of the orientations since it gave the same value for a completely unoriented state or for two main orientation directions perpendicular to each other. It is expected that aligning the axis of interest parallel to one main orientation direction provides a solution to this problem. Regarding the SAXS analysis, for improved information about the morphological state, it is recommended to partially integrate the SAXS patterns and to evaluate the long period in the different orientation directions. To eliminate the limitations of PLM, the examination of the samples with etching in combination with Scanning Electron Microscopy is suggested to get more information about the morphological state. Regarding the industrial near processing conditions that were aimed at in this thesis, it was necessary to use these thin platelets. Although, they were not optimum for fracture mechanical tests, they still gave plausible results. Regarding MoldFlow, it is to question how accurately the crystallization in the mold is displayed. Furthermore, it is unknown how the crystalline orientation factor is calculated and if it has the same weakness as the Herman’s orientation function used for the WAXD analysis. The simulated residual stresses did not give plausible results. Hence, additional research is needed on this topic.

6 REFERENCES

Alexander, L. (1969): X-ray diffraction methods in polymer science. New York: Wiley-Interscience (Wiley series on the science and technology of materials).

Anderson, T. (2005): Fracture Mechanics. Fundamentals and Applications, Third Edition. 3rd ed. Hoboken: CRC Press. avilable online at http://gbv.eblib.com/patron/FullRecord.aspx?p=1449389.

Arbeiter, F.; Schrittesser, B.; Frank, A.; Berer, M.; Pinter, G. (2015): Cyclic tests on cracked round bars as a quick tool to assess the long term behaviour of thermoplastics and elastomers. In: *Polymer Testing* 45, S. 83–92. DOI: 10.1016/j.polymertesting.2015.05.008.

ASTM E 399 - 19: Test Method for Linear-Elastic Plane-Strain Fracture Toughness KIc of Metallic Materials. DOI: 10.1520/E0399-19.

ASTM E 0647-15: Test Method for Measurement of Fatigue Crack Growth Rates. DOI: 10.1520/E0647-15E01.

Bandyopadhyay, S.; Roseblade, J.; Muscat, R. (1993): Fracture study of a polyacetal resin. In: *J Mater Sci* 28 (14), S. 3777–3782. DOI: 10.1007/BF00353178.

Berer, M.; Halb, M.; Feuchter, M.; Pacher, G.; Pinter, G. (2018): Fatigue Fracture Properties and Morphology of Polyoxymethylene (POM) Plates Produced under Moderate Processing Conditions. In: *International Journal of Polymer Science* 2018, S. 1–18. DOI: 10.1155/2018/7410925.

Berer, M.; Major, Z. (2010): Characterization of the global deformation behaviour of engineering plastics rolls. In: *Int J Mech Mater Des* 6 (1), S. 1–9. DOI: 10.1007/s10999-010-9111-9.

Berer, M.; Major, Z. (2012): Characterisation of the Local Deformation Behaviour of Engineering Plastics Rolls. In: *Strain* 48 (3), S. 225–234. DOI: 10.1111/j.1475-1305.2011.00816.x.

Berer, M.; Pinter, G.; Feuchter, M. (2014): Fracture mechanical analysis of two commercial polyoxymethylene homopolymer resins. In: *J. Appl. Polym. Sci.* 131 (19). DOI: 10.1002/app.40831.

Berer, M.; Tscharnuter, D.; Pinter, G. (2015): Dynamic mechanical response of polyetheretherketone (PEEK) exposed to cyclic loads in the high stress tensile regime. In: *International Journal of Fatigue* 80, S. 397–405. DOI: 10.1016/j.ijfatigue.2015.06.026.

Bragg, W.; Bragg, W. (1913): The Reflection of X-rays by Crystals. In: *Proceedings of the Royal Society A: Mathematical, Physical and Engineering Sciences* 88 (605), S. 428–438. DOI: 10.1098/rspa.1913.0040.

Crist, B.; Schultz, J. (2016): Polymer spherulites: A critical review. In: *Progress in Polymer Science* 56, S. 1–63. DOI: 10.1016/j.progpolymsci.2015.11.006.

Domininghaus, H.; Elsner, P.; Eyerer, P.; Hirth, T. (2012): Kunststoffe. Berlin, Heidelberg: Springer Berlin Heidelberg.

Ewald, P. (1921): VII. Das „reziproke Gitter“ in der Strukturtheorie. In: *Zeitschrift für Kristallographie - Crystalline Materials* 56 (1-6). DOI: 10.1524/zkri.1921.56.1.129.

Gedde, U. (2013): Polymer Physics. Dordrecht: Springer Netherlands.

Geil, P. (1967): Morphology of Polyoxymethylene. In: *Journal of Macromolecular Science: Part A - Chemistry* 1 (2), S. 325–337. DOI: 10.1080/10601326708053974.

Gerasimov, V.; Genin, Y.; Tsvankin, D. (1974): Small-angle x-ray study of deformed bulk polyethylene. In: *J. Polym. Sci. Polym. Phys. Ed.* 12 (10), S. 2035–2046. DOI: 10.1002/pol.1974.180121006.

Grellmann, W.; Seidler, S. (2011): Kunststoffprüfung. München: Carl Hanser Verlag GmbH & Co. KG.

Guinier, A. (2013): X-Ray Diffraction. In Crystals, Imperfect Crystals, and Amorphous Bodies. Newburyport: Dover Publications (Dover Books on Physics). avilable online at http://gbv.eblib.com/patron/FullRecord.aspx?p=1900960.

Halb, M. (2016): Influence of the Processing Conditions on Morphology and Fracture Mechanical Properties of unfilled Polyoxymethylene (POM). Diploma Thesis. Montanuniversitaet Leoben, Austria. Materials Science and Testing of Plastics.

Hama, H.; Tashiro, K. (2003a): Structural changes in non-isothermal crystallization process of melt-cooled polyoxymethylene. [I] Detection of infrared bands characteristic of folded and extended chain crystal morphologies and extraction of a lamellar stacking model. In: *Polymer* 44 (10), S. 3107–3116. DOI: 10.1016/S0032-3861(03)00207-6.

Hama, H.; Tashiro, K. (2003b): Structural changes in non-isothermal crystallization process of melt-cooled polyoxymethylene[II] evolution of lamellar stacking structure derived from SAXS and WAXS data analysis. In: *Polymer* 44 (7), S. 2159–2168. DOI: 10.1016/S0032-3861(03)00093-4.

Hammersley, A. (2016): FIT2D: a multi-purpose data reduction, analysis and visualization program. In: *J Appl Crystallogr* 49 (2), S. 646–652. DOI: 10.1107/S1600576716000455.

Hashemi, S.; Williams, J. (1984): Size and loading mode effects in fracture toughness testing of polymers. In: *J Mater Sci* 19 (11), S. 3746–3759. DOI: 10.1007/PL00020112.

Hertzberg, R.; Manson, J. (1980): Fatigue of engineering plastics. New York, NY: Acad. Press.

Hirose, R.; Yoshioka, T.; Yamamoto, H.; Reddy, K.; Tahara, D.; Hamada, K.; Tashiro, K. (2014): In-house simultaneous collection of small-angle X-ray scattering, wide-angle X-ray diffraction and Raman scattering data from polymeric materials. In: *J Appl Crystallogr* 47 (3), S. 922–930. DOI: 10.1107/S1600576714006724.

Iguchi, M.; Murase, I. (1975): “Shish kebab” structures formed on needle-like polyoxymethylene crystals. In: *J. Polym. Sci. Polym. Phys. Ed.* 13 (7), S. 1461–1465. DOI: 10.1002/pol.1975.180130715.

Isayev, A.; Kamal, M. (2009): Injection molding. Technology and fundamentals. Munich, Cincinnati: Hanser (Progress in polymer processing). avilable online at http://www.sciencedirect.com/science/book/9783446416857.

Jeffries, R. (2014): electromagnetic radiation - Why don't X-rays travel through water? avilable online at https://physics.stackexchange.com/questions/150546/why-dont-x-rays-travel-through-water/150600#150600, checked on 25.09.2019.

Kinloch, A.; Young, R. (1995): Fracture Behaviour of Polymers. Dordrecht: Springer Netherlands.

Kongkhlang, T.; Reddy, K.; Kitano, T.; Nishu, T.; Tashiro, K. (2011): Cocrystallization phenomenon of polyoxymethylene blend samples between the deuterated and hydrogenated species. In: *Polym J* 43 (1), S. 66–73. DOI: 10.1038/pj.2010.106.

Koo, G.; Roldan, L. (1972): Effect of cyclic loading on the morphology of polytetrafluoroethylene. In: *J. Polym. Sci. A-2 Polym. Phys.* 10 (6), S. 1145–1152. DOI: 10.1002/pol.1972.160100616.

Kurosu, H.; Komoto, T.; Ando, I. (1988): 13C NMR chemical shift and crystal structure of polyoxymethylene in the solid state. In: *Journal of Molecular Structure* 176, S. 279–283. DOI: 10.1016/0022-2860(88)80247-3.

Lang, R. (1984): Applicability of Linear Elastic Fracture Mechanics to Fracture in Polymers and Short-Fiber Composites. Dissertation. Lehigh University, Betlehem, Pennsylvania, USA.

Lang, R.; Balika, W.; Pinter, G. (2004): Applicability of Linear Elastic Fracture Mechanics to Fatigue in Amorphous and Semi-crystalline Polymers. In: David R. Moore (Hg.): The application of fracture mechanics to polymers, adhesives and composites. Amsterdam: Elsevier (ESIS publication, 33), S. 83–92.

Lexikon der Kunststoffprüfung. avilable online at https://wiki.polymerservice-merseburg.de/index.php/SENT-Pr%C3%BCfk%C3%B6rper, checked on 30.09.2019.

Liparoti, S.; Speranza, V.; Pantani, R.; Titomanlio, G. (2016): Fast temperature evolution on the mold surface: Analysis and simulation. In:. PROCEEDINGS OF THE REGIONAL CONFERENCE GRAZ 2015 – POLYMER PROCESSING SOCIETY PPS: Conference Papers. Graz, Austria, 21–25 September 2015: Author(s) (AIP Conference Proceedings), S. 20014.

Liu, G.; Zhu, P.; Edward, G. (2002): Morphology distribution and processing history of injection moulded polypropylenes. In: *Macromol. Symp.* 185 (1), S. 327–340. DOI: 10.1002/1521-3900(200208)185:1<327::AID-MASY327>3.0.CO;2-G.

Lüftl, S.; Visakh, P.; Chandran, S. (2014): Polyoxymethylene Handbook. Hoboken, NJ, USA: John Wiley & Sons, Inc.

Meinel, G.; Peterlin, A. (1971): Plastic deformation of polyethylene II. Change of mechanical properties during drawing. In: *J. Polym. Sci. A-2 Polym. Phys.* 9 (1), S. 67–83. DOI: 10.1002/pol.1971.160090106.

Mennig, G.; Stoeckhert, K. (Hg.) (2013): Mold-making handbook. 3rd edition. Cincinnati: Hanser Publications. avilable online at http://www.sciencedirect.com/science/book/9781569904466.

Michler, G. (Hg.) (2008): Electron Microscopy of Polymers. Berlin, Heidelberg: Springer Berlin Heidelberg.

Michler, G. (2016): Atlas of Polymer Structures. München: Carl Hanser Verlag GmbH & Co. KG.

Narisawa, I.; Ishikawa, M. (1989): Crazing in semicrystalline thermoplastics. In: H. H. Kausch (Hg.): Crazing in Polymers, 91/92. Berlin, Mitcham, VIC, Australia: Springer; Central Book Services New Zealand [distributor] (Advances in Polymer Science), S. 353–391.

Osswald, T.; Hernández-Ortiz, J. (2006): Polymer processing. Modeling and simulation. München: Hanser Verlag. avilable online at http://www.hanser-elibrary.com/action/showBook?doi=10.3139/9783446412866.

Pecharsky, V.; Zavalij, P. (2009): Fundamentals of Powder Diffraction and Structural Characterization of Materials. 2. ed. Boston, MA: Springer US. avilable online at http://site.ebrary.com/lib/alltitles/docDetail.action?docID=10266944.

Plummer, C.; Cudré-Mauroux, N.; Kausch, H.-H. (1994): Deformation and entanglement in semicrystalline polymers. In: *Polym. Eng. Sci.* 34 (4), S. 318–329. DOI: 10.1002/pen.760340414.

Plummer, C.; Menu, P.; Cudré-Mauroux, N.; Kausch, H.-H. (1995): The effect of crystallization conditions on the properties of polyoxymethylene. In: *J. Appl. Polym. Sci.* 55 (3), S. 489–500. DOI: 10.1002/app.1995.070550314.

Raimo, M. (2011): An overview on the processing of polymers growth rate data and on the methods to verify the accuracy of the input parameters in crystallization regime analysis. In: *Progress in Crystal Growth and Characterization of Materials* 57 (2-3), S. 65–92. DOI: 10.1016/j.pcrysgrow.2011.06.001.

Rosato, D.; Rosato, D.; Rosato, M. (2000): Injection Molding Handbook. Boston, MA: Springer US.

Schnablegger, H.; Singh, Y. (2013): The SAXS Guide. Anton Paar GmbH. Graz, Austria. avilable online at https://www.anton-paar.com/at-de/saxs-guide/, checked on 31.08.2019.

Schrank, T. (2019): Residual stress measurement study on injection molded Polyoxymethylene specimens. Diploma Thesis. Montanuniversitaet Leoben, Austria. Materials Science and Testing of Plastics.

Seguela, R. (2005): Critical review of the molecular topology of semicrystalline polymers: The origin and assessment of intercrystalline tie molecules and chain entanglements. In: *J. Polym. Sci. B Polym. Phys.* 43 (14), S. 1729–1748. DOI: 10.1002/polb.20414.

Shimomura, M. (1993): Morphology Dependence of Vibrational Spectra of polyoxymethylene and poly(ethylene oxide) crystals. Osaka University, Osaka. Faculty of Science.

Shimomura, M.; Iguchi, M.; Kobayashi, M. (1988): Vibrational spectroscopic study on trigonal polyoxymethylene and polyoxymethylene-d2 crystals. In: *Polymer* 29 (2), S. 351–357. DOI: 10.1016/0032-3861(88)90346-1.

Singh, D.; Moslé, H. (1988): The relationship between processing conditions, morphological structure and mechanical properties of knit lines of an injection molded semi-crystalline thermoplastic. In: *Makromolekulare Chemie. Macromolecular Symposia* 20-21 (1), S. 489–500. DOI: 10.1002/masy.19880200151.

Strobl, G.; Schneider, M. (1980): Direct evaluation of the electron density correlation function of partially crystalline polymers. In: *J. Polym. Sci. Polym. Phys. Ed.* 18 (6), S. 1343–1359. DOI: 10.1002/pol.1980.180180614.

Zamboni, V.; Zerbi, G. (1964): Vibrational spectrum of a new crystalline modification of polyoxymethylene. In: *J. polym. sci., C Polym. symp.* 7 (1), S. 153–161. DOI: 10.1002/polc.5070070111.

Zhao, X.; Ye, L. (2011): Structure and properties of highly oriented polyoxymethylene produced by hot stretching. In: *Materials Science and Engineering: A* 528 (13-14), S. 4585–4591. DOI: 10.1016/j.msea.2011.02.039.

APPENDIX

In the following, the SAXS and WAXD patterns obtained from the scans over the whole platelet for the processing conditions C1 to C8 are given. Within one measurement technique (SAXS and WAXD), the intensity scale was kept constant for all conditions.

<table>
<tr><th colspan="2">C1</th></tr>
<tr><th>SAXS</th><th>WAXD</th></tr>
<tr><td>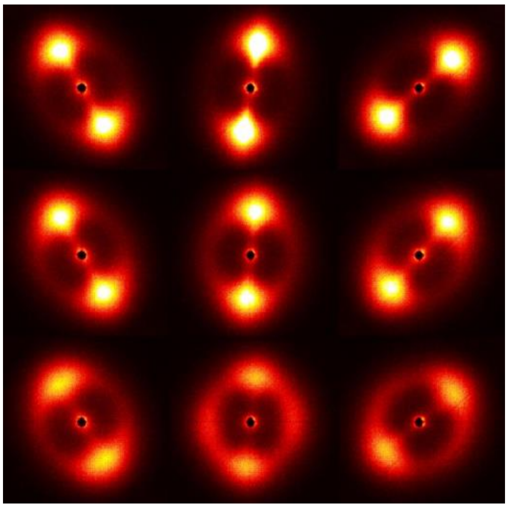</td><td>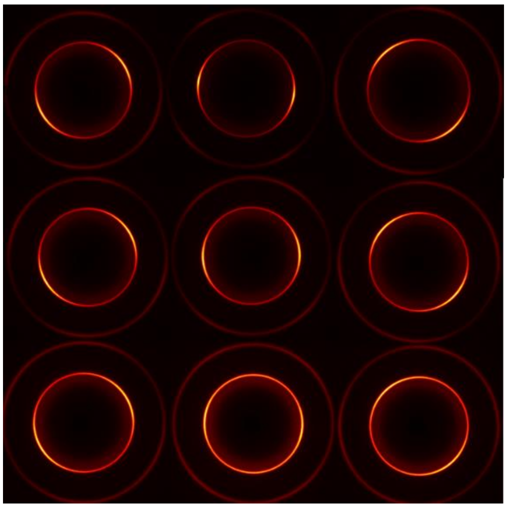</td></tr>
</table>

<table>
<tr><th colspan="2">C2</th></tr>
<tr><th>SAXS</th><th>WAXD</th></tr>
<tr><td>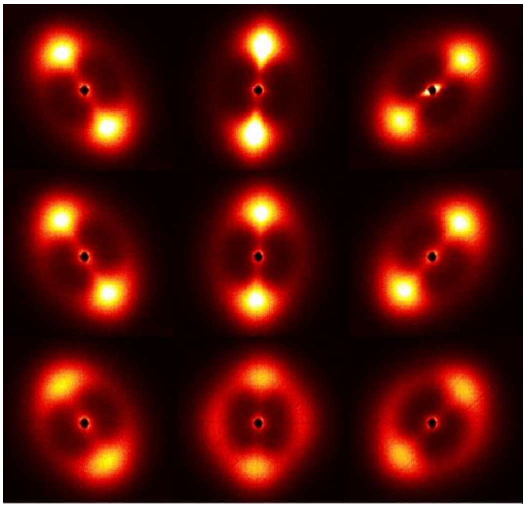</td><td>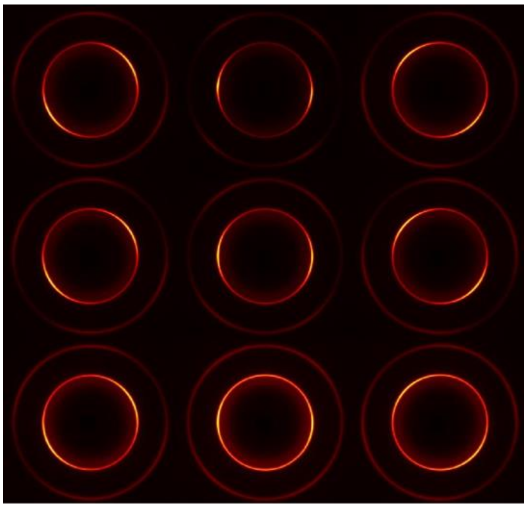</td></tr>
</table>

<table>
<tr><th colspan="2">C3</th></tr>
<tr><th>SAXS</th><th>WAXD</th></tr>
<tr><td>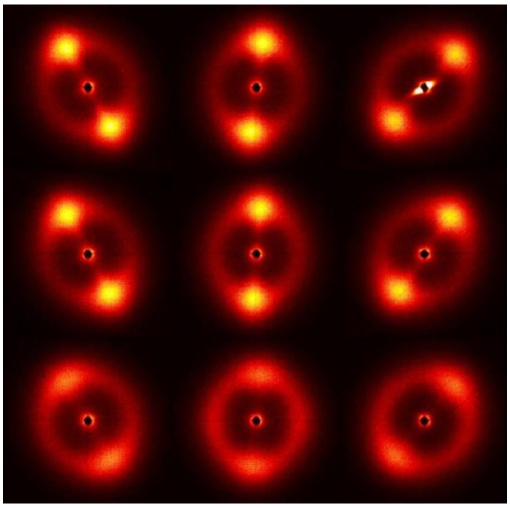</td><td>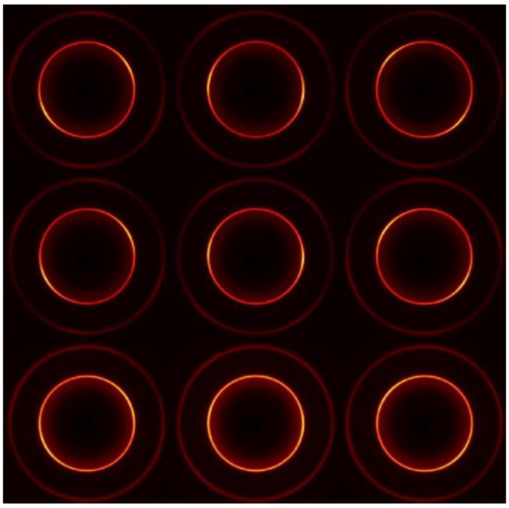</td></tr>
</table>

<table>
<tr><th colspan="2">C4</th></tr>
<tr><th>SAXS</th><th>WAXD</th></tr>
<tr><td>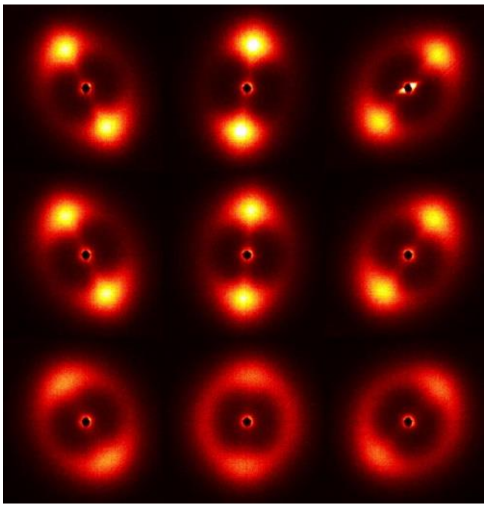</td><td>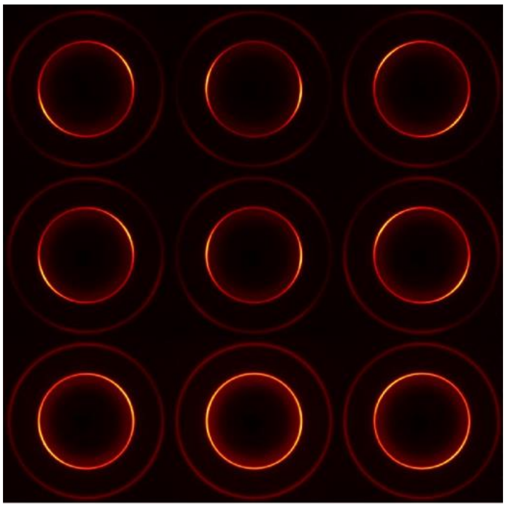</td></tr>
</table>

<table>
<tr><th colspan="2">C5</th></tr>
<tr><th>SAXS</th><th>WAXD</th></tr>
<tr><td>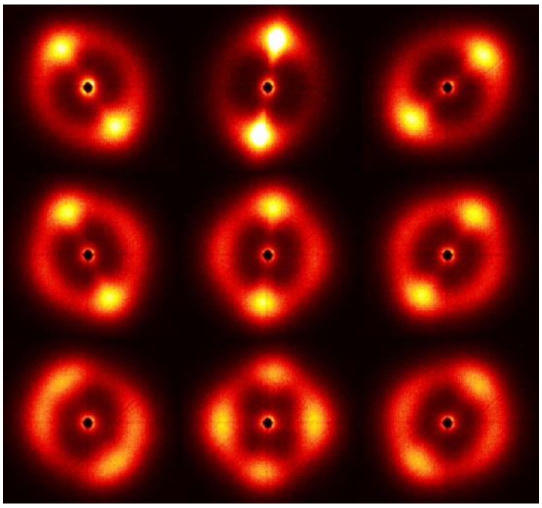</td><td>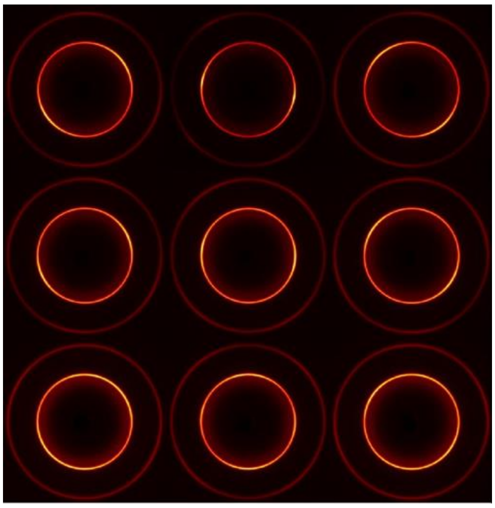</td></tr>
</table>

<table>
<tr><th colspan="2">C6</th></tr>
<tr><th>SAXS</th><th>WAXD</th></tr>
<tr><td>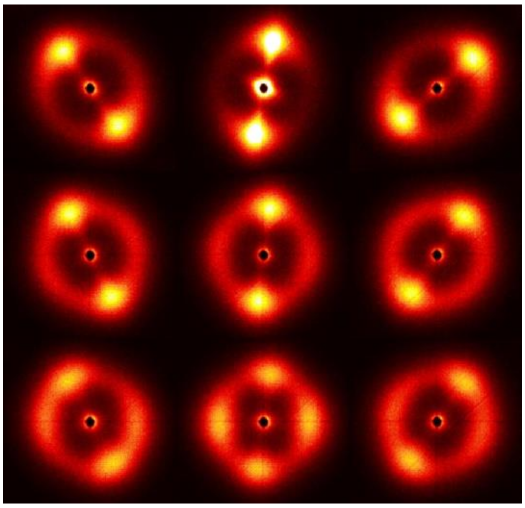</td><td>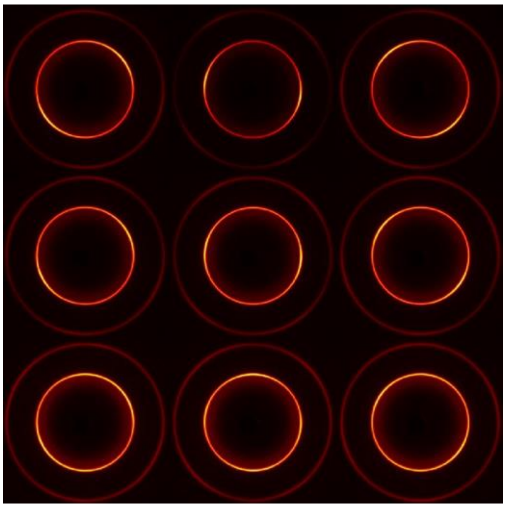</td></tr>
</table>

C7	
SAXS	**WAXD**
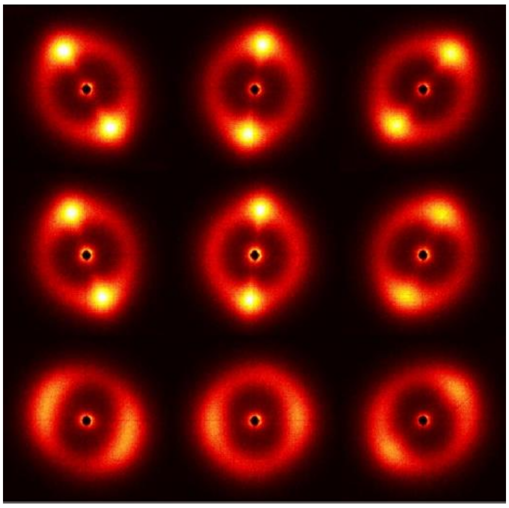	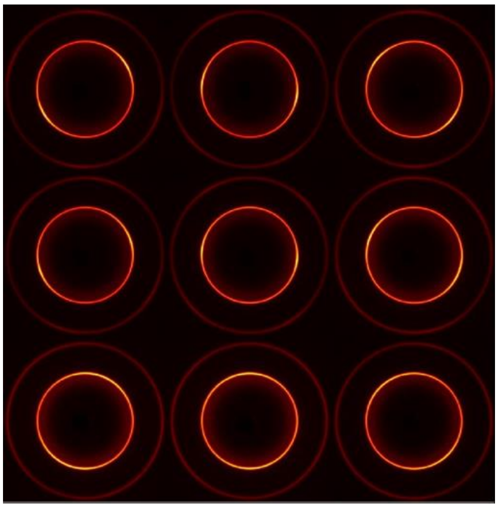

C8	
SAXS	**WAXD**